Photophysical Properties of Quantum-Cutting Ytterbium(III)-Doped Perovskite Nanocrystals

Joo Yeon Roh

A dissertation

submitted in partial fulfillment of the

requirements for the degree of

Doctor of Philosophy

University of Washington

2023

Reading Committee:

Daniel R. Gamelin, Chair

Brandi M. Cossairt

Alexandra Velian

Program Authorized to Offer Degree:

Chemistry

University of Washington

Abstract

Photophysical Properties of Quantum-Cutting Ytterbium(III)-Doped Perovskite Nanocrystals

Joo Yeon Roh

Chair of the Supervisory Committee:
Professor Daniel R. Gamelin
Department of Chemistry

Ytterbium(III)-doped all-inorganic lead-halide perovskites (Yb^{3+}:$CsPb(Cl_{1-x}Br_x)_3$) have recently been discovered to display highly efficient quantum cutting, in which the energy from each ultraviolet photon absorbed by the perovskite is split and emitted as *pairs* of near-infrared photons by Yb^{3+} dopants. Experimental photoluminescence quantum yields of nearly 200% have been reported for nanocrystals and thin films. Combining such high photoluminescence quantum yields and strong, broadband absorption of the perovskites, these materials drew extraordinary research interest for their applications in solar energy conversion technologies. This work explores the fundamental origins of quantum cutting in Yb^{3+}:$CsPb(Cl_{1-x}Br_x)_3$ nanocrystals and the unique structural and photophysical properties induced by Yb^{3+} doping. Quantum-cutting energy transfer follows two consecutive steps: (i) sub-picosecond depopulation from the perovskite host to a Yb^{3+}-

induced defect state and (ii) energy transfer from the same defect state to two Yb^{3+} ions simultaneously on the order of nanoseconds. The observation of this second energy transfer step, shown by a rise time of Yb^{3+} photoluminescence, confirms that quantum-cutting occurs *via* an intermediate state, which is induced by Yb^{3+} doping. Anion alloying *via* anion exchange of these materials allows tuning of the perovskite bandgap, which provides new insights to Yb^{3+} sensitization. Quantum cutting remains exothermic until the perovskite bandgap reaches a thermodynamic threshold for energy conservation (Yb^{3+}:$CsPb(Cl_{1-x}Br_x)_3$, $x \sim 0.66$), at which the quantum-cutting energy-transfer rate becomes increasingly temperature dependent. This temperature dependent behavior in Yb^{3+}:$CsPb(Cl_{1-x}Br_x)_3$ ($0.66 < x < 1.00$) is accompanied by strong negative thermal quenching of the Yb^{3+} luminescence. As a result, Yb^{3+}:$CsPbBr_3$ nanocrystals show single-Yb^{3+} sensitization at cryogenic temperature and thermally-activated quantum cutting near room temperature. Finally, Yb^{3+} coordination environments in $CsPbCl_3$ and $CsPbBr_3$ lattices, spatial distribution of Yb^{3+} dopants during anion-exchange reaction, and diverse Yb^{3+} speciation are discussed in detail. These results enhance the fundamental understanding of this unique quantum cutter with potential ramifications in solar technologies.

TABLE OF CONTENTS

LIST OF FIGURES

LIST OF SCHEMES

LIST OF TABLES

ACKNOWLEDGMENTS

I want to begin by thanking Prof. Daniel Gamelin for welcoming me into his group at the University of Washington and providing me with resources and mentorship for me to develop as a scientist. Your dedication, knowledge, and enthusiasm for science has been exceptionally inspirational, which guided me throughout my scientific journey here. I feel very fortunate and grateful to have joined a remarkably collaborative community with such scientific rigor that you have fostered.

Next, I want to thank my committee members Profs. Brandi Cossairt, Alexandra Velian, Kai-Mei Fu for their help in development and review of my dissertation. I have truly valued all your input throughout my time here at division meetings and MEM-C meetings, which provided me with opportunities to grow as a scientist.

The Gamelin Group has become my home these past several years and I want to thank every member for providing me with a collaborative community, friendship, and support. To start, I want to particularly thank team ytterbium. Dr. Daniel Kroupa, thank you for welcoming me into team ytterbium and helping me pave my way to become a spectroscopist. Your mentorship and input throughout my graduate school career were truly valued. Dr. Tyler Milstein, thank you for teaching me everything I know about perovskite NC syntheses and your friendship and support. I want to thank Prof. Sidney Creutz for his mentorship and being my scientific role model in the group. You taught me everything I know about structural characterization, and I am grateful to have worked alongside you. Dr. Ted Cohen, thank you for feeding me with fun ideas for new experiments and being my CHB 212 desk buddy for many years. Prof. Matthew Crane, thank you for always being available for troubleshooting and tough laser problems. Dr. Matthew Smith, thank you for making those late helium measurement days so fun. Dr. Kyle Kluherz, thank you for amazing TEM images and always being available to chat about structural analyses. Dr. Christian Erickson, thank you for always being available to chat about science and any experimental frustrations over a beer. Support, encouragements, and silly jokes from you and Emily Garvin have brightened up countless days. Dr. Michael De Siena, thank you for showing me my way around the optics lab and how to efficiently work in the lab. Dr. Kira Hughes Lund and Dr. Kimberly Hartstein, your friendship, support, and wisdom have been crucial during my time here. I am grateful to have shared so many of my life events with you. Kelly Walsh, I believe you will now rule the basement with your iron fists. You are an amazing role model to many, and I feel fortunate to have worked with you. My two loudest CHB 212 office mates, Laura Jacoby and Atch Gopalan, thank you for brightening up many frustrating afternoons and fun and loud (sometimes distracting) conversations. I am excited to have passed down my ytterbium torch to team chromium-ytterbium, led by Kimo Pressler. You have paved a new avenue of ytterbium research, and I cannot wait to see the rest of your scientific journey. Eden Tzanetopoulos, your enthusiasm for science even with a broken knee is inspirational and thank you for laughing at all my jokes. Jacob Baillie, never stop asking questions. Thom Snoeren, I am excited to learn more about ytterbium from you with those two clowns next to you. Dr. Stephen Gibbs, I admire your dedication to science and capabilities as a scientist and a reliable

labmate. Rayne Anderson, I am so grateful to have met you all those years ago as my first student. I am amazed by your enthusiasm to understand the details of each experiment. Julie Schwartz, your desire to learn and further your scientific knowledge is incredibly admirable. Drs. Charles Barrows, Patrick Whitham, and Prof. Alina Schimpf, thank you for your lab-life wisdom, and I am grateful for your friendship and support. Prof. Victor Polinger, thank you for making weekly group meetings more enjoyable and rigorous. I have learned a lot from your questions, which allowed me to think outside the box.

My time at University of Washington was more enjoyable due to my cohorts, Dr. Robert Weakly, Jason Sandwisch, Dr. Ryan DiRisio, and Dr. Sarah Sweger. Late night problem sets and projects were not so bad with you, and I am grateful for all the coffee runs and beer talks we shared. Your intelligence, dedication to science, and hard work have been exceptionally admirable, and it has truly been an honor to have grown as a scientist alongside you. Dr. Sarah Sweger, Bean, Fig, and Bouillon, you have become my first Seattle family and my time here has been incredibly fun because of you and your support. Troy Kilburn, thank you for sharing your beer to fuel my scientific journey. Sophie Yoo, thank you for your continued friendship and support across the globe for many years.

I am exceptionally grateful to John and Dr. Monica Gillespie for welcoming me into their family and their never-wavering support. I owe much of my success in graduate school to the Gillespie family and your encouragement.

Lastly, my mom, thank you for showing the importance of staying curious and supporting me with your unconditional love. My baby sister, I am constantly amazed at your dedication and sacrifice to help and save people.

To the loves of my life:
Jose, Cheeto, and Namu

Chapter 1. Introduction

1.1 **Overview**

Trivalent lanthanides (Ln^{3+}) have consistently attracted considerable research interest for a wide range of applications such as lasing, telecommunications, solar energy, display, lighting, and biotechnologies.[1-4] Their unique luminescent properties are incorporated into a variety of inorganic crystal lattices by intentionally adding Ln^{3+} ions as impurity defects or dopants. Particularly, ytterbium (Yb^{3+}) dopants are frequently used for spectral shifting for applications in solar technologies, but efficient spectral shifting had not been demonstrated in any materials for practical applications until the discover of Yb^{3+}-doped all-inorganic lead-halide perovskites (Yb^{3+}:$CsPb(Cl_{1-x}Br_x)_3$).[5, 6] Both nanocrystalline and thin film morphologies of these materials have demonstrated photoluminescence quantum yields approaching 200% *via* quantum cutting, a process which converts the energy from an absorbed ultraviolet photon into a pair of emitted photons of lower energy. This chapter explores quantum cutting *via* broadband sensitization in Yb^{3+}:$CsPb(Cl_{1-x}Br_x)_3$ materials, their energy transfer mechanisms, and their efficiencies relative to previous quantum-cutting materials with Ln^{3+} dopants. While studying the photophysical and structural properties of Yb^{3+}:$CsPb(Cl_{1-x}Br_x)_3$, their implications for solar technologies are further explored.

1.2 **Luminescent properties of trivalent lanthanides**

The photoluminescence (PL) of trivalent lanthanide ions (Ln^{3+}) has been investigated for decades in phosphors research due to their unique photophysical properties.[1-4] The electrons in the 4*f*-shell valence orbital are highly shielded by the 5*s*- and 5*p*-shells from the surrounding matrix or the host crystal, where the Ln^{3+} is a dopant. The 5*s*- and 5*p*-shells are lower in energy but are spatially located outside 4*f*-valence shells. Therefore, Ln^{3+} ions show sharp and highly structured PL peaks, resembling those of free ions, and their optical transitions show negligible effects from the surrounding matrix. Exploiting this nature, the Dieke diagram, which compiles the $4f^n$ energy levels of all Ln^{3+} ions, is applicable in any surrounding environment.[7] Instead, the electronic transitions of Ln^{3+} ions are determined by the interactions within the same configuration such as the Coulombic interaction and spin-orbit coupling.

Scheme 1.1 illustrates the interactions that split the electronic states for Eu^{3+} ([Xe] $4f^6$), going from strongest to weakest effect.[2] The electron-electron repulsion (Coulombic interaction) within the seven degenerate 4*f* orbitals causes a splitting in the order of 10^4 cm^{-1}, and each of these terms is split into several *J*-multiplets by spin-orbit coupling in the order of 10^3 cm^{-1}. Finally, in a coordination environment, the individual *J*-levels are further split by the crystal field, which is usually in the order of 10^2 cm^{-1}. The crystal field splittings are determined by the coordination environment, and the resulting fine structure in absorption or PL provides information about the Ln^{3+} site symmetry as well. Although the coordination environment of Ln^{3+} ions only makes marginal contributions to the electronic structure, the transition probabilities critically depend on their coordination environment or ligands.

Scheme 1.1. Schematic representation of the interactions (Coulombic interactions, spin-orbit coupling, and crystal-field splitting) leading to various electronic energy levels for Eu^{3+} ($4f^6$).

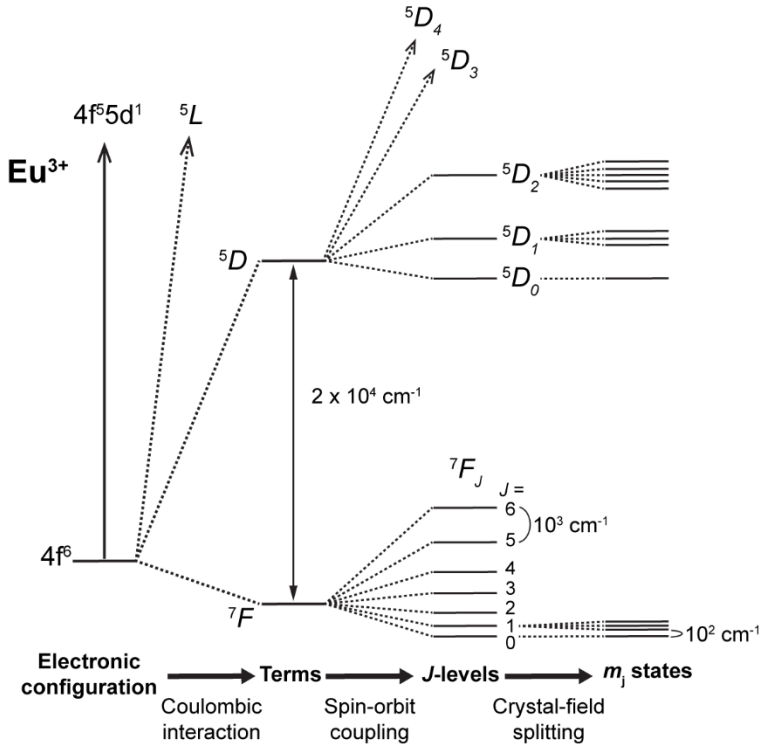

These *f-f* transitions of Ln^{3+} ions are formally electric-dipole forbidden by the Laporte selection rule, but they become partially electric-dipole allowed through a couple of mechanisms. In the limit of a free Ln^{3+} ion, only magnetic-dipole transitions are allowed, and the transition energy is

not affected by the host matrix of the Ln^{3+} ion. Ln^{3+} ions in a coordinating environment, however, show *f-f* transitions that are electric-dipole allowed because the ligand field couples odd-parity configurations with the pure electronic transition. Although some transitions are both electric-dipole- and magnetic-dipole-allowed (*e.g.* luminescence of Tb^{3+}[2, 8]), most *f-f* transitions gain allowedness by mixing with configurations of opposite parity.

Scheme 1.2. Simple three-level upconversion and quantum-cutting schemes with electronic transitions: (a) ground state absorption (0→1), (b) excited-state absorption (1→2), (c) emission from an upper excited state as a result of upconversion (2→0), (d) direct excitation into an upper excited state (0→2), (e) emission of two lower-energy photons as a result of quantum cutting (2→1), (1→0).

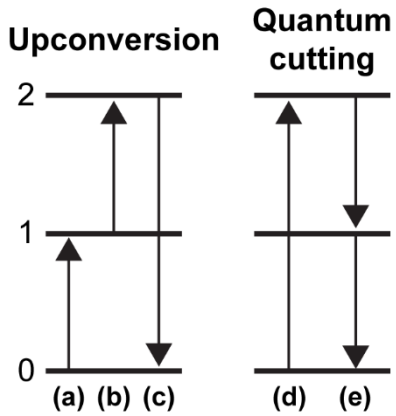

In addition to the single-photon transitions, different types of *f-f* electronic transitions can be achieved in the limit of allowed transitions: upconversion and quantum cutting, as shown in Scheme 1.2. In upconversion, a photoexcited ion is excited again to achieve emission from a higher luminescent state that is roughly double the energy of the lower luminescent state.[9] Quantum cutting, on the other hand, is a photomultiplication process, where an absorbed high energy photon is split to generate two or more lower energy photons.[10] Both mechanisms have important technological implications, but quantum cutting provides potential ramifications for highly efficient spectral shifting of ultraviolet (UV) into near-infrared (NIR) photons in solar technologies.

1.3 Quantum cutting in trivalent lanthanide-doped materials

Materials research in the past several decades has focused on improving the efficiencies of single-junction photovoltaics beyond the Shockley-Queisser thermodynamic limit of ~32%.[11, 12] The rest of the terrestrial solar photons are lost through different mechanisms such as thermalization, transmission, and other minor losses such as recombination, junction, and contact voltage losses, as illustrated in Figure 1.1.[13, 14] Transmission losses occur when incident photons are of insufficient energy relative to the bandgap (E_g) of the photovoltaic material. Those low energy photons transmit through the material, and therefore energy is lost. Photonic upconversion can reduce transmission losses by absorbing those otherwise lost low-energy photons and re-emitting at a higher energy level, but this upconversion process is only efficient at high incident or excitation power (*i.e.* the upconverted emission intensity (I_{up}) is related to the excitation intensity (I_{ex}) by $I_{up} \propto (I_{ex})^2$).[13, 14] Thermalization losses occur when the photovoltaic material, such as crystalline silicon (c-Si), absorbs photons higher in energy than its E_g. The excess energy is lost as heat as electrons relax (thermalize) to the conduction band minimum. Photomultiplication has become a key to exploiting high-energy solar photons to generate multiple lower-energy electron-hole pairs, ultimately reducing the thermalization loss in photovoltaics.[15] Among several strategies such as singlet fission[16, 17] and multi-exciton generation,[17-19] quantum cutting has stimulated a large research interest because the excitation energy is extracted photonically through emitters instead of being extracted *via* inefficient charge separation and collection.[5, 6, 10, 20-27]

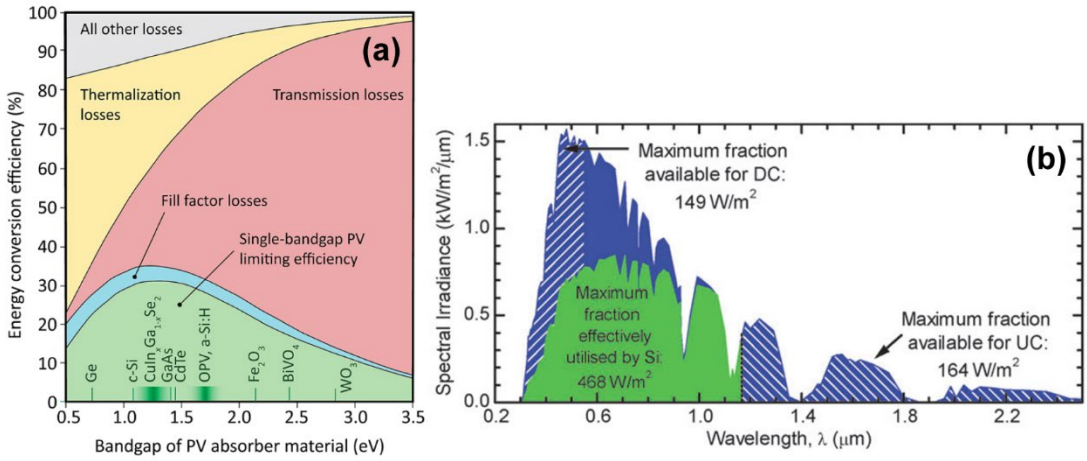

Figure 1.1. (a) Relative importance of fundamental loss mechanisms in solar energy conversion as a function of the photovoltaic absorber bandgap. Reprinted with permission from ref. [14]. Copyright 2015 The Royal Society of Chemistry. **(b)** AM 1.5 G solar spectrum

showing the fraction of solar energy absorbed/utilized by c-Si photovoltaic devices (green), and the additional regions of the spectrum that can be utilized *via* upconversion (UC) or quantum cutting (DC). Reprinted with permission from ref. [28]. Copyright 2006 Elsevier.

Trivalent ytterbium (Yb^{3+}) is a well-known emitter used for quantum cutting because of its simple electronic structure, involving a single $^2F_{5/2}$ excited state and the $^2F_{7/2}$ ground state without any upper excited states.[7] Once sensitized, Yb^{3+}, like other Ln^{3+}, shows radiative lifetimes in the order of milliseconds, which is several orders of magnitude longer than those of organic fluorophores.[2, 3] Furthermore, this single *f-f* transition of Yb^{3+}, centered around 10300 cm^{-1} (~1.3 eV) matches favorably with the E_g of silicon (9000 cm^{-1} (1.1 eV)), making Yb^{3+} an ideal emitter for applications in solar spectral shifting.

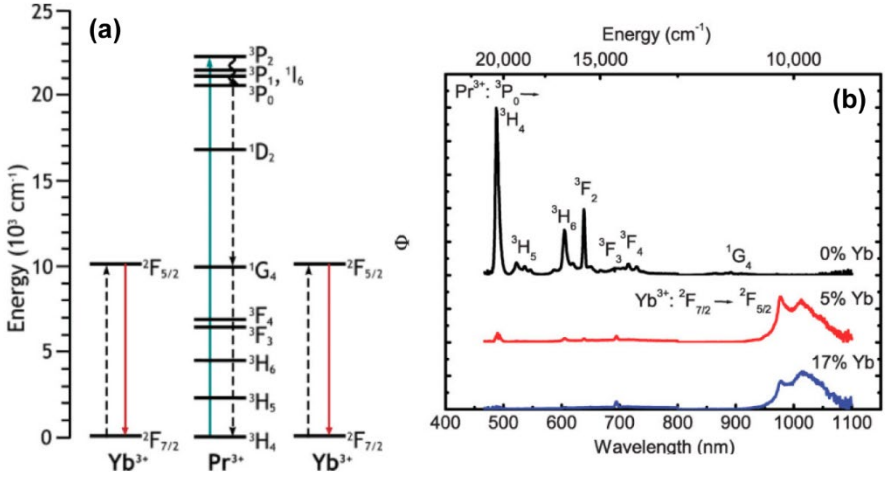

Figure 1.2. (a) Energy levels and quantum cutting mechanism for the Pr^{3+}– Yb^{3+} couple. The photoexcited energy for ^3P_J ($J = 0, 1, 2$) and $^1I_6$ levels of Pr^{3+} is split to excite two Yb^{3+} ions and re-emitted *via* Yb^{3+} $^2F_{5/2} \rightarrow {}^2F_{7/2}$. Solid, dotted, and curved arrows represent optical transitions, nonradiative energy transfer processes and nonradiative relaxation processes, respectively. **(b)** PL spectra for 0.1% Pr^{3+}, *x*% Yb^{3+}:SrF_2 ($x = 0$ (black), 5 (red), 17 (blue)). Reprinted with permission from ref. [22]. Copyright 2009 Wiley.

In most quantum cutting materials, both the activator, Yb^{3+}, and the sensitizer Ln^{3+} (*e.g.* Tb^{3+},[20] Pr^{3+},[21, 22] Tm^{3+},[23] Er^{3+},[24] Nd^{3+},[25] Ho^{3+}[26]) are codoped into inorganic host crystals such as YF_3, $Cs_2Y_2Br_9$, and YPO_4. Figure 1.2 shows a representative quantum cutting system that involves two Ln^{3+} ions: Pr^{3+}, Yb^{3+}:SrF_2.[22] Typically, a high energy photon is absorbed by the sensitizer Ln^{3+} ion, and that photoexcited energy is re-emitted in the form of two NIR photons through Yb^{3+} ions. For example, in Pr^{3+}, Yb^{3+}:SrF_2 (Figure 1.2b), the visible Pr^{3+} ($^3P_0 \rightarrow {}^3H_J$ and ^3F_J) PL is almost

entirely quenched, giving rise to the Yb^{3+} ($^2F_{5/2} \rightarrow {}^2F_{7/2}$) PL in the NIR. These systems, however, have not demonstrated sufficiently high efficiency to be integrated into solar technologies because quantum-cutting energy-transfer in these materials involves weak multipolar coupling between two formally electric-dipole-forbidden transitions. Although magnetic- and induced electric-dipole transitions are allowed, they are significantly weaker than other fully allowed transitions found in materials such as organic chromophores.[27] Therefore, oscillator strengths of *f-f* transitions in Ln^{3+} ions are on the order of 10^{-6},[1, 2] making them poor sensitizers with their narrow and weak absorption features (and PL, see Figure 1.2b). Broadband sensitization of Yb^{3+} has been explored (Pr^{3+}, Yb^{3+}-doped $NaYF_4$ with coumarin dyes, Yb^{3+}:CdSe, Yb^{3+}:$Na(In_{1-x}Pb_x)S_2$), but the photoluminescence quantum yields (PLQYs) are still too low for practical solar applications.[27, 29, 30]

1.4 Quantum-cutting Yb^{3+}-doped all-inorganic lead-halide perovskites

1.4.1 *$CsPb(Cl_{1-x}Br_x)_3$ perovskites as broadband sensitizers for Yb^{3+}*

All-inorganic lead-halide perovskite ($CsPbX_3$, X = Cl, Br, I) nanocrystals (NCs) have been the center of phosphors and optoelectronics research in recent years, due to their large absorption cross section, sharp excitonic PL features, defect tolerance, and facile bandgap tunability.[31-37] Additionally, the octahedral coordination at the Pb^{2+} site makes the material a desirable host for metal dopants.[4, 37] Song and coworkers first demonstrated quantum cutting *via* broadband sensitization in Yb^{3+}, Ce^{3+}-codoped $CsPb(Cl_{0.5}Br_{0.5})_3$ and Yb^{3+}-doped $CsPbCl_3$ NCs, exceeding over 100% NIR PLQYs, confirming that Yb^{3+} ions in these systems are sensitized *via* a quantum-cutting mechanism and not a single-Yb^{3+} mechanism.[5, 6] In detail, while $CsPbCl_3$ NCs only show excitonic PL at the E_g of the perovskite, Yb^{3+}:$CsPbCl_3$ NCs in Figure 1.3 show well-sensitized Yb^{3+} PL with barely discernable excitonic PL. Unlike previous quantum-cutting materials involving two Ln^{3+} ions, broadband absorption (Figure 1.3) marks a key difference in demonstrating such high efficiencies. Additionally, absorption coefficients of $CsPbCl_3$ and $CsPbBr_3$ are larger than those of Ln^{3+} ions by 4 orders of magnitude,[1, 2, 38, 39] establishing themselves as ideal sensitizers for Yb^{3+} dopants.

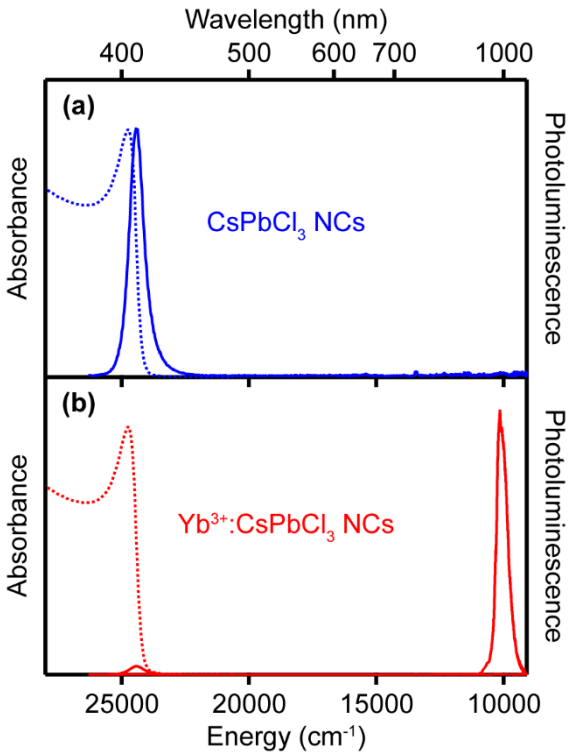

Figure 1.3. Representative absorbance (dotted) and PL (solid) spectra of **(a)** $CsPbCl_3$ (blue) and **(b)** Yb^{3+}:$CsPbCl_3$ (red) NCs measured at room temperature. λ_{exc} = 375 nm

Following Song and coworkers,[5] many researchers reported PLQYs over 100% measured for Yb^{3+}:$CsPb(Cl_{1-x}Br_x)_3$ in various morphologies (NCs, solution-processed, vapor-deposited thin films), as summarized in Table 1.1.[5, 6, 39-56] These reports also imply that quantum cutting is not an intrinsic property of Yb^{3+}:$CsPb(Cl_{1-x}Br_x)_3$ composition or size itself. In fact, a few of the highest PLQYs in Table 1.1 were measured for bulk morphologies. Furthermore, quantum confinement is not expected in the $CsPbX_3$ NCs, since their average edge lengths range from ~9 to 18 nm, while their Bohr exciton diameters are ~5 and ~7 nm for $CsPbCl_3$ and $CsPbBr_3$, respectively.[33] These observations support the conclusion that Yb^{3+} PL is indeed sensitized *via* broadband absorption and energy transfer from the host perovskite.

Table 1.1. Summary of reported quantum-cutting efficiencies in Yb^{3+}-doped $CsPb(Cl_{1-x}Br_x)_3$.

Material	Morphology	Yb^{3+} PLQY	Reference
Yb^{3+}, Ce^{3+}:$CsPb(Cl_{0.5}Br_{0.5})_3$	Nanocrystals	119%	Song[6]
Yb^{3+}:$CsPbCl_3$	Nanocrystals	143%	Song[5]
Yb^{3+}:$CsPbCl_3$	Nanocrystals	170%	Gamelin[39]
Yb^{3+}:$CsPb(Cl_{0.35}Br_{0.65})_3$	Solution-processed films	193%	Gamelin[40]
Yb^{3+}:$CsPbCl_3$	Nanocrystals	120%	Yu[41]
Yb^{3+}:$CsPbCl_3$	Nanocrystals	130%	Gamelin[42]
Yb^{3+}:$CsPb(Cl_{0.5}Br_{0.5})_3$	Vapor-deposited films	183%	Gamelin[43]
Yb^{3+}:$CsPbCl_3$	Nanocrystals	175%	Gamelin[44]
Yb^{3+}:$CsPbCl_3$	Nanocrystals	164%	Wu[45]
Yb^{3+}:$CsPb(Cl_{1-x}Br_x)_3$	Nanocrystals	~200%	Gamelin[46]
Yb^{3+}, Pr^{3+}, Ce^{3+}:$CsPb(Cl_{1-x}Br_x)_3$	Nanocrystals	160%	Song[47]
Yb^{3+}, Mn^{2+}:$CsPbCl_3$	Nanocrystals	103%	Chen[48]
Cr^{3+}, Yb^{3+}, Ce^{3+}:$CsPbCl_3$	Nanocrystals	175%	Song[49]
Yb^{3+}:$CsPbCl_3$	Layered films	130%	Miyasaka[50]
Yb^{3+}:$CsPbCl_3$	Nanocrystals	150%	Hens[51]
Yb^{3+}, Er^{3+}:$CsPb(Cl_{0.6}Br_{0.4})_3$	Nanocrystals	129%	Mao[52]
Yb^{3+}:$CsPbCl_3$	Nanocrystals	110%	Li, Chen, Chen[54]
Yb^{3+}:$CsPbCl_3$	Nanocrystals	127%	Zhu[55]
Yb^{3+}:$CsPbCl_3$	Nanocrystals	130%	Weiss[53]
Yb^{3+}, La^{3+}:$CsPbCl_3$	Nanocrystals	168%	Pan[56]

1.4.2 *Proposed Yb^{3+} sensitization mechanisms in Yb^{3+}-doped $CsPb(Cl_{1-x}Br_x)_3$*

Since Yb^{3+}-doped $CsPb(Cl_{1-x}Br_x)_3$ materials are a newly discovered composition of matter, several Yb^{3+} sensitization schemes have been proposed to investigate the fundamental origins of their exceptionally high PLQYs.[5, 39, 51] While E_g of $CsPbCl_3$ is 24600 cm^{-1} (3.05 eV), the Yb^{3+} *f-f* transition energy is centered at 10300 cm^{-1} (1.25 eV). In principle, a fundamental energy-

conservation threshold for quantum cutting, which is twice the Yb^{3+} $^2F_{7/2} \rightarrow {}^2F_{5/2}$ absorption energy ($2\times E_{f\text{-}f}$), must also be involved in establishing a sensitization scheme for Yb^{3+}:$CsPb(Cl_{1-x}Br_x)_3$ but is omitted here, since E_g of $CsPbCl_3$ is substantially larger than $2\times E_{f\text{-}f}$.

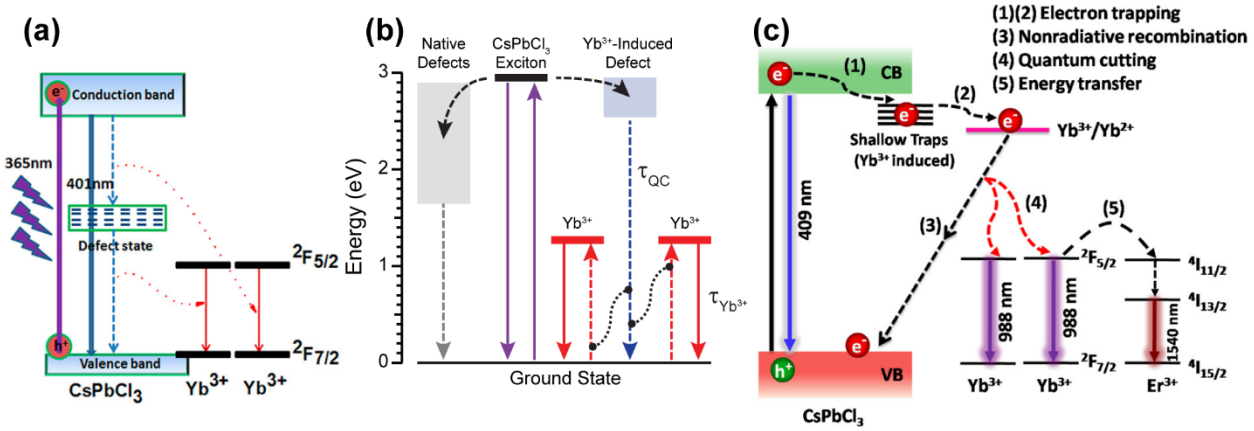

Figure 1.4. (a) A step-wise Yb^{3+}-sensitization mechanism, involving a mid-bandgap trap state of $CsPbCl_3$. Reprinted with permission from ref. [5]. Copyright 2017 American Chemical Society. **(b)** A cooperative Yb^{3+}-sensitization mechanism, involving a shallow dopant-induced defect/trap state. Reprinted with permission from ref. [39]. Copyright 2018 American Chemical Society. **(c)** A transient-redox Yb^{3+}-sensitization mechanism, involving transient formation of Yb^{2+} at a shallow trap state, prior to exciting two Yb^{3+} ions. Reprinted with permission from ref. [51]. Copyright 2020 American Chemical Society.

First, Song and coworkers proposed a step-wise Yb^{3+}-sensitization mechanism, involving a deep trap state within the perovskite E_g.[5] In this mechanism (Figure 1.4a), the photoexcited energy is trapped in the mid-gap state of $CsPbCl_3$, consecutively exciting one Yb^{3+} ion, followed by excitation of the second Yb^{3+} ion as the trapped energy decays to the ground state. The second quantum-cutting sensitization mechanism (Figure 1.4b), proposed by Gamelin and coworkers, involves energy transfer from the exciton to a shallow dopant-induced defect state, followed by cooperative energy transfer to simultaneously excite two Yb^{3+} ions.[39] These two mechanisms will be discussed further in the following sections. Finally, in the third proposed mechanism[51] (Figure 1.4c), upon photoexcitation, electrons are trapped in the dopant-induced defect state, which facilitates charge transfer to reduce Yb^{3+} to Yb^{2+}. This reduction is immediately followed by oxidation of Yb^{2+} to form Yb^{3+} *via* electron transfer to the valence band of the perovskite. This electron-transfer process provides sufficient energy to excite two Yb^{3+} ions simultaneously. The position of the $Yb^{3+/2+}$ level relative to the perovskite band edges, however, is not yet reported.

Instead, a ligand-metal charge transfer (LMCT) state of $[YbCl_6]^{3-}$ can be considered for this discussion, since Yb^{3+} is substitutionally doped into the octahedral Pb^{2+} site. The first LMCT excited states for $[YbCl_6]^{3-}$ and $[YbBr_6]^{3-}$ are observed at ~36000 cm^{-1} and ~29000 cm^{-1}, respectively, both ~10000 cm^{-1} (1 eV) higher in energy than E_g of $CsPbCl_3$and $CsPbBr_3$ perovskites.[57-59] Therefore, excitation from the shallow dopant-induced defect state to the $[YbX_6]^{3-}$ charge transfer band requires nonradiative energy transfer from photoexcited perovskites to already excited Yb^{3+} ions, resulting in an Auger-type cross-relaxation and ultimately limiting PLQY of the system to 100%.[44]

1.4.3 *Aliovalent doping of Yb^{3+} and charge compensation*

The step-wise and cooperative quantum-cutting energy-transfer mechanisms may propose defect/trap states with different energies, but a defect state is critical in both mechanisms. Although emission from these defect states is not observed in Yb^{3+}:$CsPb(Cl_{1-x}Br_x)_3$, this state can be probed in $CsPb(Cl_{1-x}Br_x)_3$ doped with spectroscopically-innocent trivalent rare-earth ions (RE^{3+}). These ions, such as Y^{3+}, La^{3+}, Ce^{3+}, Gd^{3+}, and Lu^{3+}, have chemically similar properties as Yb^{3+} ions but do not have any interfacing electronic states within the bandgap of the perovskites and, therefore, are energetically irrelevant to the host.[7]

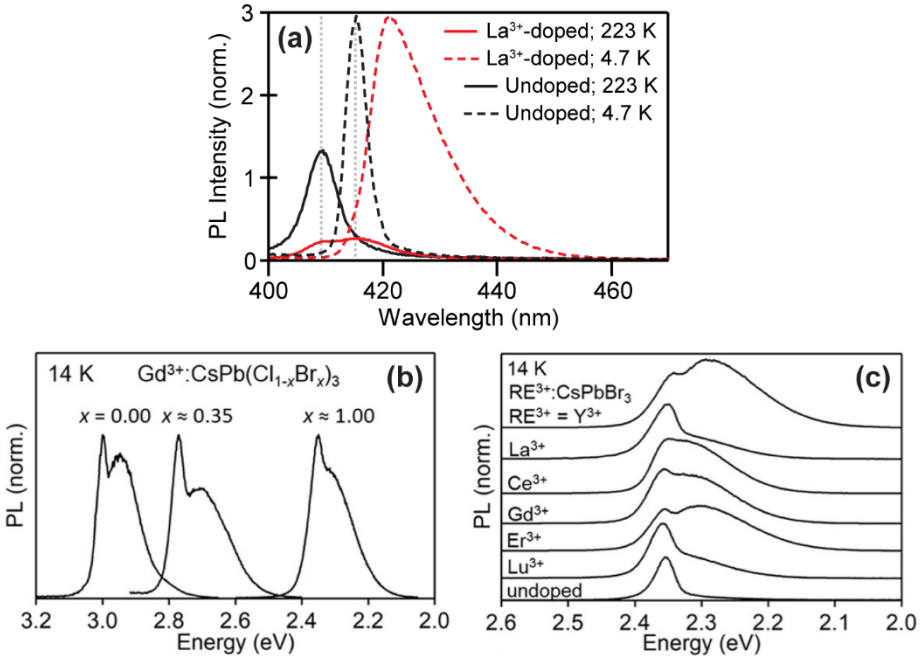

Figure 1.5. (a) Steady-state PL spectra of La^{3+}-doped (red) and undoped (black) $CsPbCl_3$ NCs at 4.7 (dashed) and 223 K (solid). Reprinted with permission from ref. [39]. Copyright

2018 American Chemical Society. **(b)** Steady-state PL spectra of Gd^{3+}:$CsPb(Cl_{1-x}Br_x)_3$ NCs (x = 0.00, 0.35, 1.00) at 14 K. Reprinted with permission from ref. [60]. Copyright 2022 American Chemical Society. **(c)** Steady-state PL spectra of RE^{3+}-doped and undoped (bottom) $CsPbBr_3$ NCs (RE^{3+} = Y^{3+}, La^{3+}, Ce^{3+}, Gd^{3+}, Er^{3+}, Lu^{3+}) Reprinted with permission from ref. [60]. Copyright 2022 American Chemical Society.

Asai and coworkers reported broad defect emission near the band-edge in La^{3+}:$CsPbCl_3$ single crystals (SCs) at cryogenic temperature.[61] Following this study, a range of spectroscopically-innocent RE^{3+} ions were doped into $CsPb(Cl_{1-x}Br_x)_3$ NCs, and their PL spectra measured at cryogenic temperature show that the shallow defect state is universally generated ~400 cm^{-1} (50 meV) below the E_g (Figure 1.5).[39, 60] These studies, however, do not report emission from the mid-gap state, proposed by Song and coworkers.[5] This observation strongly supports the cooperative quantum-cutting mechanism proposed by Gamelin and coworkers.[39] Furthermore, as discussed previously, E_g of perovskites can easily be tuned by post-synthetic anion exchange or by tuning halide precursors during syntheses, and many studies report over 100% PLQYs *via* quantum cutting in Yb^{3+}:$CsPb(Cl_{1-x}Br_x)_3$ (Table 1.1).[6, 39, 40, 43, 52] To that end, cryogenic PL measurements of Gd^{3+}:$CsPb(Cl_{1-x}Br_x)_3$ NCs confirm that the defect state is maintained constantly ~400 cm^{-1} below the conduction band in all compositions (Figure 1.5b),[60] supporting the hypothesis that the dopant-induced defect state is involved in sensitizing Yb^{3+} PL for all compositions.

Substitutionally doping Yb^{3+} into either Cs^+ or Pb^{2+} sites in $CsPb(Cl_{1-x}Br_x)_3$ lattice involves charge compensating cation vacancies (V_{Cs} or V_{Pb}) to maintain charge neutrality of the material. Computational work on $CsPbBr_3$ demonstrates formation of shallow trap states by V_{Cs} and V_{Pb},[62] both consistent with the observation of broad defect luminescence from RE^{3+}: $CsPb(Cl_{1-x}Br_x)_3$ NCs.[39, 60] A charge-compensation motif from an analogous material, Gd^{3+}-doped $CsCdBr_3$ SCs, were thoroughly investigated using electron paramagnetic resonance.[63, 64] In these studies, McPherson and coworkers propose coupling of two Gd^{3+} ions with one Cd^{2+} vacancy, spatially located between the Gd^{3+} pair to achieve charge neutrality. This charge compensation motif in Yb^{3+}:$CsPb(Cl_{1-x}Br_x)_3$ also allows simultaneous energy transfer to two Yb^{3+} ions from the V_{Pb} or the dopant-induced defect, which further supports the cooperative quantum-cutting energy-transfer mechanism. This proposal is supported by both experimental and computation studies.[65-67] X-ray absorption fine structure experiments and pair distribution analysis by Kluherz *et al.* confirm substitutional doping of Yb^{3+} ions in the Pb^{2+} sites, adopting the same octahedral coordination environment, accompanied by the formation of V_{Pb} induced by the trivalent dopant in $CsPbCl_3$

lattice.[66] Furthermore, computational studies by Sommer *et al.* report that various configurations of $(2Yb_{Pb} + V_{Pb})^0$ complexes possess a favorable binding energy, suggesting a diverse population of Yb^{3+} pairs distributed across the perovskite lattice (*e.g.* linear or bent configurations of Yb_{Pb}-V_{Pb}-Yb_{Pb} and more).[67] This diverse $(2Yb_{Pb} + V_{Pb})^0$ population has been measured in the form of Yb^{3+} speciation for Yb^{3+}:$CsPbCl_3$ SC in a low-temperature PL experiment.[68] The optical and structural properties of various Yb^{3+} species are studied in further detail in Chapters 2 and 4.

1.4.4 *Quantum-cutting energy-transfer dynamics in Yb^{3+}:$CsPb(Cl_{1-x}Br_x)_3$*

The exceptionally high PLQYs of Yb^{3+}:$CsPb(Cl_{1-x}Br_x)_3$ perovskites can be explained by their unique photophysical properties established by V_{Pb} or the dopant-induced defect state. To achieve near-unity NIR PLQYs, the energy-transfer step from the exciton to the shallow dopant-induced defect state must be substantially faster than the radiative and non-radiative processes native to perovskites. The excitonic state of $CsPbCl_3$ NCs decays within several nanoseconds,[33] and $CsPbBr_3$ NCs experience hot carrier trapping at the native defect sites, occurring on the picosecond timescale.[69] Transient absorption kinetics of Yb^{3+}:$CsPbCl_3$ NCs and solution-processed thin films (Figure 1.6a) show a dramatic decrease in the initial transient-absorption amplitude in the Yb^{3+}-doped samples, suggesting that Yb^{3+} doping introduces a sub-picosecond depopulation pathway from the excitonic state of $CsPbCl_3$ at room temperature.[39, 40] This pathway easily outcompetes other radiative and non-radiative pathways that are native to perovskites, consistent with high PLQYs observed in Yb^{3+}:$CsPbCl_3$ materials.

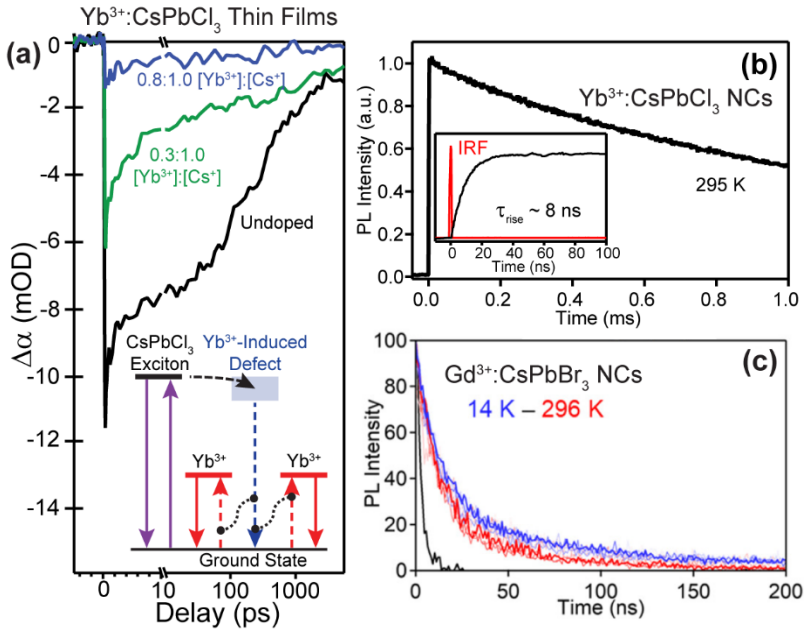

Figure 1.6. (a) Room-temperature transient absorption kinetics (recovery dynamics of the excitonic absorption) of undoped (black), 0.3 [Yb^{3+}]:[Cs^{+}] loading (green), and 0.8 [Yb^{3+}]:[Cs^{+}] loading (blue) $CsPbCl_3$ thin films. *Inset*: proposed cooperative quantum-cutting energy-transfer mechanism. Reprinted with permission from ref. [40]. Copyright 2018 American Chemical Society. **(b)** Room-temperature time-resolved PL data for Yb^{3+} luminescence (λ_{em} = 985 nm) in Yb^{3+}:$CsPbCl_3$ NCs. *Inset*: first 100 ns of the same trace with instrument response function (red). Reprinted with permission from ref. [68]. Copyright 2020 American Physical Society. **(c)** Variable-temperature time-resolved PL data for the near-band edge emission (shallow defect state; $\lambda_{em} \approx$ 550 nm) in Gd^{3+}:$CsPbBr_3$ NCs. The average decay time is reported to be on the order of 10 ns from 14 K (blue) to room temperature (red). Reprinted with permission from ref. [60]. Copyright 2022 American Chemical Society. Note: All the measurements above involve photoexcitation through the perovskite E_g.

Emission from the dopant-induced defect state, however, is not observed in Yb^{3+}:$CsPbCl_3$ at any temperature[39, 68, 70] because the concentration of V_{Pb} formed in the lattice is determined by the concentration of Yb^{3+} ions; *i.e.* the entire V_{Pb} population contributes to quantum cutting, as demonstrated in first-principles electronic structure calculations.[67] Although the dopant-induced defect state is not directly measured in quantum-cutting Yb^{3+}:$CsPbCl_3$ materials, an ~8-ns rise time (Figure 1.6b) for Yb^{3+} $^2F_{5/2} \rightarrow {}^2F_{7/2}$ PL following $CsPbCl_3$ photoexcitation at room temperature provides direct experimental evidence that energy transfer from the perovskite to Yb^{3+} ions proceeds *via* an intermediate state.[68] Furthermore, the luminescence from the dopant-induced defect state in Gd^{3+}:$CsPbBr_3$ NCs also decays on the order of 10s of nanoseconds at room

temperature, confirming that the energy transfer indeed occurs from the V_{Pb} to two Yb^{3+} ions.[60] As discussed above, quantum cutting in other materials involves multipolar coupling between *f-f* transitions of Ln^{3+} ions as the sensitizer and Yb^{3+} as the activator. Therefore, the actual quantum-cutting energy transfer between two Ln^{3+} ions occurs within several microseconds to miliseconds.[20-26] Instead, in Yb^{3+}:$CsPbCl_3$, quantum-cutting energy-transfer involves a Dexter-type exchange mechanism, which is well-documented among molecularly sensitized Ln^{3+} compounds with energy-transfer time constants ranging from 100s of picoseconds to several nanoseconds.[3]

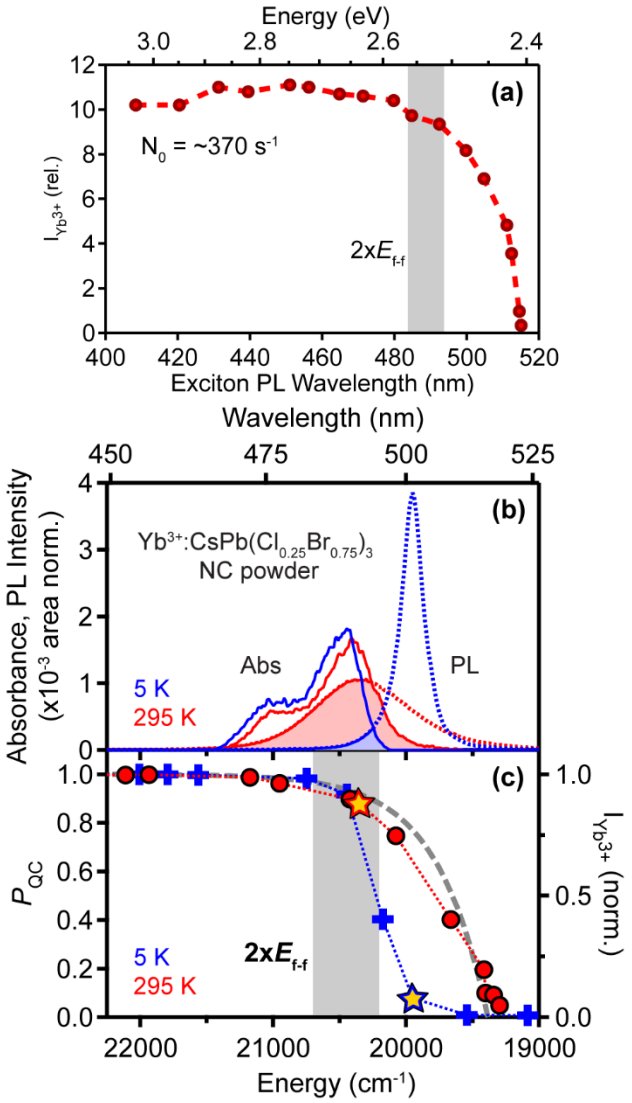

Figure 1.7. (a) Integrated Yb^{3+} $^2F_{5/2} \rightarrow {}^2F_{7/2}$ PL intensities *vs* exciton PL wavelength of Yb^{3+}:$CsPb(Cl_{1-x}Br_x)_3$ NCs (*via* post-synthetic anion exchange) collected at room temperature with a constant NC excitation rate of ~370 s^{-1}. Reprinted with permission from ref. [46]. Copyright 2019 American Chemical Society. **(b)** Yb^{3+}-Yb^{3+} simultaneous pair

absorption ($|^2F_{7/2}, {}^2F_{7/2}\rangle \rightarrow |^2F_{5/2}, {}^2F_{5/2}\rangle$, solid, calculated) and excitonic PL (dotted) spectra of Yb^{3+}:$CsPb(Cl_{0.25}Br_{0.75})_3$ NC powder measured at 5 (blue) and 295 K (red). The filled areas correspond to the donor/acceptor spectral overlap at 5 (blue) and 295 K (pink). Reprinted with permission from ref. [71]. Copyright 2023 American Chemical Society. **(c)** Values of the quantum-cutting energy-transfer probability (P_{QC}, adopted from ρ) at 5 (blue) and 295 K (red) calculated using the Yb^{3+}-Yb^{3+} pair absorption spectra from panel (b) and excitonic PL spectra for Yb^{3+}:$CsPb(Cl_{1-x}Br_x)_3$ ($0.40 \leq x \leq 0.90$), plotted as a function of E_g at 5 and 295 K, respectively. Gray dashed line: reproduction of the data in panel (a). Stars: P_{QC} values calculated from the spectra in panel (b). Reprinted with permission from ref. [71]. Copyright 2023 American Chemical Society.

The energy-transfer rate in Yb^{3+}:$CsPb(Cl_{1-x}Br_x)_3$ can be explained in the framework of Fermi's golden rule in eq 1.1, where the rate of quantum cutting energy transfer (k_{QC}) is described as a function of the electronic coupling of (M_{DA}) and the spectral overlap (ρ) between the donor and acceptor. During quantum-cutting energy transfer in these systems, the donor is the dopant-induced defect state (V_{Pb}) and the acceptor is two Yb^{3+} ions.

$$k_{QC} = \frac{2\pi}{\hbar} |M_{DA}|^2 \rho \tag{1.1}$$

While M_{DA} for Yb^{3+}:$CsPb(Cl_{1-x}Br_x)_3$ is still poorly understood, ρ has been thoroughly investigated. Using anion-exchange reactions, Milstein *et al.* tuned E_g of perovskites from 24600 to 19400 cm^{-1}, while monitoring the Yb^{3+} $^2F_{5/2} \rightarrow {}^2F_{7/2}$ PL intensity at room temperature.[46] The Yb^{3+} PL intensities stay steady when E_g is above the quantum-cutting energy threshold ($2\times E_{f\text{-}f}$) but show a rapid drop when $E_g < 2\times E_{f\text{-}f}$ (Figure 1.7a).[46] In this work, ρ is expected to change as E_g approaches $2\times E_{f\text{-}f}$, given the narrow *f-f* absorption of Yb^{3+} ions. Using calculated Yb^{3+}-Yb^{3+} simultaneous pair absorption ($|^2F_{7/2}, {}^2F_{7/2}\rangle \rightarrow |^2F_{5/2}, {}^2F_{5/2}\rangle$) and excitonic PL spectra of Yb^{3+}:$CsPb(Cl_{1-x}Br_x)_3$ NCs, Roh *et al.* spectrally demonstrated ρ as a function of E_g and temperature and confirmed the critical impact of ρ on quantum-cutting efficiencies (Figures 1.7b, c).[71] When $E_g \approx 2\times E_{f\text{-}f}$, ρ increases dramatically with increasing temperature, enabling efficient quantum-cutting at room temperature. The quantum-cutting efficiencies in the context of thermal energy and E_g are studied in further detail in Chapter 3. The results indicate that a larger range of Yb^{3+}:$CsPb(Cl_{1-x}Br_x)_3$ compositions ($0.0 \leq x \leq 0.8$) can be used to achieve quantum cutting at high temperatures, which is particularly important for their applications in solar technologies.

1.5 Solar applications of Yb^{3+}:$CsPb(Cl_{1-x}Br_x)_3$ perovskites

Due to their unique photophysics and remarkably high PLQYs, Yb^{3+}:$CsPb(Cl_{1-x}Br_x)_3$ perovskites have gained popularity as a cost-effective material with the potential to improve power conversion efficiencies (PCEs) of solar cells beyond the Shockley-Queisser thermodynamic limit.[11, 72] Additionally, vapor-deposited and solution-processed films of the material show equally,[40, 43] if not higher, quantum-cutting efficiencies than NCs. These thin films can reduce the cost of their production significantly for commercial application, compared to NC syntheses that are labor-intensive and require a large volume of solvents. In principle, Yb^{3+}:$CsPb(Cl_{1-x}Br_x)_3$ can be integrated by overlaying the material on top of a working c-Si solar cell (Figure 1.8a).

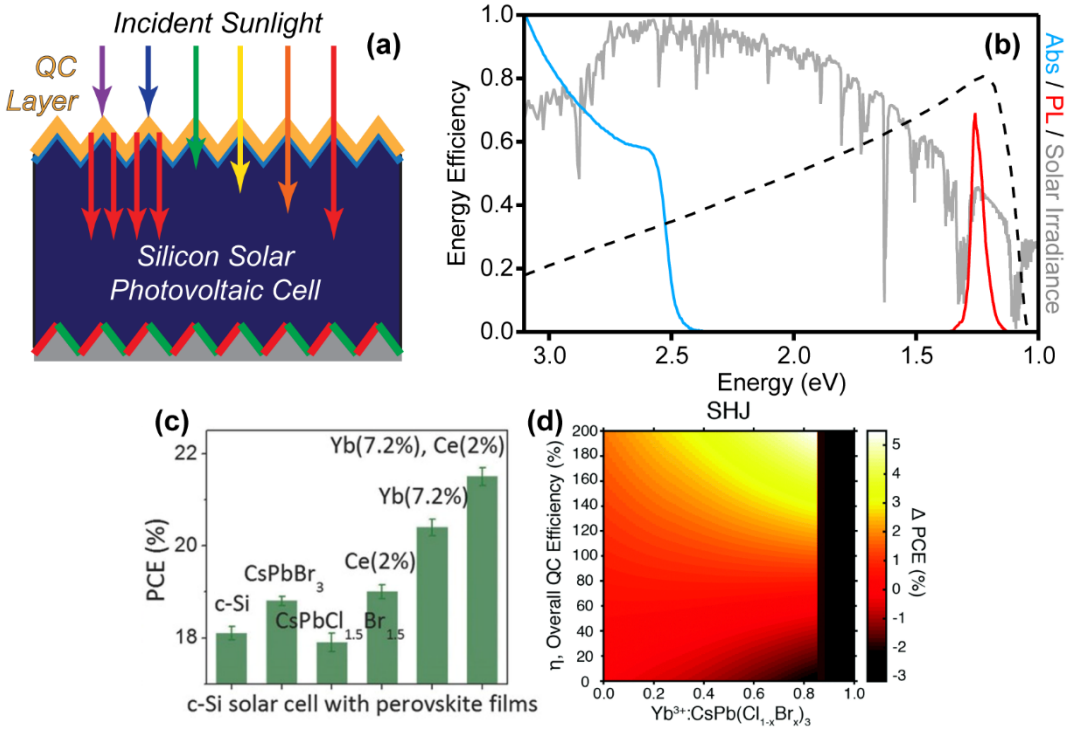

Figure 1.8. (a) Schematic of the proposed quantum-cutting photovoltaic architecture. **(b)** Energy-conversion efficiency of a typical c-Si photovoltaic (dashed black), AM 1.5 G solar spectral irradiance (gray), absorption (blue), PL (red) spectra of Yb^{3+}:$CsPb(Cl_{0.75}Br_{0.25})_3$ NCs at room temperature. Reprinted with permission from ref. [46]. Copyright 2019 American Chemical Society. **(c)** PCEs of c-Si solar cells coated with various perovskite NCs: no perovskites, $CsPbBr_3$, $CsPbCl_{1.5}Br_{1.5}$, Ce^{3+}:$CsPbCl_{1.5}Br_{1.5}$, Yb^{3+}:$CsPbCl_{1.5}Br_{1.5}$, Yb^{3+},Ce^{3+}:$CsPbCl_{1.5}Br_{1.5}$ (left to right). Reprinted with permission from ref. [6]. Copyright 2017 Wiley. **(d)** Detailed-balance calculations of the maximum PCE increase in a Si heterojunction (SHJ) photovoltaic, modeled by adding Yb^{3+}:$CsPb(Cl_{1-x}Br_x)_3$ with NIR PLQYs from 0 to 200%. Reprinted with permission from ref. [73]. Copyright 2019 The Royal Society of Chemistry.

Again, the Yb^{3+} *f-f* transition energy is spectrally well-matched for c-Si solar cells that have poor absorption in the UV region, where Yb^{3+}:$CsPb(Cl_{1-x}Br_x)_3$ absorbs high energy photons and re-emits NIR photons through Yb^{3+} *via* quantum cutting (Figure 1.8b). Deposition of a quantum-cutting Yb^{3+}:$CsPb(Cl_{1-x}Br_x)_3$ NC layer on the surface of commercial c-Si solar cells (area 125 mm × 125 mm) by Song and coworkers reports an increase in PCE of 3.5% (Figure 1.8c).[6, 47] Furthermore, the detailed-balance calculations for PCEs of different photovoltaic materials with Yb^{3+}:$CsPb(Cl_{0.25}Br_{0.75})_3$ show an increase of ~5 and 2%, at 200 and 100% NIR PLQYs, respectively (Figure 1.8d).[73] Although more research efforts on engineering and optimization of the device are required, these results illustrate that Yb^{3+}:$CsPb(Cl_{1-x}Br_x)_3$ is a promising photonic material for the next generation solar technologies.

1.6 Conclusion

Harnessing unique luminescent properties of Yb^{3+} ions and broadband absorption of $CsPb(Cl_{1-x}Br_x)_3$, quantum-cutting Yb^{3+}-doped $CsPb(Cl_{1-x}Br_x)_3$ materials show near-unity PLQYs of 200% (Table 1.1). These strikingly high efficiencies drew significant research interests to investigate their origins and the details of Yb^{3+}-sensitization mechanisms. Aliovalent doping of Yb^{3+} ions into the Pb^{2+} sites of the perovskites introduces extraordinary structural and photophysical properties, including a dopant-induced defect state, which is critical in achieving such high PLQYs. Understanding these mechanistic details of quantum-cutting energy transfer in Yb^{3+}:$CsPb(Cl_{1-x}Br_x)_3$ allowed further optimization and application of these materials. Laboratory-scale integration of these materials to working silicon solar cells has already demonstrated over 3% increase in PCEs.[6, 47] Due to their technological relevance and exceptional efficiencies, Yb^{3+}:$CsPb(Cl_{1-x}Br_x)_3$ materials remain a highly productive area of research for device engineering as well as their photophysical and structural properties.

1.7 References

1. Ovsyankin, V. V., CHAPTER 7 - Spectroscopy of Collective States and Cooperative Transitions in Disordered Rare-Earth Activated Solids. In *Modern Problems in Condensed Matter Sciences*, Kaplyanskii, A. A.; Macfarlane, R. M., Eds. Elsevier: 1987; Vol. 21, pp 343-480.
2. Werts, M. H. V. Making Sense of Lanthanide Luminescence. *Science Progress (1933-)* **2005,** *88*, 101-131.

3. Bünzli, J.-C. G. On the Design of Highly Luminescent Lanthanide Complexes. *Coord. Chem. Rev.* **2015,** *293-294*, 19-47.
4. Mir, W. J.; Sheikh, T.; Arfin, H.; Xia, Z.; Nag, A. Lanthanide Doping in Metal Halide Perovskite Nanocrystals: Spectral Shifting, Quantum Cutting and Optoelectronic Applications. *NPG Asia Mater.* **2020,** *12*, 9.
5. Pan, G.; Bai, X.; Yang, D.; Chen, X.; Jing, P.; Qu, S.; Zhang, L.; Zhou, D.; Zhu, J.; Xu, W.; Dong, B.; Song, H. Doping Lanthanide into Perovskite Nanocrystals: Highly Improved and Expanded Optical Properties. *Nano Lett.* **2017,** *17*, 8005-8011.
6. Zhou, D.; Liu, D.; Pan, G.; Chen, X.; Li, D.; Xu, W.; Bai, X.; Song, H. Cerium and Ytterbium Codoped Halide Perovskite Quantum Dots: A Novel and Efficient Downconverter for Improving the Performance of Silicon Solar Cells. *Adv. Mater.* **2017,** *29*, 1704149.
7. Dieke, G. H., *Spectra and Energy Levels of Rare Earth Ions in Crystals*. Interscience Publishers: New York, 1968.
8. Yaiphaba, N.; Ningthoujam, R. S.; Singh, N. R.; Vatsa, R. K. Luminescence Properties of Redispersible Tb^{3+}-Doped $GdPO_4$ Nanoparticles Prepared by an Ethylene Glycol Route. *Eur. J. Inorg. Chem.* **2010,** *2010*, 2682-2687.
9. Auzel, F. Upconversion and Anti-Stokes Processes with *f* and *d* Ions in Solids. *Chem. Rev.* **2004,** *104*, 139-174.
10. Wegh, R. T.; Donker, H.; Oskam, K. D.; Meijerink, A. Visible Quantum Cutting in $LiGdF_4:Eu^{3+}$ Through Downconversion. *Science* **1999,** *283*, 663-666.
11. Shockley, W.; Queisser, H. J. Detailed Balance Limit of Efficiency of *p-n* Junction Solar Cells. *J. Appl. Phys.* **1961,** *32*, 510-519.
12. Trupke, T.; Green, M. A.; Würfel, P. Improving Solar Cell Efficiencies by Down-Conversion of High-Energy Photons. *J. Appl. Phys.* **2002,** *92*, 1668-1674.
13. Van der Ende, B. M.; Aarts, L.; Meijerink, A. Lanthanide Ions as Spectral Converters for Solar Cells. *Phys. Chem. Chem. Phys.* **2009,** *11*, 11081-11095.
14. Schulze, T. F.; Schmidt, T. W. Photochemical Upconversion: Present Status and Prospects for Its Application to Solar Energy Conversion. *Energy Environ. Sci.* **2015,** *8*, 103-125.
15. Dexter, D. L. Two Ideas on Energy Transfer Phenomena: Ion-Pair Effects Involving the OH Stretching Mode, and Sensitization of Photovoltaic Cells. *J. Lumin.* **1979,** *18-19*, 779-784.
16. Geacintov, N.; Pope, M.; Vogel, F. Effect of Magnetic Field on the Fluorescence of Tetracene Crystals: Exciton Fission. *Phys. Rev. Lett.* **1969,** *22*, 593-596.
17. Hanna, M. C.; Nozik, A. J. Solar Conversion Efficiency of Photovoltaic and Photoelectrolysis Cells with Carrier Multiplication Absorbers. *J. Appl. Phys.* **2006,** *100*, 074510.
18. Beard, M. C.; Knutsen, K. P.; Yu, P.; Luther, J. M.; Song, Q.; Metzger, W. K.; Ellingson, R. J.; Nozik, A. J. Multiple Exciton Generation in Colloidal Silicon Nanocrystals. *Nano Lett.* **2007,** *7*, 2506-2512.
19. Nozik, A. J.; Beard, M. C.; Luther, J. M.; Law, M.; Ellingson, R. J.; Johnson, J. C. Semiconductor Quantum Dots and Quantum Dot Arrays and Applications of Multiple Exciton Generation to Third-Generation Photovoltaic Solar Cells. *Chem. Rev.* **2010,** *110*, 6873-6890.
20. Vergeer, P.; Vlugt, T. J. H.; Kox, M. H. F.; den Hertog, M. I.; van der Eerden, J. P. J. M.; Meijerink, A. Quantum Cutting by Cooperative Energy Transfer in $Yb_xY_{1-x}PO_4:Tb^{3+}$. *Phys. Rev. B* **2005,** *71*, 014119.
21. Chen, D.; Wang, Y.; Yu, Y.; Huang, P.; Weng, F. Near-Infrared Quantum Cutting in Transparent Nanostructured Glass Ceramics. *Opt. Lett.* **2008,** *33*, 1884-1886.

22. Van der Ende, B. M.; Aarts, L.; Meijerink, A. Near-Infrared Quantum Cutting for Photovoltaics. *Adv. Mater.* **2009,** *21*, 3073-3077.
23. Xie, L.; Wang, Y.; Zhang, H. Near-Infrared Quantum Cutting in $YPO_4:Yb^{3+}$, Tm^{3+} *via* Cooperative Energy Transfer. *Appl. Phys. Lett.* **2009,** *94*, 061905.
24. Eilers, J. J.; Biner, D.; van Wijngaarden, J. T.; Krämer, K.; Güdel, H.-U.; Meijerink, A. Efficient Visible to Infrared Quantum Cutting Through Downconversion with the Er^{3+}–Yb^{3+} Couple in $Cs_3Y_2Br_9$. *Appl. Phys. Lett.* **2010,** *96*, 151106.
25. Meijer, J.-M.; Aarts, L.; van der Ende, B. M.; Vlugt, T. J. H.; Meijerink, A. Downconversion for Solar Cells in $YF_3:Nd^{3+}$, Yb^{3+}. *Phys. Rev. B* **2010,** *81*, 035107.
26. Lin, H.; Chen, D.; Yu, Y.; Yang, A.; Wang, Y. Near-Infrared Quantum Cutting in Ho^{3+}/Yb^{3+} Codoped Nanostructured Glass Ceramic. *Opt. Lett.* **2011,** *36*, 876-878.
27. Wang, Z.; Meijerink, A. Dye-Sensitized Downconversion. *J. Phys. Chem. Lett.* **2018,** *9*, 1522-1526.
28. Richards, B. S. Enhancing the Performance of Silicon Solar Cells *via* the Application of Passive Luminescence Conversion Layers. *Sol. Energy Mater. Sol. Cells* **2006,** *90*, 2329-2337.
29. Martín-Rodríguez, R.; Geitenbeek, R.; Meijerink, A. Incorporation and Luminescence of Yb^{3+} in CdSe Nanocrystals. *J. Am. Chem. Soc.* **2013,** *135*, 13668-13671.
30. Creutz, S. E.; Fainblat, R.; Kim, Y.; De Siena, M. C.; Gamelin, D. R. A Selective Cation Exchange Strategy for the Synthesis of Colloidal Yb^{3+}-Doped Chalcogenide Nanocrystals with Strong Broadband Visible Absorption and Long-Lived Near-Infrared Emission. *J. Am. Chem. Soc.* **2017,** *139*, 11814-11824.
31. Akkerman, Q. A.; D'Innocenzo, V.; Accornero, S.; Scarpellini, A.; Petrozza, A.; Prato, M.; Manna, L. Tuning the Optical Properties of Cesium Lead Halide Perovskite Nanocrystals by Anion Exchange Reactions. *J. Am. Chem. Soc.* **2015,** *137*, 10276-10281.
32. Nedelcu, G.; Protesescu, L.; Yakunin, S.; Bodnarchuk, M. I.; Grotevent, M. J.; Kovalenko, M. V. Fast Anion-Exchange in Highly Luminescent Nanocrystals of Cesium Lead Halide Perovskites ($CsPbX_3$, X = Cl, Br, I). *Nano Lett.* **2015,** *15*, 5635-5640.
33. Protesescu, L.; Yakunin, S.; Bodnarchuk, M. I.; Krieg, F.; Caputo, R.; Hendon, C. H.; Yang, R. X.; Walsh, A.; Kovalenko, M. V. Nanocrystals of Cesium Lead Halide Perovskites ($CsPbX_3$, X = Cl, Br, and I): Novel Optoelectronic Materials Showing Bright Emission with Wide Color Gamut. *Nano Lett.* **2015,** *15*, 3692-3696.
34. Ten Brinck, S.; Infante, I. Surface Termination, Morphology, and Bright Photoluminescence of Cesium Lead Halide Perovskite Nanocrystals. *ACS Energy Lett.* **2016,** *1*, 1266-1272.
35. Akkerman, Q. A.; Rainò, G.; Kovalenko, M. V.; Manna, L. Genesis, Challenges and Opportunities for Colloidal Lead Halide Perovskite Nanocrystals. *Nat. Mater.* **2018,** *17*, 394-405.
36. Creutz, S. E.; Crites, E. N.; De Siena, M. C.; Gamelin, D. R. Anion Exchange in Cesium Lead Halide Perovskite Nanocrystals and Thin Films Using Trimethylsilyl Halide Reagents. *Chem. Mater.* **2018,** *30*, 4887-4891.
37. Dey, A.*, et al.* State of the Art and Prospects for Halide Perovskite Nanocrystals. *ACS Nano* **2021,** *15*, 10775-10981.
38. Maes, J.; Balcaen, L.; Drijvers, E.; Zhao, Q.; De Roo, J.; Vantomme, A.; Vanhaecke, F.; Geiregat, P.; Hens, Z. Light Absorption Coefficient of $CsPbBr_3$ Perovskite Nanocrystals. *J. Phys. Chem. Lett.* **2018,** *9*, 3093-3097.

39. Milstein, T. J.; Kroupa, D. M.; Gamelin, D. R. Picosecond Quantum Cutting Generates Photoluminescence Quantum Yields Over 100% in Ytterbium-Doped $CsPbCl_3$ Nanocrystals. *Nano Lett.* **2018,** *18*, 3792-3799.
40. Kroupa, D. M.; Roh, J. Y.; Milstein, T. J.; Creutz, S. E.; Gamelin, D. R. Quantum-Cutting Ytterbium-Doped $CsPb(Cl_{1-x}Br_x)_3$ Perovskite Thin Films with Photoluminescence Quantum Yields over 190%. *ACS Energy Lett.* **2018,** *3*, 2390-2395.
41. Zhang, X.; Zhang, Y.; Zhang, X.; Yin, W.; Wang, Y.; Wang, H.; Lu, M.; Li, Z.; Gu, Z.; Yu, W. W. Yb^{3+} and Yb^{3+}/Er^{3+} Doping for Near-Infrared Emission and Improved Stability of $CsPbCl_3$ Nanocrystals. *J. Mater. Chem. C* **2018,** *6*, 10101-10105.
42. Cohen, T. A.; Milstein, T. J.; Kroupa, D. M.; MacKenzie, J. D.; Luscombe, C. K.; Gamelin, D. R. Quantum-Cutting Yb^{3+}-Doped Perovskite Nanocrystals for Monolithic Bilayer Luminescent Solar Concentrators. *J. Mater. Chem. A* **2019,** *7*, 9279-9288.
43. Crane, M. J.; Kroupa, D. M.; Roh, J. Y.; Anderson, R. T.; Smith, M. D.; Gamelin, D. R. Single-Source Vapor Deposition of Quantum-Cutting Yb^{3+}:$CsPb(Cl_{1-x}Br_x)_3$ and Other Complex Metal-Halide Perovskites. *ACS Appl. Energy Mater.* **2019,** *2*, 4560-4565.
44. Erickson, C. S.; Crane, M. J.; Milstein, T. J.; Gamelin, D. R. Photoluminescence Saturation in Quantum-Cutting Yb^{3+}-Doped $CsPb(Cl_{1-x}Br_x)_3$ Perovskite Nanocrystals: Implications for Solar Downconversion. *J. Phys. Chem. C* **2019,** *123*, 12474-12484.
45. Luo, X.; Ding, T.; Liu, X.; Liu, Y.; Wu, K. Quantum-Cutting Luminescent Solar Concentrators Using Ytterbium-Doped Perovskite Nanocrystals. *Nano Lett.* **2019,** *19*, 338-341.
46. Milstein, T. J.; Kluherz, K. T.; Kroupa, D. M.; Erickson, C. S.; De Yoreo, J. J.; Gamelin, D. R. Anion Exchange and the Quantum-Cutting Energy Threshold in Ytterbium-Doped $CsPb(Cl_{1-x}Br_x)_3$ Perovskite Nanocrystals. *Nano Lett.* **2019,** *19*, 1931-1937.
47. Zhou, D.; Sun, R.; Xu, W.; Ding, N.; Li, D.; Chen, X.; Pan, G.; Bai, X.; Song, H. Impact of Host Composition, Codoping, or Tridoping on Quantum-Cutting Emission of Ytterbium in Halide Perovskite Quantum Dots and Solar Cell Applications. *Nano Lett.* **2019,** *19*, 6904-6913.
48. Cai, T.; Wang, J.; Li, W.; Hills-Kimball, K.; Yang, H.; Nagaoka, Y.; Yuan, Y.; Zia, R.; Chen, O. Mn^{2+}/Yb^{3+} Codoped $CsPbCl_3$ Perovskite Nanocrystals with Triple-Wavelength Emission for Luminescent Solar Concentrators. *Adv. Sci.* **2020,** *7*, 2001317.
49. Ding, N.; Xu, W.; Zhou, D.; Ji, Y.; Wang, Y.; Sun, R.; Bai, X.; Zhou, J.; Song, H. Extremely Efficient Quantum-Cutting Cr^{3+}, Ce^{3+}, Yb^{3+} Tridoped Perovskite Quantum Dots for Highly Enhancing the Ultraviolet Response of Silicon Photodetectors with External Quantum Efficiency Exceeding 70%. *Nano Energy* **2020,** *78*, 105278.
50. Ishii, A.; Miyasaka, T. Sensitized Yb^{3+} Luminescence in $CsPbCl_3$ Film for Highly Efficient Near-Infrared Light-Emitting Diodes. *Adv. Sci.* **2020,** *7*, 1903142.
51. Zeng, M.; Artizzu, F.; Liu, J.; Singh, S.; Locardi, F.; Mara, D.; Hens, Z.; Van Deun, R. Boosting the Er^{3+} 1.5 μm Luminescence in $CsPbCl_3$ Perovskite Nanocrystals for Photonic Devices Operating at Telecommunication Wavelengths. *ACS Appl. Nano Mater.* **2020,** *3*, 4699-4707.
52. Zhu, Y.; Pan, G.; Shao, L.; Yang, G.; Xu, X.; Zhao, J.; Mao, Y. Effective Infrared Emission of Erbium Ions Doped Inorganic Lead Halide Perovskite Quantum Dots By Sensitization of Ytterbium Ions. *J. Alloys Compd.* **2020,** *835*, 155390.
53. Chang, W. J.; Irgen-Gioro, S.; Padgaonkar, S.; López-Arteaga, R.; Weiss, E. A. Photoredox-Mediated Sensitization of Lanthanide Dopants by Perovskite Nanocrystals. *J. Phys. Chem. C* **2021,** *125*, 25634-25642.

54. Huang, H.; Li, R.; Jin, S.; Li, Z.; Huang, P.; Hong, J.; Du, S.; Zheng, W.; Chen, X.; Chen, D. Ytterbium-Doped $CsPbCl_3$ Quantum Cutters for Near-Infrared Light-Emitting Diodes. *ACS Appl. Mater. Interfaces* **2021,** *13*, 34561-34571.
55. Xu, K.; Chen, D.; Huang, D.; Zhu, H. Thermally Stable Emission from Yb^{3+}-doped $CsPbCl_3$ Nanocrystals. *J. Lumin.* **2021,** *240*, 118464.
56. Yang, G.; Zheng, C.; Zhu, Y.; Li, X.; Huang, J.; Xu, X.; Liu, W.; Cui, S.; Pan, G. Efficient Quantum Cutting of Lanthanum and Ytterbium Ions Co-Doped Perovskite Quantum Dots Towards Improving the Ultraviolet Response of Silicon-Based Photodetectors. *J. Alloys Compd.* **2022,** *921*, 166097.
57. Ryan, J. L.; Jørgensen, C. K. Absorption Spectra of Octahedral Lanthanide Hexahalides. *J. Phys. Chem.* **1966,** *70*, 2845-2857.
58. Dorenbos, P.; Josef, A.; de Haas, J. T. M.; Krämer, K. W. Vacuum Referred Binding Energies of the Lanthanides in Chloride, Bromide, and Iodide Compounds. *J. Lumin.* **2019,** *208*, 463-467.
59. Jørgensen, C. K., Electron Transfer Spectra. In *Progress in Inorganic Chemistry. Volume 12*, Lippard, S. J., Ed. New York, N.Y. : Wiley: New York, N.Y., 1970; pp 101-158.
60. Milstein, T. J.; Roh, J. Y. D.; Jacoby, L. M.; Crane, M. J.; Sommer, D. E.; Dunham, S. T.; Gamelin, D. R. Ubiquitous Near-Band-Edge Defect State in Rare-Earth-Doped Lead-Halide Perovskites. *Chem. Mater.* **2022,** *34*, 3759-3769.
61. Watanabe, K.; Koshimizu, M.; Yanagida, T.; Fujimoto, Y.; Asai, K. Luminescence and Scintillation Properties of La- and La, Ag-Doped $CsPbCl_3$ Single Crystals. *Jpn. J. Appl. Phys.* **2016,** *55*, 02BC20.
62. Kang, J.; Wang, L.-W. High Defect Tolerance in Lead Halide Perovskite $CsPbBr_3$. *J. Phys. Chem. Lett.* **2017,** *8*, 489-493.
63. Henling, L. M.; McPherson, G. L. EPR Spectra of Magnetically Coupled Pairs of Gd^{3+} Ions in Crystals of $CsMgCl_3$, $CsMgBr_3$, and $CsCdBr_3$. *Phys. Rev. B* **1977,** *16*, 4756-4760.
64. McPherson, G. L.; Henling, L. M. EPR Spectrum of Coupled Pairs of Gd^{3+} Ions in Single Crystals of $CsCdBr_3$. *Phys. Rev. B* **1977,** *16*, 1889-1892.
65. Li, X.; Duan, S.; Liu, H.; Chen, G.; Luo, Y.; Ågren, H. Mechanism for the Extremely Efficient Sensitization of Yb^{3+}Luminescence in $CsPbCl_3$ Nanocrystals. *J. Phys. Chem. Lett.* **2019,** *10*, 487-492.
66. Kluherz, K. T.; Mergelsberg, S. T.; Sommer, D. E.; Roh, J. Y. D.; Saslow, S. A.; Biner, D.; Krämer, K. W.; Dunham, S. T.; De Yoreo, J. J.; Gamelin, D. R. Defect Structure in Quantum-Cutting Yb^{3+}-Doped $CsPbCl_3$ Perovskites Probed by X-Ray Absorption and Atomic Pair Distribution Function Analysis. *Phys. Rev. Mater.* **2022,** *6*, 074601.
67. Sommer, D. E.; Gamelin, D. R.; Dunham, S. T. Defect Formation in Yb-Doped $CsPbCl_3$ from First Principles with Implications for Quantum Cutting. *Phys. Rev. Mater.* **2022,** *6*, 025404.
68. Roh, J. Y. D.; Smith, M. D.; Crane, M. J.; Biner, D.; Milstein, T. J.; Krämer, K. W.; Gamelin, D. R. Yb^{3+} Speciation and Energy-Transfer Dynamics in Quantum-Cutting Yb^{3+}-Doped $CsPbCl_3$ Perovskite Nanocrystals and Single Crystals. *Phys. Rev. Mater.* **2020,** *4*, 105405.
69. Chen, J.; Messing, M. E.; Zheng, K.; Pullerits, T. Cation-Dependent Hot Carrier Cooling in Halide Perovskite Nanocrystals. *J. Am. Chem. Soc.* **2019,** *141*, 3532-3540.
70. Stefanski, M.; Ptak, M.; Sieradzki, A.; Strek, W. Optical Characterization of Yb^{3+}:$CsPbCl_3$ Perovskite Powder. *Chem. Eng. J.* **2021,** *408*, 127347.
71. Roh, J. Y. D.; Milstein, T. J.; Gamelin, D. R. Negative Thermal Quenching in Quantum-Cutting Yb^{3+}-Doped $CsPb(Cl_{1-x}Br_x)_3$ Perovskite Nanocrystals. *Submitted*.

72. Sun, R.; Zhou, D.; Song, H. Rare Earth Doping in Perovskite Luminescent Nanocrystals and Photoelectric Devices. *Nano Sel.* **2022,** *3*, 531-554.
73. Crane, M. J.; Kroupa, D. M.; Gamelin, D. R. Detailed-Balance Analysis of Yb^{3+}:$CsPb(Cl_{1-x}Br_x)_3$ Quantum-Cutting Layers for High-Efficiency Photovoltaics Under Real-World Conditions. *Energy Environ. Sci.* **2019,** *12*, 2486-2495.

Chapter 2. Yb^{3+} Speciation and Energy-Transfer Dynamics in Quantum-Cutting Yb^{3+}-Doped $CsPbCl_3$ Perovskite Nanocrystals and Single Crystals

2.1 Overview

Yb^{3+}-doped inorganic metal-halide perovskites (Yb^{3+}:$CsPbX_3$, X = Cl, Br) have recently been discovered to display highly efficient quantum cutting, in which the energy from individual blue or UV photons absorbed by the material is re-emitted in the form of *pairs* of near-infrared photons by Yb^{3+} dopants. Experimental photoluminescence quantum yields approaching 200% have been reported. As the first quantum-cutting materials that combine such high photoluminescence quantum yields with strong, broadband absorption in the visible, these materials offer unique opportunities for enhancing the efficiencies of solar technologies. Little is known about the fundamental origins of this quantum cutting, however. Here, we describe variable-temperature and time-resolved photoluminescence studies of Yb^{3+}:$CsPbCl_3$ in two disparate forms - colloidal nanocrystals and macroscopic single crystals. Both forms show very similar spectroscopic properties, demonstrating that quantum cutting is an intrinsic property of the Yb^{3+}:$CsPbX_3$ composition itself. Diverse Yb^{3+} speciation is observed in both forms by low-temperature photoluminescence spectroscopy, but remarkably, quantum cutting is dominated by the same specific Yb^{3+} species in both cases. Time-resolved photoluminescence measurements provide direct evidence of the previously hypothesized intermediate state in the quantum-cutting mechanism. This intermediate state mediates relaxation from the photogenerated excited state of the perovskite to the emissive excited state of Yb^{3+}, and hence is of critical mechanistic importance. At room temperature, this intermediate state is populated within a few picoseconds and has a decay time of only ~7 ns in both nanocrystalline and single-crystal Yb^{3+}:$CsPbCl_3$. The mechanistic implications of these observations are discussed. These results provide valuable information about characteristics of this unique quantum cutter that will aid its optimization and application in solar technologies.

2.2 Introduction

For several decades, researchers have strived to develop materials and technologies that can improve the efficiencies of solar cells beyond the so-called Schockley-Queisser thermodynamic limit of ca. 32% for a single-junction photovoltaic [1, 2]. One strategy that has generated a lot of interest involves splitting the energies of individual solar photons to generate multiple lower-energy electron-hole pairs in the device, thus increasing the solar photocurrent and reducing thermalization losses. For example, certain organic chromophores such as tetracene have the capacity to split the energy of a high-energy photogenerated singlet excited state by populating two triplet excited states in neighboring molecules ("singlet fission"), each with roughly half of the initial photon's energy [3-5]. Similarly, semiconductor quantum dots (QD) can show "multiple exciton generation", in which a photogenerated upper excited state of the QD can cross-relax by promoting one (or more) additional electron(s) across the gap to yield two (or more) electron-hole pairs within the same QD, *i.e.*, bi- or multi-excitons [5-7]. In principle, these materials can then be used to generate photocurrents from high-energy solar photons at a greater rate than in traditional photovoltaics, but extraction of the excitation energy poses major challenges because of competing nonradiative recombination channels (*e.g.*, Auger), the need to introduce additional energy- or charge-transfer steps, or the need to re-engineer the underlying solar cell to integrate the new component at the expense of its baseline performance.

In phosphor research, an analogous photomultiplication process has been investigated in lanthanide-containing materials, referred to as "quantum cutting" [8-15]. A common rendition involves Pr^{3+} and Yb^{3+} co-doped into inorganic host crystals [9, 11]. Photoexcitation of the Pr^{3+} dopant with a blue photon is followed by non-radiative energy transfer to generate two excited Yb^{3+} ions. A major advantage of quantum cutting is that the resulting Yb^{3+} excited states are good photon emitters, in contrast with the dark triplet states generated *via* singlet fission. This advantage makes it feasible to extract the excitation energy photonically rather than *via* charge separation and collection or *via* a separate triplet-harvesting intermediate species. The two excited Yb^{3+} ions generated by quantum cutting can simply re-emit the energy of the blue photon in the form of two NIR photons, both suitable for capture by an underlying photovoltaic. In these systems, however, Pr^{3+} and other lanthanides are poor sensitizers because of their sharp and weak absorption features. Broadband sensitization has been explored but introduces additional loss channels.

Recently, Yb^{3+}-doped $CsPbX_3$ (Yb^{3+}:$CsPbX_3$, X = Cl, Br) has emerged as an attractive material

capable of highly efficient quantum cutting [15-25], achieving photoluminescence quantum yields (PLQYs) approaching 200% [16, 17]. First prepared as colloidal nanocrystals (NCs) [15, 16], efficient quantum cutting has now also been demonstrated in both solution-processed [17] and vapor-deposited [21] $CsPbX_3$ thin films. A key distinction between this material and all previous quantum-cutting materials is its strong and broadband absorption at the energies relevant for quantum cutting. This feature allows much greater harvesting of solar photons by Yb^{3+}:$CsPbX_3$ than by all-lanthanide quantum cutters. Moreover, the composition tunability of the $CsPbX_3$ absorber material allows the absorption threshold to be tailored to minimize thermalization losses, and quantum-cutting energy efficiencies over 90% have been demonstrated for converting absorbed blue photons into emitted NIR photons [19]. Based on these properties, detailed-balance calculations have predicted double-digit (relative) improvements in the maximum theoretical power-conversion efficiencies of various photovoltaics when interfaced with these unique materials, including of state-of-the-art Si heterojunction solar cells [22]. Experimental results interfacing quantum-cutting Yb^{3+}-doped $CsPbX_3$ NCs with polycrystalline Si and CIGS photovoltaics have already demonstrated power-conversion efficiency enhancements as large as 20% (relative) [15, 23]. Given the unique optoelectronic characteristics of these quantum-cutting materials and their preparative flexibility, other technologies such as high-performance transparent luminescent solar concentrators [18, 20], high-efficiency NIR light-emitting diodes [24], or telecommunications phosphors [25] based on Yb^{3+}-doped $CsPbX_3$ and related compositions also become viable.

Because Yb^{3+}-doped metal-halide perovskites are a newly discovered composition of matter, the fundamental origins of their exceptional photophysics remain largely unresolved. One reason for their high quantum-cutting efficiency appears to be the extremely rapid depopulation of the photogenerated $CsPbX_3$ exciton upon introduction of Yb^{3+} dopants. Transient-absorption measurements [16, 17] have shown exciton depopulation within just a few picoseconds associated with Yb^{3+} doping, making quantum cutting competitive with other non-productive exciton trapping or recombination processes. Curiously, energy transfer to Yb^{3+} in other quantum cutters generally requires much more time than this because of the highly shielded *f*-shell valence orbitals involved in the Yb^{3+} *f-f* excitation, exacerbated by the high ionicity of common host lattices. Using La^{3+} as a surrogate trivalent dopant, photoluminescence (PL) from a shallow "dopant-induced defect state" was observed, and this state was hypothesized to play a critical role as an intermediate state in this material's quantum cutting [16]. Transient absorption showed very similar picosecond

exciton depopulation upon doping $CsPbCl_3$ NCs with La^{3+} as found with Yb^{3+} [16], supporting that hypothesis. The dopant-induced defect was proposed to arise from the need for charge compensation when substituting Yb^{3+} for Pb^{2+}. Several charge-compensating defects could conceivably form in this material, and a charge-neutral defect cluster involving Yb^{3+}-V_{Pb}-Yb^{3+} was hypothesized as a plausible motif by analogy with the "McPherson pairs" found in lanthanide-doped $CsCdX_3$ and related lattices [26, 27]. Computational work supports the proposal that such a charge-neutral defect cluster can help to steer energy toward Yb^{3+} dopants [28]. Despite the circumstantial evidence, however, there is to date no *direct* experimental evidence of the involvement of an intermediate state in the quantum cutting displayed by Yb^{3+}:$CsPbX_3$. Additional fundamental studies are required to unravel the properties of this unique material.

Here, we report results from variable-temperature and time-resolved PL (TRPL) studies of Yb^{3+}:$CsPbX_3$ NCs, as well as parallel results obtained for a Yb^{3+}:$CsPbX_3$ single crystal (SC) of macroscopic dimensions grown by the Bridgman method. Remarkably, these two disparate forms of the same composition show nearly indistinguishable spectroscopic characteristics, including nearly identical Yb^{3+} *f-f* spectra that confirm that the same Yb^{3+} species is responsible for quantum cutting in both nano- and macroscopic crystals. Most surprisingly, both materials also show nearly identical few-nanosecond rise times in the Yb^{3+} PL generated by semiconductor photoexcitation. This result provides the first direct experimental evidence of a discrete intermediate state involved in the quantum cutting mechanism, and its preservation in both nano- and macroscopic crystals with very different surface-to-volume ratios and grown under very different conditions demonstrates its intrinsic origin. With this information in hand, the electronic-structure origins of quantum cutting in this material are discussed. The data further indicate the presence of upstream losses prior to energy capture by Yb^{3+}, as well as energy migration and trapping following quantum cutting, that both reduce the quantum-cutting efficiencies. The NCs show fewer losses in both steps, consistent with their higher PLQYs. These results improve our understanding of the photophysics and electronic structure of this unique material, and the insights from these measurements will help to inform future computational or experimental work including material optimization for device applications.

2.3 Experimental

2.3.1 *NC synthesis, SC growth, and general materials characterization*

Yb^{3+}:$CsPbCl_3$ NCs were synthesized as detailed previously [16]. Large crystals of Yb^{3+}-doped $CsPbCl_3$ were grown from melts of stoichiometric admixtures of precursors by the Bridgman technique. Additional synthesis and crystal-growth details are provided in Section 2.8 Appendix. Transmission electron microscopy (TEM) images were obtained using a FEI TECNAI F20 microscope operating at 200 kV. TEM samples were prepared by dropcasting NCs onto carbon-coated copper grids from TED Pella, Inc. Inductively coupled plasma-atomic emission spectroscopy (ICP-AES, PerkinElmer 8300) was used to determine elemental composition. NCs were digested in concentrated nitric acid overnight with sonication for ICP-AES. Powder X-ray diffraction (XRD) data were collected using a Bruker D8 Discover with a high-efficiency IμS microfocus X-ray source for Cu Kα radiation (50 kV, 1 mA). All Yb^{3+} concentrations in $CsPbCl_3$ are reported as the B-site cation mole fraction (in percentage). For NC XRD, colloidal NCs were dropcast onto a silicon substrate. A portion of the Bridgman sample was powdered, and those microcrystals were used to obtain powder XRD data for this sample.

2.3.2 *Spectroscopic measurements*

Samples for PL measurements were prepared by dropcasting colloidal NCs onto quartz discs, and by sealing a monolithic SC fragment inside a quartz tube under a partial pressure of helium gas. These samples were cooled to 5 K in a helium flow cryostat. Temperatures were varied between 5 and 295 K, and PL data were measured at each temperature using a 375 nm LED (0.3 $\mu W/cm^2$) for excitation. For NIR photoexcitation measurements, samples were excited with a CW Ti:Sapphire laser (Coherent Mira-HP in CW mode). PL spectra were measured using a LN_2-cooled silicon CCD camera mounted on a 0.3 m single monochromator with a spectral bandwidth of about 0.03 nm. Absolute PLQY measurements were performed at room temperature using a 5.3 inch teflon-based integrating sphere. The samples were directly excited with a 375 nm LED and attenuated with neutral density filters as needed, and the signal was measured using the CCD camera as described above. PLQY was calculated using eq 2.1, where N indicates number of photons, I indicates the spectrally corrected intensity of the emitted light, and E indicates the spectrally corrected excitation intensity:

$$PLQY = \frac{N_{em}}{N_{abs}} = \frac{\int I_{sample}(\lambda) - I_{ref}(\lambda) d\lambda}{\int E_{ref}(\lambda) - E_{sample}(\lambda) d\lambda} . \quad (2.1)$$

The integrating sphere setup was routinely calibrated using well-characterized dye emission standards including coumarin 153, rhodamine 6G, and IR 140. All steady-state PL spectra were corrected for the instrument response.

Photoexcitation for TRPL measurements was provided by a liquid dye laser (Exalite 404 dye, 4.4×10^{-4} M) pumped by an Ekspla Nd:YAG laser (355 nm) firing at a repetition rate of 50 Hz with a pulse width of about 30 ps. The fluence at the sample was held at ~100 nJ/cm^2 per pulse, which corresponds to about 0.01 absorbed photons per NC per pulse at room temperature. The NIR PL was focused into a monochromator with a spectral bandwidth of about 6 nm, detected by a Hamamatsu InGaAs/InP NIR PMT, and signals were recorded using a multichannel scaler or a digital oscilloscope.

2.4 **Results and analysis**

2.4.1 *Structure*

Figure 2.1 summarizes structural data collected for representative Yb^{3+}-doped $CsPbCl_3$ NCs ([Yb^{3+}] = 4.3%) and a Bridgman SC ([Yb^{3+}] = 2%, nominal). The TEM image in Figure 2.1a shows nanocrystallites of Yb^{3+}-doped $CsPbCl_3$ with average edge lengths of ~11.6 nm (surveying ~350 NCs), consistent with previous results from the same synthesis method [16, 19, 20, 29]. Figure 2.1b shows a photograph of a Yb^{3+}-doped $CsPbCl_3$ SC having ca. 3 × 2 × 2 mm dimensions, sealed inside a quartz tube under a helium atmosphere. Powder XRD patterns collected from both the NCs and the SC sample ((Figure 2.1c), powdered SC sample used) show intensities consistent with the perovskite crystal structure. $CsPbCl_3$ adopts the orthorhombic $GdFeO_3$-type structure at room temperature [30], undergoing a transition to the cubic phase at 37-47°C. The distortion of the room-temperature structure is small and gives rise to tiny additional reflections that are not visible on the scale of Figure 2.1c. As reported previously [16, 17, 19-21, 29], Yb^{3+}-doping does not cause significant shifts of the XRD reflections relative to undoped $CsPbCl_3$ (Figure 2.1c).

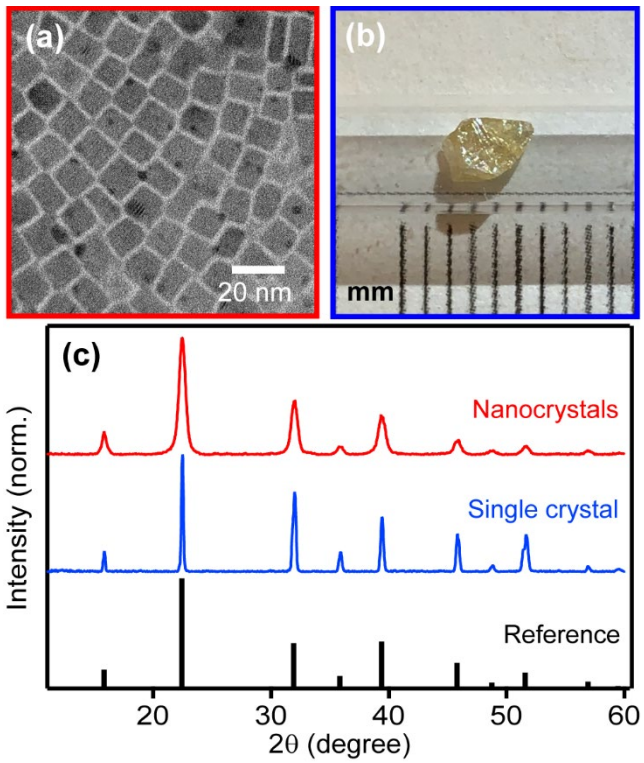

Figure 2.1. (a) TEM image of 4.3% Yb^{3+}:$CsPbCl_3$ NCs and **(b)** a photograph of a 2% Yb^{3+}:$CsPbCl_3$ SC. Tick marks indicate mm spacings. **(c)** Powder XRD data collected for the same Yb^{3+}:$CsPbCl_3$ NCs (red) and SC (blue). Reference indices (black) are shown for the cubic high-temperature form of $CsPbCl_3$ (PDF 73-692), which is stable in bulk above ~37-47 °C [31]. Bulk $CsPbCl_3$ adopts the orthorhombic $GdFeO_3$-type structure (space group Pnma) at room temperature [30], giving rise to additional small reflections that are not visible on the scale of panel (c).

2.4.2 *Photoluminescence spectra*

Figure 2.2 shows steady-state PL spectra of 1.7% Yb^{3+}:$CsPbCl_3$ NCs and the 2% Yb^{3+}:$CsPbCl_3$ SC of Figure 2.1 measured at several temperatures from 5 to 295 K. The 5 K PL spectra of both samples (Figure 2.2a) are highly structured, showing features characteristic of Yb^{3+} $^2F_{5/2} \rightarrow {}^2F_{7/2}$ transitions in related chloride lattices. Notably, almost all of the peaks from the NC sample are directly correlated with peaks at the same energies and with the same relative intensities in the SC sample. The similarities between these spectra indicate similar environments for the perovskite-sensitized Yb^{3+} ions in the two forms of the material. This observation is important because of the extremely large surface-to-volume ratios of the NCs compared to the bulk SC, and it demonstrates that the active Yb^{3+} ions in the NCs are indeed bulk-like rather than, *e.g.*, bound to the NC surfaces.

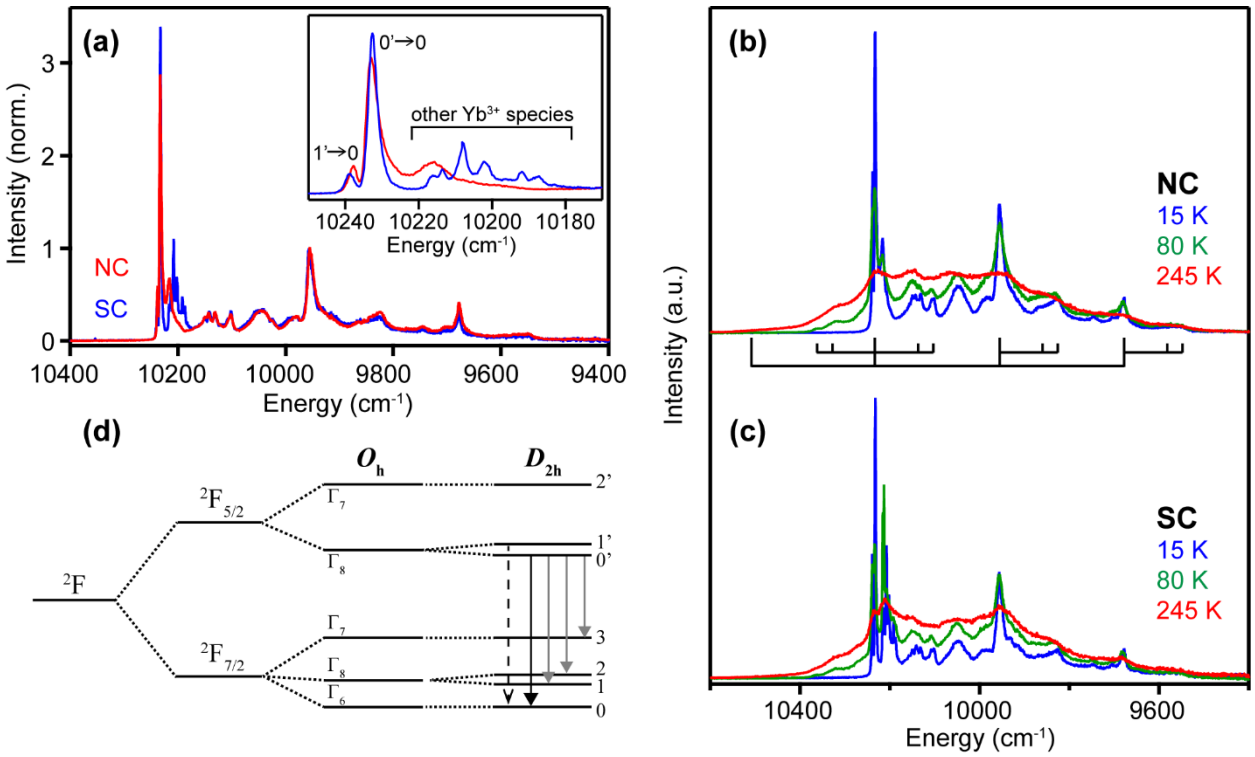

Figure 2.2. (a) 5 K PL spectra of Yb^{3+}:$CsPbCl_3$ NCs (red, [Yb^{3+}] = 1.7%) and the SC sample from Figure 2.1 (blue, [Yb^{3+}] = 2%), normalized to the peak at ~9960 cm^{-1}. *Inset*: The first set of peaks at highest energies in both samples at 5 K, showing the dominant 0'→0 and 1'→0 (hot-band) crystal-field components of the Yb^{3+} $^2F_{5/2} \rightarrow {}^2F_{7/2}$ transition as well as a series of smaller peaks from other Yb^{3+} species. Variable temperature PL spectra of **(b)** the NCs and **(c)** the SC from panel (a) measured at 15 K (blue), 80 K (green), and 245 K (red). λ_{ex} = 375 nm for all panels. The spectrum in (b) includes markers denoting the periodic structure attributed to vibronic coupling, both on the Stokes and anti-Stokes (hot-band) sides of the first intense maximum. **(d)** Schematic illustration of Yb^{3+} *f-f* energy levels, including the low-symmetry splitting of Γ_8 components. The idealized reduced site symmetry is labeled as D_{2h}. The solid and dashed black arrows show the $^2F_{5/2} \rightarrow {}^2F_{7/2}$ 0'→0 and 1'→0 crystal-field transitions labeled in panel (a), respectively. The gray arrows indicate other low-temperature crystal-field origins that have not been conclusively identified in the spectrum.

Both PL spectra in Figure 2.2a show their maximum peak intensities in a sharp feature at 10233 cm^{-1}, interpreted as an electronic origin within the crystal-field-split Yb^{3+} $^2F_{5/2} \rightarrow {}^2F_{7/2}$ spectrum. In the cubic limit, the $^2F_{7/2}$ ground term is split by the crystal field into Γ_6, Γ_8, and Γ_7 levels, in order of increasing energy, and the $^2F_{5/2}$ excited term is split into Γ_8 and Γ_7 levels, such that this highest-energy origin at low temperature is associated with the $\Gamma_8(^2F_{5/2}) \rightarrow \Gamma_6(^2F_{7/2})$ transition (*vide infra*). To lower energy, the next most prominent peak occurs at 9957 cm^{-1}, shifted ~276 cm^{-}

[1] from the first peak, and a third distinct peak is found another ~276 cm^{-1} to lower energy with lower intensity. Each of these peaks appears to additionally show similar side bands at ~93 and 130 cm^{-1}. Such regularity in the spectral pattern suggests that this emission gains electric-dipole allowedness by the vibronic mechanism, despite high shielding of the *f* orbitals involved in these transitions [32, 33], and hence that the quantum-cutting Yb^{3+} ions reside at sites that lack a large odd-parity crystal-field component. In this mechanism, electric-dipole allowedness is enhanced by coupling the pure electronic transition with one quantum of an odd-parity local vibrational mode of the $[YbCl_6]^{3-}$ moiety. In support of this interpretation, we note that the energies here are very similar to those of the vibronic sidebands observed in the luminescence of Yb^{3+}-doped $Cs_2NaHoCl_6$ (86 cm^{-1} (ν_6), 108 cm^{-1} (ν_4), and 257 cm^{-1} (ν_3), all ungerade local modes) [34]. An additional broad luminescence peak is observed at ~10048 cm^{-1} whose assignment is unclear. This feature occurs close in energy to the $\Gamma_8(^2F_{5/2}) \rightarrow \Gamma_8(^2F_{7/2})$ origin in cubic Yb^{3+}-doped $Cs_2NaHoCl_6$ [34] and could result from this electronic transition in somewhat reduced symmetry, for example due to a proximal charge-compensating defect. Alternatively, the $\Gamma_8(^2F_{5/2}) \rightarrow \Gamma_8(^2F_{7/2})$ origin may instead coincide with the intense peak at 9957 cm^{-1} in Figure 2.2a, akin to the spectra of Yb^{3+} in cubic fluoroperovskites [35]. Further studies on the SC sample and on halide-alloyed samples will be aimed at clarifying these assignments.

Both the NC and SC samples show an additional weak PL peak at 10239 cm^{-1}, *i.e.*, ~6 cm^{-1} to *higher* energy of the 10233 cm^{-1} $\Gamma_8(^2F_{5/2}) \rightarrow \Gamma_6(^2F_{7/2})$ origin. This feature is attributed to a thermal hot band reflecting a low-symmetry splitting of the emissive $\Gamma_8(^2F_{5/2})$ level into 0' and 1' crystal-field components. In support of this interpretation, we note that elevating the temperature from 5 to 15 K increases the intensity of this higher-energy band by nearly a factor of 3. Fitting this temperature dependence in relation to that of the 10233 cm^{-1} intensity using a simple two-level Boltzmann model (see Section 2.8 Appendix) yields an energy splitting that agrees well with the spectroscopic splitting and supports the peak assignment. Nearly identical results are obtained for the SC sample. This $\Gamma_8(^2F_{5/2})$ splitting energy is small compared to those of Yb^{3+} ions in many other pseudo-octahedral crystalline sites (*e.g.*, ~45 cm^{-1} in hexagonal $CsMnCl_3$ [36] and ~16 cm^{-1} in hexagonal $CsCdBr_3$ [37, 38]), from which it is inferred that the Yb^{3+} ions involved in quantum cutting have a site symmetry that is close to octahedral.

In addition to populating the $\Gamma_8(^2F_{5/2})$ hot band, raising the sample temperature also broadens

all of the individual PL features observed at 5 K and introduces additional hot bands at higher energies. These hot bands occur with the same energies identified in the low-temperature spectrum, supporting the assignment of these features as vibronic. For example, the 80 K spectrum of the NCs (Figure 2.2b) shows clear hot bands ~93 and 130 cm^{-1} to higher energy of the 10233 cm^{-1} low-temperature origin, and the 245 K spectrum shows an additional broad shoulder that would be consistent with a ~276 cm^{-1} hot band (see Section 2.8 Appendix), although the spectral breadth at this temperature impedes a concrete assignment. Moreover, the Yb^{3+} PL decay times decrease substantially with increasing temperature (*vide infra*) while the integrated PL intensities increase (Figures 2.2b, c), consistent with a vibronic electric-dipole intensity-gaining mechanism and hence Yb^{3+} centrosymmetry. Concomitantly, the excitonic PL intensity of the NCs decreases with increasing temperature (see Section 2.8 Appendix), as we reported previously for other NC samples [16].

EPR measurements of Mn^{2+}-doped $CsPbCl_3$ SCs have indicated essentially orthorhombic B-site point symmetries of D_2, C_{2v}, or D_{2h} at all temperatures below the cubic phase transition (~320 K) [39], of which only D_{2h} has the inversion symmetry implied by the PL spectra and variable-temperature PL data described above. Similarly, EPR measurements of Gd^{3+}-doped $CsPbCl_3$ SCs have also suggested a centrosymmetric point group at room temperature, assigned as C_{2h} [40]. In both cases, reduction from orthorhombic to monoclinic and possibly lower site symmetries are formally required in lower-temperature phases, but these distortions appear to be minor [39, 40]. With these considerations and the spectroscopic observations described above, we assume an effective site symmetry of either D_{2h} or C_{2h} for Yb^{3+} in $CsPbCl_3$ at all temperatures examined here. Figure 2.2d summarizes the Yb^{3+} crystal-field splittings so far deduced for this system, assuming an idealized site symmetry of D_{2h}.

The main difference between the NC and SC spectra is in the set of peaks within the first ~50 cm^{-1} of the first intense maximum, *e.g.*, at ca. 10230 cm^{-1} (Figure 2.1a, inset). Here, the NCs appear to show a simpler spectrum, with only one clear side peak at 10216 cm^{-1}, whereas the SC shows a multitude of maxima in this region. Site-selective photoexcitation measurements on the SC sample demonstrate that these various sharp features come from different Yb^{3+} species, and at least 5 distinct species can be deduced (see Section 2.8 Appendix). Because the charge of the Yb^{3+} dopants is different from that of the B-site Pb^{2+} cations, additional defect formation is always required to achieve charge neutrality, and the additional PL lines are thus attributed to Yb^{3+} "trap"

sites with different charge-compensation motifs. These Yb^{3+} trap species are only resolved near the first electronic origin, where spectral broadening is smallest. In support of the interpretation of these peaks as due to other Yb^{3+} species, we note that some of their intensities increase markedly with increasing temperature in the SC spectra but not in the NC spectra (Figure 2.2). This observation is consistent with thermally assisted energy migration and capture by Yb^{3+} traps in the SC sample, as also reflected in the increasingly multi-exponential Yb^{3+} decay (*vide infra*) and in the low PLQY (~20%) of the SC sample. Although numerous, these Yb^{3+} traps account for < ~30% of the integrated quantum-cutting PL at low temperature (see Section 2.8 Appendix). The fact that the majority of quantum-cutting PL intensity arises from just the 10230 cm^{-1} species even though that species is not dominant in any of the PL spectra obtained with direct Yb^{3+} photoexcitation strongly suggests that quantum cutting occurs non-statistically, *i.e.*, the 10230 cm^{-1} Yb^{3+} species is disproportionately active in quantum cutting. Notably, the 10230 cm^{-1} quantum-cutting species also shows by far the most intense vibronic structure among the species observed by site-selective excitation (see Section 2.8 Appendix). Overall, we conclude that quantum cutting is dominated by the same specific Yb^{3+} species in both NC and SC forms of this material.

2.4.3 *Photoluminescence dynamics*

Figure 2.3 plots room-temperature NIR PL decay curves measured for the Yb^{3+}:$CsPbCl_3$ NCs ([Yb^{3+}] = 1.7%) and SC ([Yb^{3+}] = 2%) of Figure 2.2. The NCs (Figure 2.3a) show nearly monoexponential PL decay following $CsPbCl_3$ photoexcitation, with τ_{decay} ~ 1.5 ms. The inset to Figure 2.3a reveals a distinct rise in the Yb^{3+} PL following the excitation pulse, having a time constant of ~8 ns. Similar data are found for the Yb^{3+}:$CsPbCl_3$ SC (Figure 2.3b), except that the Yb^{3+} PL decay in this sample is multiexponential. Measurement at short times again reveals a ~7 ns rise time for Yb^{3+} PL following $CsPbCl_3$ photoexcitation.

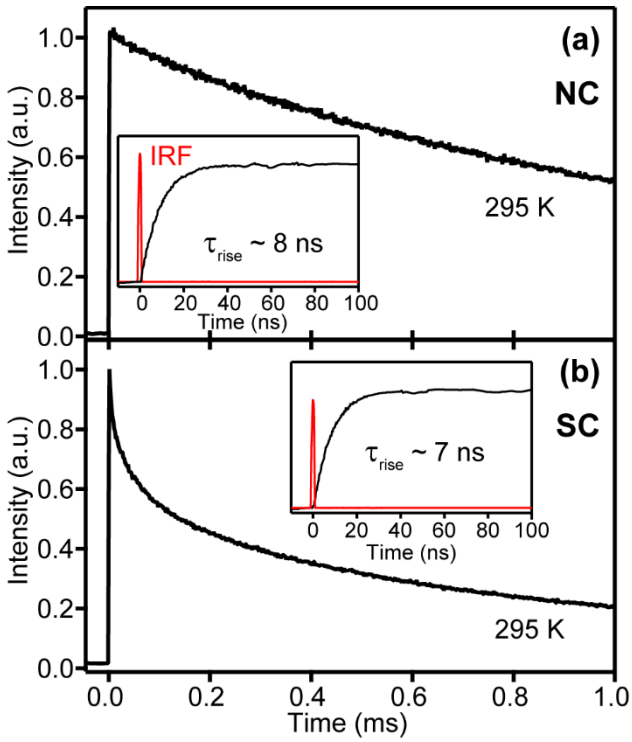

Figure 2.3. Representative room-temperature TRPL data collected for **(a)** NCs ([Yb^{3+}] = 1.7%) and **(b)** a SC ([Yb^{3+}] = 2% (nom.)) of Yb^{3+}:$CsPbCl_3$. *Inset*: First 100 ns of the room-temperature TRPL trace, showing a distinct rise at short times. The red curve plots the experimental instrument response function (IRF). λ_{ex} = 404 nm, λ_{em} = 985 nm.

Figure 2.4 plots TRPL data measured for the Yb^{3+}:$CsPbCl_3$ NCs and SC from Figure 2.2 at temperatures from 5 to 295 K following interband photoexcitation of the $CsPbCl_3$. Figure 2.4a plots the Yb^{3+} PL intensities at short times on a linear intensity scale, and Figure 2.4b plots the same PL decay over much longer times and on a logarithmic intensity scale. The NC PL decay curves in Figure 2.4b are all nearly monoexponential and the decay rate accelerates by roughly a factor of 2 upon warming from 5 to 295 K, even though the integrated PL intensity increases over this temperature range. This temperature dependence is consistent with the conclusion drawn above that the Yb^{3+} excited *via* quantum cutting occupies a centrosymmetric lattice site and that thermal energy accelerates the *radiative* Yb^{3+} $^2F_{5/2} \rightarrow {}^2F_{7/2}$ transition through vibronic coupling. Figure 2.4a shows that the rise of the NC Yb^{3+} PL gets much slower as the temperature is lowered. Whereas the PL rise at room temperature is too fast to be observed in the window of Figure 2.4a (but see Figure 2.3a, inset, and Section 2.8 Appendix), the PL rise at 5 K is biexponential with its dominant (~80%) component having a time constant of ~40 ns (*vide infra*) followed by a much

slower component (~20%) with a time constant of ~50 μs.

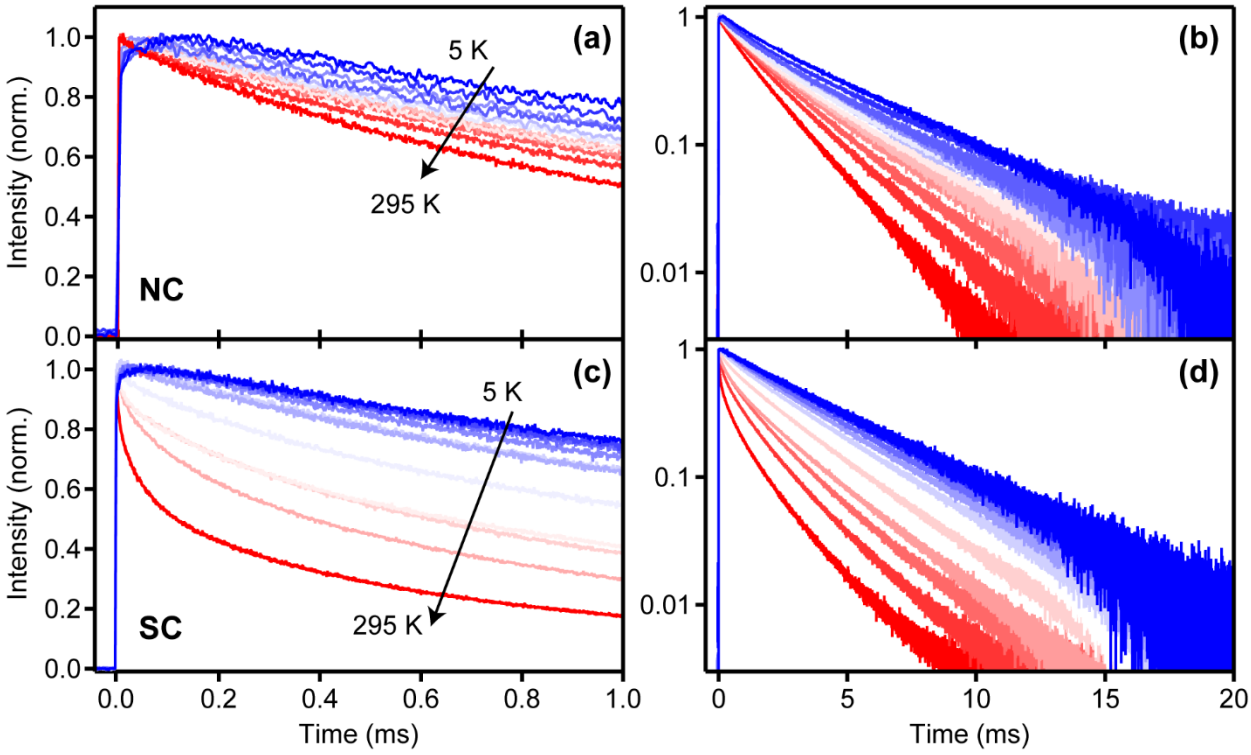

Figure 2.4. Variable-temperature TRPL traces measured for **(a)**, **(b)** NCs and **(c)**, **(d)** a SC of Yb^{3+}:$CsPbCl_3$ (1.7% and 2%(nom.) Yb^{3+}, respectively), from 5 K (blue) to room-temperature (red). Temperatures: 5, 15, 30, 45, 60, 80, 100, 125, 150, 200, 250, 295 K. λ_{ex} = 404 nm, λ_{em} = 982 nm (at 5-150 K), 985 nm (at 200-295 K).

Figures 2.4c and d plot analogous data collected for the Yb^{3+}:$CsPbCl_3$ SC. Similar trends are observed, with slower Yb^{3+} PL rise and decay dynamics at lower temperatures. The SC data are complicated by additional processes that make the Yb^{3+} PL decay curves multiexponential, most evident in the appearance of a prominent PL decay component with a time constant of ~100 μs at room temperature that is absent at lower temperatures. Despite these specific differences, the SC TRPL data (Figures 2.4c, d) are generally very similar to those measured for the NCs (Figures 2.4a, b).

Figure 2.5 summarizes the data from Figures 2.2 and 2.4 for both the Yb^{3+}:$CsPbCl_3$ NCs (Figures 2.5a-c) and the Yb^{3+}:$CsPbCl_3$ SC (Figures 2.5d-f). Figure 2.5a plots the temperature dependence of the integrated steady-state Yb^{3+} PL intensity, along with the temperature dependence of the PL decay time, τ_{decay}, obtained by fitting the data to a single-exponential

function. Figure 2.5d plots analogous variable-temperature data for the Yb^{3+}:$CsPbCl_3$ SC. Here, the figure plots the amplitude-weighted average decay time, $\tau_{decay}(avg)$ (eq 2.2), where *n* indexes the decay components), obtained from biexponential fits of the PL decay curves (see Section 2.8 Appendix);

$$\tau_{decay}(avg) = \frac{\sum A_n \tau_n^2}{\sum A_n \tau_n}. \tag{2.2}$$

Figures 2.5a and d both show the same trend of increasing Yb^{3+} PL intensity with increasing temperature, more than doubling over this temperature range. In parallel, the Yb^{3+} PL decay time decreases from over ~4 ms at 5 K to ~1.5 ms at 295 K for both samples. These trends are similar to the NC results reported previously [16]. The PL temperature dependence described by Figures 2.5a and d also suggests that PL saturation, which is directly linked to the long Yb^{3+} excited-state lifetime [29], may be partially alleviated in solar cells, which operate at about 80 °C (~350 K).

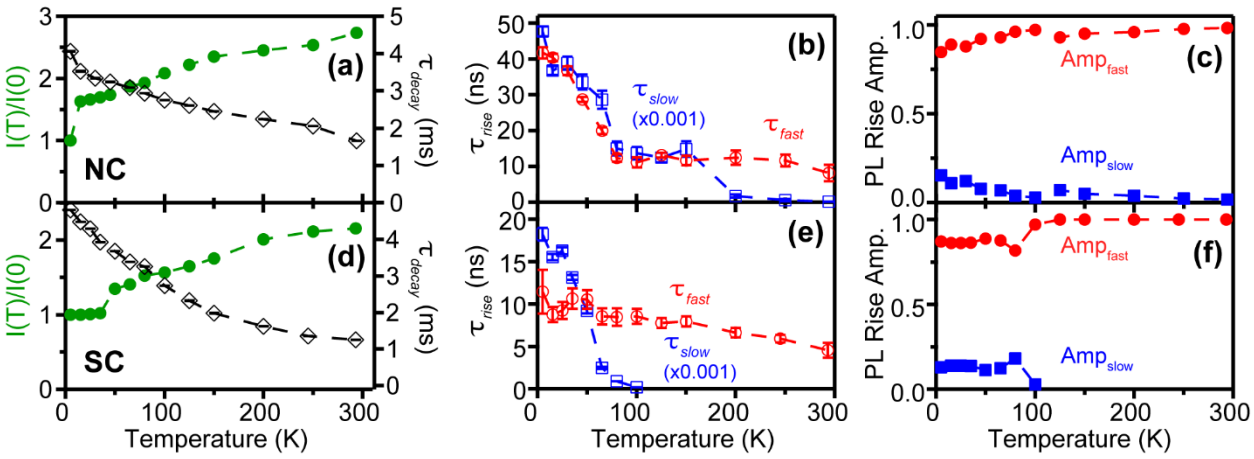

Figure 2.5. Scatter plots summarizing the variable-temperature PL data in Figures 2.2 and 2.4. Integrated NIR PL intensities (green) and decay times (black) for the Yb^{3+}:$CsPbCl_3$ NCs **(a)** and SC **(d)** plotted *vs* temperature. For the SC, τ_{decay} reflects the average PL decay time obtained from biexponential fitting, as described by eq 2.2. Fast (red) and slow (blue) NIR PL rise times and amplitudes measured for the Yb^{3+}:$CsPbCl_3$ NCs **(b)**, **(c)** and SC **(e)**, **(f)**, plotted *vs* temperature.

Table 2.1. Key results from analysis of Yb^{3+} photoluminescence rise and decay dynamics at 5 K and 295 K following pulsed photoexcitation of the $CsPbCl_3$ host in ~2% Yb^{3+}:$CsPbCl_3$ nanocrystal and single-crystal samples (Figures 2.4 and 2.5).

	Nanocrystals		Single Crystal	
	5 K	295 K	5 K	295 K
Decay: τ_{decay}	4.1 ms	1.7 ms	4.4 ms	1.3 ms
Rise: τ_{fast} (% amplitude)	41.6 ns (81%)	7.9 ns (98%)	11.8 ns (87%)	7.0 ns (100%)
Rise: τ_{slow} (% amplitude)	47.7 μs (19%)	100 ns (2%)	18.2 μs (13%)	--

The bi-exponential Yb^{3+} PL rise data for the Yb^{3+}:$CsPbCl_3$ NCs (Figure 2.4a) were fitted and the time constants and amplitudes of each component are plotted separately in Figures 2.5b and c. At 5 K, ~80% of the NC PL rise occurs with a time constant of τ_{fast} ~ 42 ns, and the remaining 20% has a rise time of τ_{slow} ~ 48 μs. Both rise components accelerate (Figure 2.5b) and the fast component dominates more (Figure 2.5c) with increasing temperature. The amplitude of the slow rise decreases from ~20% at 5 K to close to 0% at 100 K, and only a fast rise component of τ_{fast} ~ 8 ns is discernable at 295 K. Very similar results are again found for the SC (Figures 2.5e, f). Here, at 5 K, the fast rise component has a fractional amplitude of ~87% and a time constant of only ~12 ns, whereas the slow component (~13%) is characterized by τ_{slow} ~ 18 μs. By room temperature, the slow rise is no longer discernable and the fast rise has accelerated to τ_{fast} ~ 7 ns (Figure 2.3b, inset). Energy transfer to Yb^{3+} following semiconductor photoexcitation is thus very fast at room temperature in both the NC and SC Yb^{3+}:$CsPbCl_3$ samples.

2.5 **Discussion**

2.5.1 *Comparison of NCs and SC*

A primary observation from the results and analysis presented above is that the NCs and SC are essentially identical to one another, despite their massively different surface-to-volume ratios and the very different reaction conditions under which these two forms of Yb^{3+}:$CsPbCl_3$ were prepared (solution precipitation *vs* Bridgman growth). Structurally, the powder XRD data for these two forms are basically indistinguishable. Even more diagnostic are the high-resolution low-

temperature PL data; both samples show remarkably similar sensitized Yb^{3+} PL peak energies and intensities, indicating that the Yb^{3+} species active in quantum cutting in both forms are the same. Surprisingly, even the dynamics of energy transfer to Yb^{3+} following $CsPbCl_3$ photoexcitation are essentially identical in the NCs and SC. Both forms show an Yb^{3+} PL rise time constant of about 7 ns at room temperature. These observations highlight the conclusion that quantum cutting in the Yb^{3+}-doped $CsPbCl_3$ composition does not require any other properties of NCs or the other granular forms that have been explored previously [17, 21], such as surfaces, grain-boundary defects, or spatial exciton confinement.

Despite these overwhelming similarities, some differences are still observed between the NCs and SC, and these differences can be informative. In high-resolution PL spectra, for example, the two samples show different distributions of Yb^{3+} traps. These traps reflect a variety of charge-compensation motifs generated upon substitutional doping of Yb^{3+} in both the NCs and the SC, but with different distributions of these traps between the two forms. Such a difference is not surprising given the very different synthesis conditions used for preparing the two materials. The SC sample shows evidence of thermally assisted energy migration and capture by these traps, which is manifested in their different PL temperature dependence, the temperature dependence of the Yb^{3+} quantum-cutting PL decay dynamics, and ultimately the relatively low PLQY of the SC sample (~20%). Additionally, the NCs show excitonic PL at low temperatures that disappears when the temperature is raised, but the SC sample shows no excitonic PL at any temperature (see Section 2.8 Appendix). This result suggests that nonproductive exciton recombination is more competitive in the SC sample than in the NCs, and it is also consistent with the low PLQY of the SC sample (~20%). Notably, the similar Yb^{3+} PL rise times for these two samples suggest that these losses occur *prior* to energy capture by the intermediate defect state. Despite these specific differences between Yb^{3+}-doped $CsPbCl_3$ NCs and SC, the primary photophysical characteristics of these two forms of the material are almost identical.

2.5.2 *Quantum-cutting energy-transfer dynamics*

Previously, we demonstrated that Yb^{3+} doping of $CsPbCl_3$ NCs and solution-deposited granular thin films [16, 17] introduces a new few-picosecond exciton depopulation channel attributed to quantum cutting. An intermediate state associated with a hypothesized dopant-induced defect was proposed to mediate energy transfer from the perovskite to Yb^{3+} [16]. The observation here of a ~7

ns rise at room temperature in the Yb^{3+} PL following pulsed interband photoexcitation, and the fact that this rise is slower than the exciton depopulation time, provides the first direct evidence that energy transfer from the perovskite to Yb^{3+} indeed proceeds *via* such an intermediate state, supporting the general energy-transfer mechanism proposed previously [16]. Although the PL data presented above also reveal other Yb^{3+} species in both NC and SC samples, presumably associated with different charge-compensation motifs, the data point to just one specific species as dominant in quantum cutting.

A slower (μs) pathway for Yb^{3+} sensitization is also observed in the PL rise dynamics at low temperatures, but the PL is almost entirely dominated by the fast (ns) pathway in both the NCs and the SC, and so we focus our discussion on this process. An interesting fundamental question pertains to the electronic-structure origins of the fast energy-transfer rate. In most other quantum-cutting systems, the actual quantum-cutting energy-transfer step involves weak multipolar coupling between formally electric-dipole-forbidden *f—f* transitions of the energy donor (*e.g.*, Pr^{3+} [9, 11], Tb^{3+} [8], Er^{3+} [12], Tm^{3+} [10], Nd^{3+} [13], Ho^{3+} [14]) and the quantum-cutting acceptor (typically Yb^{3+}). Consequently, quantum-cutting time constants ranging from ~6 μs – 4 ms are typically observed. More similar to the present system are the energy-transfer times observed in molecularly sensitized (non-quantum-cutting) Ln^{3+} compounds, which typically show energy transfer from ligand singlet states to bound Ln^{3+} ions on the timescale of 100s of ps to several ns [41]. This rapid energy transfer involves a Dexter-type exchange mechanism instead of the multipolar coupling mechanism active in typical lanthanide pairs. The absence of near-band-edge emission at room temperature (see Section 2.8 Appendix) is an indication that the oscillator strength of the intermediate state is too small for its radiative recombination to compete with energy transfer to Yb^{3+}, consistent with a Dexter-type energy transfer mechanism. We thus propose that energy transfer in Yb^{3+}-doped $CsPbCl_3$ proceeds *via* an exchange-mediated mechanism that involves coupling between the dopant-induced defect and two Yb^{3+} ions. Because Dexter-type energy transfer is a short-range effect, the dopant-induced defect must be close to both Yb^{3+} acceptor ions, and it may in fact be this defect that differentiates the PL spectrum of the Yb^{3+} sites involved in quantum cutting from the spectra of the other Yb^{3+} sites in the crystal (Figure 2.2a). Overall, these findings are generally consistent with the proposal [16] of a Yb^{3+}-V_{Pb}-Yb^{3+} charge-neutral defect cluster at the heart of quantum cutting, although the precise microscopic defect structure remains unknown.

Scheme 2.1. Quantum-cutting energy transfer in Yb^{3+}-doped $CsPbCl_3$. Photoexcitation of $CsPbCl_3$ (black up arrow) is followed by intense Yb^{3+} *f—f* luminescence (red down arrows) after quantum cutting. The majority of the quantum cutting proceeds following the blue arrows, *via* energy capture by a dopant-induced defect (k_{defect}) and then simultaneous energy transfer to two Yb^{3+} dopants (k_{QC}). This process takes < 10 ns at room temperature and < 50 ns at liquid-helium temperatures. A minority slow pathway is also observed at low temperatures that is proposed to involve temporary trapping and detrapping by native defects (green arrows). This process takes ~20 to 50 μs at liquid-helium temperatures. Solid arrows indicate radiative processes and dashed arrows indicate nonradiative processes.

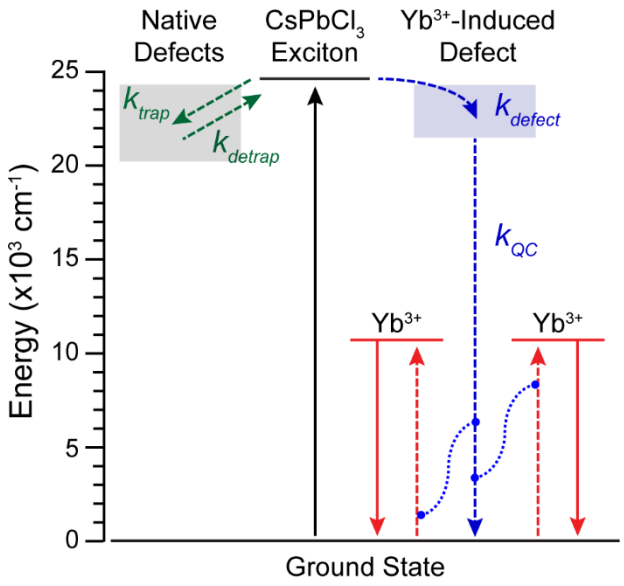

Scheme 2.1 summarizes the energy flow upon perovskite photoexcitation. Efficient quantum cutting involves two consecutive energy-transfer steps: the first from the exciton to a shallow dopant-induced defect (k_{defect}), and the second from that defect state to a pair of Yb^{3+} ions (k_{QC}). The dopant-induced defect state depopulates the excitonic state on a single-picosecond timescale and can compete with all other radiative and nonradiative processes affecting the exciton population [16, 17]. The quantum-cutting step (k_{QC}) is also very rapid, with $1/k_{QC} \sim 7$ ns at room temperature. Both the NCs and SC show increasing integrated Yb^{3+} PL intensities upon increasing the temperature from 5 to 295 K, despite more non-radiative decay of the Yb^{3+} excited state (k_{decay}) at elevated temperatures in the SC. This observation indicates that the branching ratios for one or both of the two upstream quantum-cutting energy-transfer steps (k_{defect} and k_{QC}) must become more favorable with increasing temperature. This conclusion is supported by the observation of decreasing excitonic PL intensity with increasing temperature in the NCs.

Such an energy-transfer process can be considered in the framework of Fermi's golden rule, eq 2.3, which describes k_{QC} as a function of the donor/acceptor electronic coupling (M_{DA}) and spectral overlap (ρ):

$$k_{QC} = \frac{2\pi}{\hbar} |M_{DA}|^2 \rho. \quad (2.3)$$

In Yb^{3+}-doped $CsPbCl_3$, $k_{QC} = 1/\tau_{rise}$ (the fast rise component), the donor in the quantum-cutting step is the dopant-induced defect state, and the acceptor is a pair of Yb^{3+} ions that are both coupled to this defect state, and hence in proximity to the defect. For simplicity, we consider this Yb^{3+} pair as formally a single "dimeric" acceptor with states at $2\times E_{f\text{-}f}$, although a three-center formalism may be more appropriate for quantitative description.

We have previously explored the role of ρ in Yb^{3+}:$CsPb(Cl_{1-x}Br_x)_3$ quantum cutting experimentally, using anion exchange to tune the donor energy [19]. Because the dopant-induced defect state is shallow, $E_{donor} \sim E_g$. For $E_g > 2\times E_{f\text{-}f}$, the NIR PLQY is roughly independent of E_g. Given the narrowness of the *f*—*f* absorption, ρ must be small at large values of E_g and quantum cutting must be phonon assisted, but k_{QC} must nonetheless remain sufficiently large to maintain efficient quantum cutting. A steep drop in the NIR PLQY is observed when $E_g < \sim 2\times E_{f\text{-}f}$, attributed to reduction of ρ to zero, *i.e.*, a quantum-cutting threshold energy [17, 19].

The electronic-coupling term (M_{DA}) in this system is of high fundamental interest, but it is as yet poorly understood. From the above discussion of energy-transfer rates in other systems, quantum cutting in Yb^{3+}:$CsPbX_3$ proceeds *via* a Dexter-type exchange mechanism. In this scenario, the electronic coupling between the partially localized dopant-induced defect state and Yb^{3+} acceptors is likely mediated by Yb^{3+}-X^- covalency. Computational work [28] has suggested that a proximal Pb^{2+} ion of a right-angle Yb^{3+}-V_{Pb}-Yb^{3+} defect cluster possesses increased electron density that could play an important role in facilitating this quantum-cutting step. In the construct of second-order perturbation theory, Yb^{3+}-X^- covalency reflects configuration interaction between the Yb^{3+}(4*f*) states and low-lying halide-to-Yb^{3+} charge-transfer (LMCT) excited states, which formally involve photoinduced electron transfer from the valence band to Yb^{3+}. Other recent experimental work has led to the proposal that this quantum cutting involves electron trapping by Yb^{3+} to form a discrete Yb^{2+} intermediate [25]. The position of the $Yb^{3+/2+}$ level relative to the perovskite band edges is not known. The NIR PL spectra in Figure 2.2 are consistent with Yb^{3+} coordinated by 6 Cl^- anions in a pseudo-octahedral $[YbCl_6]^{3-}$ cluster, and the first LMCT excited

states of comparable $[YbCl_6]^{3-}$ centers are not observed until ~36000 cm^{-1} (compared with E_g ~ 26000 cm^{-1} for $CsPbCl_3$) [42, 43]. These LMCT transitions shift down to ~29000 cm^{-1} in $[YbBr_6]^{3-}$ (compared with E_g ~ 19000 cm^{-1} for $CsPbBr_3$) [44, 45], but remain >1 eV higher in energy than the perovskite energy gap. This consideration, in conjunction with the experimental observation of new near-band-edge defect emission upon doping $CsPbCl_3$ with redox-inactive La^{3+}, points to a more general dopant-induced defect state rather than Yb^{2+} as the quantum-cutting intermediate. Further combined experimental and theoretical advances will be required to fully understand the electronic structure of this unique material.

Finally, we address the origins of the slow component observed in the Yb^{3+} PL rise dynamics. The observation of a biexponential PL rise demonstrates the existence of two separate pathways for energy transfer from the perovskite to Yb^{3+}. Although the slow rise only accounts for <~20% of the Yb^{3+} PL at 5 K and is not observable at room temperature, it suggests the presence of a competing process that intercepts and temporarily stores the photoexcitation energy in a separate metastable state before eventually transferring it to Yb^{3+}. Metastable charge-separated states have previously been postulated for undoped $CsPbX_3$ ($X = Cl^-$, Br^-) NCs and thin films, formed by hole trapping on the timescale of tens of picoseconds [46-48], and substantial delayed luminescence involving a metastable charge-separated state has also been reported for both SC and NC forms of the related hybrid perovskite, $CH_3NH_3PbBr_3$ [49, 50]. We hypothesize that the slow quantum-cutting process observed here reflects rapid but reversible trapping in a similar metastable charge-separated state, as also illustrated in Scheme 2.1 (k_{trap} and k_{detrap}). Thermal detrapping from this metastable state accelerates this slow quantum-cutting pathway at elevated temperatures, and by room temperature it is no longer distinguishable. We note that the precise microscopic steps in this slow pathway remain unclear; the pathway may involve equilibrium between excitonic and metastable excited states alone, as in delayed excitonic luminescence and depicted in Scheme 2.1, or it could conceivably involve energy transfer to Yb^{3+} directly from the metastable state.

2.6 **Conclusion**

Despite their very different synthetic origins and surface-to-volume ratios, Yb^{3+}:$CsPbCl_3$ NC and SC samples show remarkably similar spectral and photophysical characteristics. The structural and spectroscopic data reported here are consistent with substitutional Yb^{3+}-doping at the lattice B-site of perovskite $CsPbCl_3$. This aliovalent substitution requires additional defect formation to maintain

charge neutrality, and several distinct Yb^{3+} species are observed spectroscopically. Quantum cutting in both crystal forms is largely dominated by the same specific Yb^{3+} species, however. This species appears to be close to centrosymmetric with nearly octahedral site symmetry and it appears to display relatively strong vibronic coupling in its *f-f* luminescence.

TRPL measurements have provided the first direct evidence of an intermediate state in the energy transfer from $CsPbCl_3$ to Yb^{3+}. In both NC and SC samples, a fast rise time of about 7 ns is observed in the room-temperature Yb^{3+} PL following perovskite photoexcitation. This observation solidifies the prior hypothesis [16] that quantum cutting involves consecutive steps of (*i*) energy capture by a dopant-induced defect, followed by (*ii*) energy transfer from this defect to two Yb^{3+} ions. The first step depopulates the photogenerated perovskite excited state within a few picoseconds, localizing the excitation in proximity to the Yb^{3+} dopants, and the second step captures the excitation energy at Yb^{3+} within a few nanoseconds. The nanosecond Yb^{3+} PL rise time suggests that energy transfer from the intermediate dopant-induced defect state to Yb^{3+} is mediated by exchange. Both energy-transfer steps accelerate with increasing temperature, becoming more competitive with other non-productive trapping or recombination processes. The rapid energy localization and capture described here are responsible for the high efficiency of quantum cutting in this material, making it kinetically competitive with all other processes following photoexcitation. An additional slower rise component (μs) of the Yb^{3+} PL is observed at low temperatures, attributed to a second sensitization pathway that involves temporary storage of excitation energy in a native metastable trap state, similar to the scenario responsible for delayed excitonic luminescence. The results presented here provide new insights into the fundamental spectroscopic and photophysical properties of Yb^{3+}:$CsPbX_3$ quantum cutters that will help the development of this material for future solar and photonic applications.

2.7 References

1. Shockley, W.; Queisser, H. J. Detailed Balance Limit of Efficiency of *p-n* Junction Solar Cells. *J. Appl. Phys.* **1961,** *32*, 510-519.
2. Trupke, T.; Green, M. A.; Würfel, P. Improving Solar Cell Efficiencies by Down-Conversion of High-Energy Photons. *J. Appl. Phys.* **2002,** *92*, 1668-1674.
3. Geacintov, N.; Pope, M.; Vogel, F. Effect of Magnetic Field on the Fluorescence of Tetracene Crystals: Exciton Fission. *Phys. Rev. Lett.* **1969,** *22*, 593-596.
4. Dexter, D. L. Two Ideas on Energy Transfer Phenomena: Ion-Pair Effects Involving the OH Stretching Mode, and Sensitization of Photovoltaic Cells. *J. Lumin.* **1979,** *18-19*, 779-784.

5. Hanna, M. C.; Nozik, A. J. Solar Conversion Efficiency of Photovoltaic and Photoelectrolysis Cells with Carrier Multiplication Absorbers. *J. Appl. Phys.* **2006,** *100*, 074510.
6. Schaller, R. D.; Klimov, V. I. High Efficiency Carrier Multiplication in PbSe Nanocrystals: Implications for Solar Energy Conversion. *Phys. Rev. Lett.* **2004,** *92*, 186601.
7. Nozik, A. J.; Beard, M. C.; Luther, J. M.; Law, M.; Ellingson, R. J.; Johnson, J. C. Semiconductor Quantum Dots and Quantum Dot Arrays and Applications of Multiple Exciton Generation to Third-Generation Photovoltaic Solar Cells. *Chem. Rev.* **2010,** *110*, 6873-6890.
8. Vergeer, P.; Vlugt, T. J. H.; Kox, M. H. F.; den Hertog, M. I.; van der Eerden, J. P. J. M.; Meijerink, A. Quantum Cutting by Cooperative Energy Transfer in $Yb_xY_{1-x}PO_4:Tb^{3+}$. *Phys. Rev. B* **2005,** *71*, 014119.
9. Chen, D.; Wang, Y.; Yu, Y.; Huang, P.; Weng, F. Near-Infrared Quantum Cutting in Transparent Nanostructured Glass Ceramics. *Opt. Lett.* **2008,** *33*, 1884-1886.
10. Xie, L.; Wang, Y.; Zhang, H. Near-Infrared Quantum Cutting in $YPO_4:Yb^{3+}$, Tm^{3+} *via* Cooperative Energy Transfer. *Appl. Phys. Lett.* **2009,** *94*, 061905.
11. Van der Ende, B. M.; Aarts, L.; Meijerink, A. Near-Infrared Quantum Cutting for Photovoltaics. *Adv. Mater.* **2009,** *21*, 3073-3077.
12. Eilers, J. J.; Biner, D.; van Wijngaarden, J. T.; Krämer, K.; Güdel, H.-U.; Meijerink, A. Efficient Visible to Infrared Quantum Cutting Through Downconversion with the Er^{3+}–Yb^{3+} Couple in $Cs_3Y_2Br_9$. *Appl. Phys. Lett.* **2010,** *96*, 151106.
13. Meijer, J.-M.; Aarts, L.; van der Ende, B. M.; Vlugt, T. J. H.; Meijerink, A. Downconversion for Solar Cells in $YF_3:Nd^{3+}$, Yb^{3+}. *Phys. Rev. B* **2010,** *81*, 035107.
14. Lin, H.; Chen, D.; Yu, Y.; Yang, A.; Wang, Y. Near-Infrared Quantum Cutting in Ho^{3+}/Yb^{3+} Codoped Nanostructured Glass Ceramic. *Opt. Lett.* **2011,** *36*, 876-878.
15. Pan, G.; Bai, X.; Yang, D.; Chen, X.; Jing, P.; Qu, S.; Zhang, L.; Zhou, D.; Zhu, J.; Xu, W.; Dong, B.; Song, H. Doping Lanthanide into Perovskite Nanocrystals: Highly Improved and Expanded Optical Properties. *Nano Lett.* **2017,** *17*, 8005-8011.
16. Milstein, T. J.; Kroupa, D. M.; Gamelin, D. R. Picosecond Quantum Cutting Generates Photoluminescence Quantum Yields Over 100% in Ytterbium-Doped $CsPbCl_3$ Nanocrystals. *Nano Lett.* **2018,** *18*, 3792-3799.
17. Kroupa, D. M.; Roh, J. Y.; Milstein, T. J.; Creutz, S. E.; Gamelin, D. R. Quantum-Cutting Ytterbium-Doped $CsPb(Cl_{1-x}Br_x)_3$ Perovskite Thin Films with Photoluminescence Quantum Yields over 190%. *ACS Energy Lett.* **2018,** *3*, 2390-2395.
18. Luo, X.; Ding, T.; Liu, X.; Liu, Y.; Wu, K. Quantum-Cutting Luminescent Solar Concentrators Using Ytterbium-Doped Perovskite Nanocrystals. *Nano Lett.* **2019,** *19*, 338-341.
19. Milstein, T. J.; Kluherz, K. T.; Kroupa, D. M.; Erickson, C. S.; De Yoreo, J. J.; Gamelin, D. R. Anion Exchange and the Quantum-Cutting Energy Threshold in Ytterbium-Doped $CsPb(Cl_{1-x}Br_x)_3$ Perovskite Nanocrystals. *Nano Lett.* **2019,** *19*, 1931-1937.
20. Cohen, T. A.; Milstein, T. J.; Kroupa, D. M.; MacKenzie, J. D.; Luscombe, C. K.; Gamelin, D. R. Quantum-Cutting Yb^{3+}-Doped Perovskite Nanocrystals for Monolithic Bilayer Luminescent Solar Concentrators. *J. Mater. Chem. A* **2019,** *7*, 9279-9288.
21. Crane, M. J.; Kroupa, D. M.; Roh, J. Y.; Anderson, R. T.; Smith, M. D.; Gamelin, D. R. Single-Source Vapor Deposition of Quantum-Cutting $Yb^{3+}:CsPb(Cl_{1-x}Br_x)_3$ and Other Complex Metal-Halide Perovskites. *ACS Appl. Energy Mater.* **2019,** *2*, 4560-4565.

22. Crane, M. J.; Kroupa, D. M.; Gamelin, D. R. Detailed-Balance Analysis of Yb^{3+}:$CsPb(Cl_{1-x}Br_x)_3$ Quantum-Cutting Layers for High-Efficiency Photovoltaics Under Real-World Conditions. *Energy Environ. Sci.* **2019,** *12*, 2486-2495.
23. Zhou, D.; Sun, R.; Xu, W.; Ding, N.; Li, D.; Chen, X.; Pan, G.; Bai, X.; Song, H. Impact of Host Composition, Codoping, or Tridoping on Quantum-Cutting Emission of Ytterbium in Halide Perovskite Quantum Dots and Solar Cell Applications. *Nano Lett.* **2019,** *19*, 6904-6913.
24. Ishii, A.; Miyasaka, T. Sensitized Yb^{3+} Luminescence in $CsPbCl_3$ Film for Highly Efficient Near-Infrared Light-Emitting Diodes. *Adv. Sci.* **2020,** *7*, 1903142.
25. Zeng, M.; Artizzu, F.; Liu, J.; Singh, S.; Locardi, F.; Mara, D.; Hens, Z.; Van Deun, R. Boosting the Er^{3+} 1.5 μm Luminescence in $CsPbCl_3$ Perovskite Nanocrystals for Photonic Devices Operating at Telecommunication Wavelengths. *ACS Appl. Nano Mater.* **2020,** *3*, 4699-4707.
26. Henling, L. M.; McPherson, G. L. EPR Spectra of Magnetically Coupled Pairs of Gd^{3+} Ions in Crystals of $CsMgCl_3$, $CsMgBr_3$, and $CsCdBr_3$. *Phys. Rev. B* **1977,** *16*, 4756-4760.
27. McPherson, G. L.; Henling, L. M. EPR Spectrum of Coupled Pairs of Gd^{3+} Ions in Single Crystals of $CsCdBr_3$. *Phys. Rev. B* **1977,** *16*, 1889-1892.
28. Li, X.; Duan, S.; Liu, H.; Chen, G.; Luo, Y.; Ågren, H. Mechanism for the Extremely Efficient Sensitization of Yb^{3+}Luminescence in $CsPbCl_3$ Nanocrystals. *J. Phys. Chem. Lett.* **2019,** *10*, 487-492.
29. Erickson, C. S.; Crane, M. J.; Milstein, T. J.; Gamelin, D. R. Photoluminescence Saturation in Quantum-Cutting Yb^{3+}-Doped $CsPb(Cl_{1-x}Br_x)_3$ Perovskite Nanocrystals: Implications for Solar Downconversion. *J. Phys. Chem. C* **2019,** *123*, 12474-12484.
30. Linaburg, M. R.; McClure, E. T.; Majher, J. D.; Woodward, P. M. $Cs_{1-x}Rb_xPbCl_3$ and $Cs_{1-x}Rb_xPbBr_3$ Solid Solutions: Understanding Octahedral Tilting in Lead Halide Perovskites. *Chem. Mater.* **2017,** *29*, 3507-3514.
31. Ahtee, M.; Kurki-Suonio, K.; Vahvaselkä, A.; Hewat, A. W.; Harada, J.; Hirotsu, S. Multipole Analysis of the Nuclear Smearing Functions in Caesium Lead Trichloride $CsPbCl_3$. *Acta Crystallogr.* **1980,** *B36*, 1023-1028.
32. Tanner, P. A., Spectra, Energy Levels and Energy Transfer in High Symmetry Lanthanide Compounds. In *Transition Metal and Rare Earth Compounds: Excited States, Transitions, Interactions III*, Yersin, H., Ed. Springer Berlin Heidelberg: Berlin, Heidelberg, 2004; pp 167-278.
33. Tanner, P. A.; Wenyu, L.; Ning, L. Electronic Spectra and Crystal Field Analysis of Tb^{3+} in $Cs_2NaTb(NO_2)_6$: Tb^{3+} Situated at a Site of Th Symmetry. *J. Phys. Chem. C* **2012,** *116*, 12764-12771.
34. Tanner, P. A. Electronic Spectra of Yb^{3+} in Elpasolite Lattices. *Molec. Phys.* **1986,** *58*, 317-328.
35. Bespalov, V. F.; Kazakov, B. N.; Leushin, A. M.; Safiullin, G. M. Crystal Field of Octahedral Yb^{3+} Centers in a $CsCaF_3$ Crystal. *Physics of the Solid State* **1997,** *39*, 925-928.
36. Valiente, R.; Wenger, O. S.; Güdel, H. U. Upconversion Luminescence in Yb^{3+} Doped $CsMnCl_3$: Spectroscopy, Dynamics, and Mechanisms. *J. Chem. Phys.* **2002,** *116*, 5196-5204.
37. Hehlen, M. P.; Kuditcher, A.; Rand, S. C.; Tischler, M. A. Electron–Phonon Interactions in $CsCdBr_3$:Yb^{3+}. *J. Chem. Phys.* **1997,** *107*, 4886-4892.
38. Goldner, P.; Pellé, F.; Meichenin, D.; Auzel, F. Cooperative Luminescence in Ytterbium-Doped $CsCdBr_3$. *J. Lumin.* **1997,** *71*, 137-150.

39. Cape, J. A.; White, R. L.; Feigelson, R. S. EPR Study of the Structure of $CsPbCl_3$. *J. Appl. Phys.* **1969,** *40*, 5001-5005.
40. Cohen, M. I.; Young, K. F.; Chang, T. T.; Brower Jr., W. S. Phase Transitions in $CsPbCl_3$. *J. Appl. Phys.* **1971,** *42*, 5267-5272.
41. Bünzli, J.-C. G. On the Design of Highly Luminescent Lanthanide Complexes. *Coord. Chem. Rev.* **2015,** *293-294*, 19-47.
42. Ryan, J. L.; Jørgensen, C. K. Absorption Spectra of Octahedral Lanthanide Hexahalides. *J. Phys. Chem.* **1966,** *70*, 2845-2857.
43. Dorenbos, P.; Josef, A.; de Haas, J. T. M.; Krämer, K. W. Vacuum Referred Binding Energies of the Lanthanides in Chloride, Bromide, and Iodide Compounds. *J. Lumin.* **2019,** *208*, 463-467.
44. Jørgensen, C. K., Electron Transfer Spectra. In *Progress in Inorganic Chemistry. Volume 12*, Lippard, S. J., Ed. New York, N.Y. : Wiley: New York, N.Y., 1970; pp 101-158.
45. Demirbilek, R.; Heber, J.; Nikitin, S. I., Charge Transfer and $4f^n$-$4f^{n-1}$ 5d Transitions of Trivalent Rare-Earch Ions in $CsCdBr_3$. In *XI Feofilov Symposium on Spectroscopy of Crystals Activated by Rare-Earth and Transition Metal Ions*, SPIE: Kazan, Russian Federation, 2002; Vol. 4766, pp 47-50.
46. Wu, K.; Liang, G.; Shang, Q.; Ren, Y.; Kong, D.; Lian, T. Ultrafast Interfacial Electron and Hole Transfer from $CsPbBr_3$ Perovskite Quantum Dots. *J. Am. Chem. Soc.* **2015,** *137*, 12792-12795.
47. Li, Y.; Shi, Z.-F.; Li, S.; Lei, L.-Z.; Ji, H.-F.; Wu, D.; Xu, T.-T.; Tian, Y.-T.; Li, X.-J. High-performance perovskite photodetectors based on solution-processed all-inorganic $CsPbBr_3$ thin films. *J. Mater. Chem. C* **2017,** *5*, 8355-8360.
48. Lai, R.; Wu, K. Picosecond electron trapping limits the emissivity of $CsPbCl_3$ perovskite nanocrystals. *J. Chem. Phys.* **2019,** *151*, 194701.
49. Tilchin, J.; Dirin, D. N.; Maikov, G. I.; Sashchiuk, A.; Kovalenko, M. V.; Lifshitz, E. Hydrogen-like Wannier–Mott Excitons in Single Crystal of Methylammonium Lead Bromide Perovskite. *ACS Nano* **2016,** *10*, 6363-6371.
50. Chirvony, V. S.; González-Carrero, S.; Suárez, I.; Galian, R. E.; Sessolo, M.; Bolink, H. J.; Martínez-Pastor, J. P.; Pérez-Prieto, J. Delayed Luminescence in Lead Halide Perovskite Nanocrystals. *J. Phys. Chem. C* **2017,** *121*, 13381-13390.

2.8 **Appendix**

2.8.1 *Methods*

Materials. For nanocrystal (NC) syntheses, n-hexane (99%, Sigma Aldrich), 1-octadecene (ODE, 90%, Sigma Aldrich), oleic acid (OA, 90%, Sigma Aldrich), oleylamine (OAm, 70%, Sigma Aldrich), lead acetate trihydrate ($Pb(OAc)_2 \cdot 3H_2O$, 99.999%, Sigma Aldrich), cesium acetate (CsOAc, 99.9%, Sigma Aldrich), trimethylsilyl chloride (TMS-Cl, 98%, Acros Organics), and ethyl acetate (EtOAc, 99%, Sigma Aldrich) were used as received unless otherwise noted. As-received ytterbium acetate hydrate ($Yb(OAc)_3 \cdot xH_2O$, 99.9%, Alfa Aesar) was refluxed in glacial acetic acid for 1 hr and stored in a desiccator prior to use. For single crystal (SC) growth, cesium chloride (CsCl, 99.995%, Merck KGaA) was dried in vacuum at 200°C. Lead chloride ($PbCl_2$) was prepared from lead carbonate ($PbCO_3$, 99.999%, Alfa) and hydrochloric acid (HCl, 30%, suprapure, Merck KGaA). $PbCl_2$ was sublimed in vacuum at 450°C. Ytterbium chloride ($YbCl_3$) was synthesized from ytterbium oxide (Yb_2O_3, 99.9999%, Metall Rare Earth Ltd), sublimed ammonium chloride (NH_4Cl, 99.8%, Merck), and HCl acid [1]. $YbCl_3$ was sublimed in vacuum at 800°C. All starting materials and products were handled under strictly dry and oxygen-free conditions in a glove box (MBraun, Garching) or closed apparatus.

Nanocrystal synthesis. NCs of 1.7% Yb^{3+}:$CsPbCl_3$ were synthesized as detailed previously [2]. In a typical synthesis, $Yb(OAc)_3$ (12 mg, 0.034 mmol) and $Pb(OAc)_2 \cdot 3H_2O$ (76 mg, 0.200 mmol) were combined in a round bottom flask containing ODE (5 mL), OA (1 mL), OAm (0.25 mL), and 1 M CsOAc in EtOH (0.28 mL) and degassed on a Schlenk line at 110 °C for 1 hr. The solid precursors dissolved in this solution at ca. 110 °C. The reaction vessel was then flushed with N_2 and heated to 240 °C, whereupon a solution of 0.2 mL TMS-Cl in 0.5 mL ODE was quickly injected resulting in rapid NC formation. To quench the reaction, the vessel was immediately cooled using a room-temperature water bath. The crude NC solution was then centrifuged and n-hexane was added to the pellet to resuspend the NCs. The NCs were flocculated out of solution with ethyl acetate and centrifuged again for 5 min. The NCs were once again resuspended in n-hexane and centrifuged for 20 min. The supernatant of this solution was collected and contained the final nanocrystal product. Colloidal $CsPbCl_3$ NCs are not hygroscopic like their bulk counterparts, and they can be handled and stored in air without degradation over timescales relevant to the experiments reported here. These NC samples were stored in the dark in ambient

atmosphere.

Single-crystal growth. Large crystals of Yb^{3+}-doped $CsPbCl_3$ were grown from melts of stoichiometric admixtures of CsCl, $PbCl_2$, and $YbCl_3$ by the Bridgman technique. The starting materials were sealed in a silica ampoule under vacuum and molten up at 650°C. Then, the temperature was set to 625°C and crystals were grown by slow cooling over about 10 days. Yb^{3+} concentrations are reported as the nominal concentrations of the initial powder mixture. Since the starting material $YbCl_3$ is hygroscopic, all sample handling and storage was done under inert atmosphere. Bulk $CsPbCl_3$ is stable in dry air. For a good thermal contact and in order to avoid any potential deterioration, crystals were sealed under inert helium atmosphere in silica ampules for spectroscopic measurements.

Absorption. Absorption spectra were measured using an Agilent Cary 5000 spectrometer operating in transmission mode.

NIR photoluminescence excitation (PLE). PLE spectra were measured at room temperature using an Edinburgh FLS 1000 photoluminescence spectrometer equipped with a 450 W xenon lamp as an excitation source and a spectral bandwidth of 1 nm. NIR PL was focused into a monochromator with a spectral bandwidth of 1 nm, detected by a Hamamatsu InGaAs/InP NIR photomultiplier.

2.8.2 *Additional data and analysis*

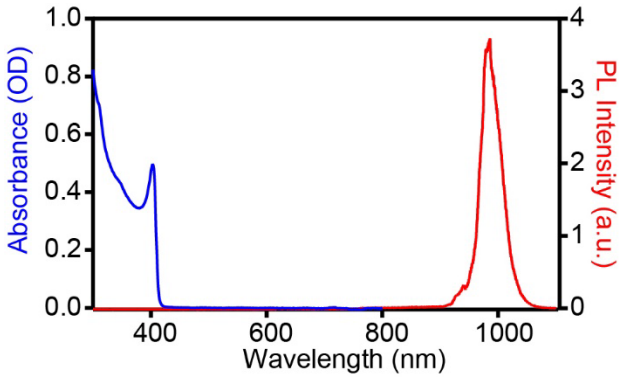

Figure 2.6. Overview room-temperature absorption (blue) and photoluminescence (PL) (red) spectra of 1.7 % Yb^{3+}:$CsPbCl_3$ NCs. λ_{ex} = 375 nm.

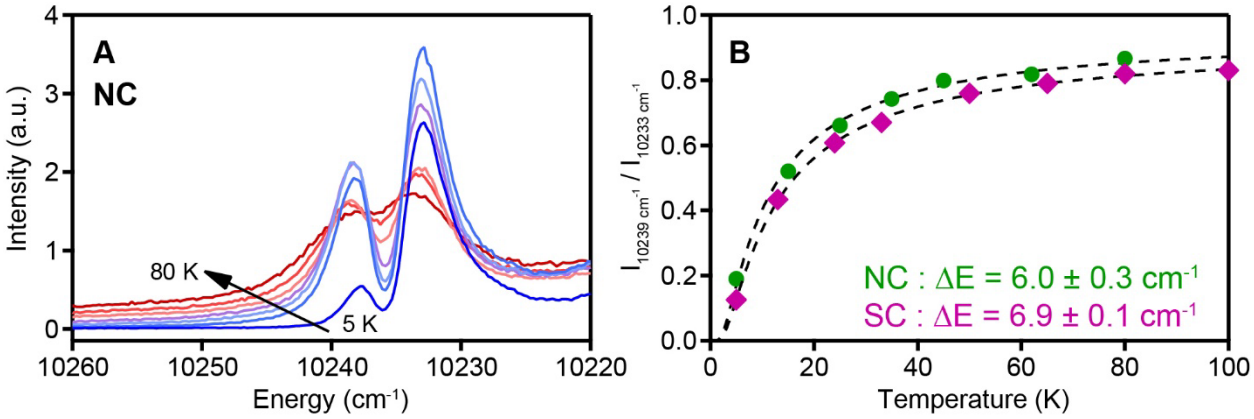

Figure 2.7. (a) Variable-temperature PL spectra of Yb^{3+}:$CsPbCl_3$ NCs from Figures 2.2 and 2.4, measured from 5 (blue) to 80 K (red). **(b)** The ratio of PL intensities of the hot band (10239 cm^{-1}) and the first electronic origin (10233 cm^{-1}) measured for the NCs (green) and the SC (purple), plotted as a function of temperature and fitted (dashed black) using the Boltzmann distribution equation of eq 2.4. λ_{ex} = 375 nm.

The intensity ratios plotted in Figure 2.7b *vs* temperature (T) were fitted using eq 2.4, where I_i and I_0 denote peak intensities at 10239 and 10233 cm^{-1}, respectively, and ΔE is the floating variable. The fits yield ΔE = 6.0 ± 0.3 and 6.9 ± 0.1 cm^{-1} for the NC and SC samples, respectively. These fit results agree well with the $\Gamma_8(^2F_{5/2})$ splitting energy of ~6 cm^{-1} measured spectroscopically (10239 - 10233 cm^{-1}).

$$\frac{I_i}{I_0} \propto e^{\frac{\Delta E}{k_b T}} \tag{2.4}$$

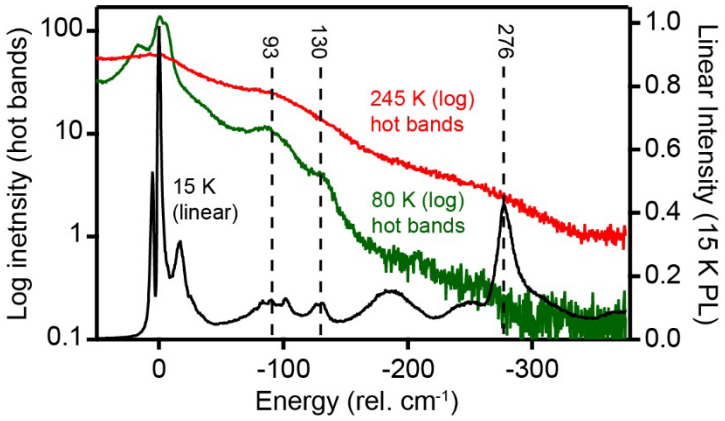

Figure 2.8. The PL spectra of the 1.7% Yb^{3+}:$CsPbCl_3$ NCs from Figure 2.2b, replotted to show direct comparison of the 15 K quantum-cutting PL spectrum with the PL hot bands observed at 80 and 245 K. The 15 K PL spectrum is plotted on a linear y scale and the hot-

band spectra are plotted on a logarithmic *y* scale. The vertical lines are guides to the eye to indicate coincidences between cold and hot band energies. λ_{ex} = 375 nm.

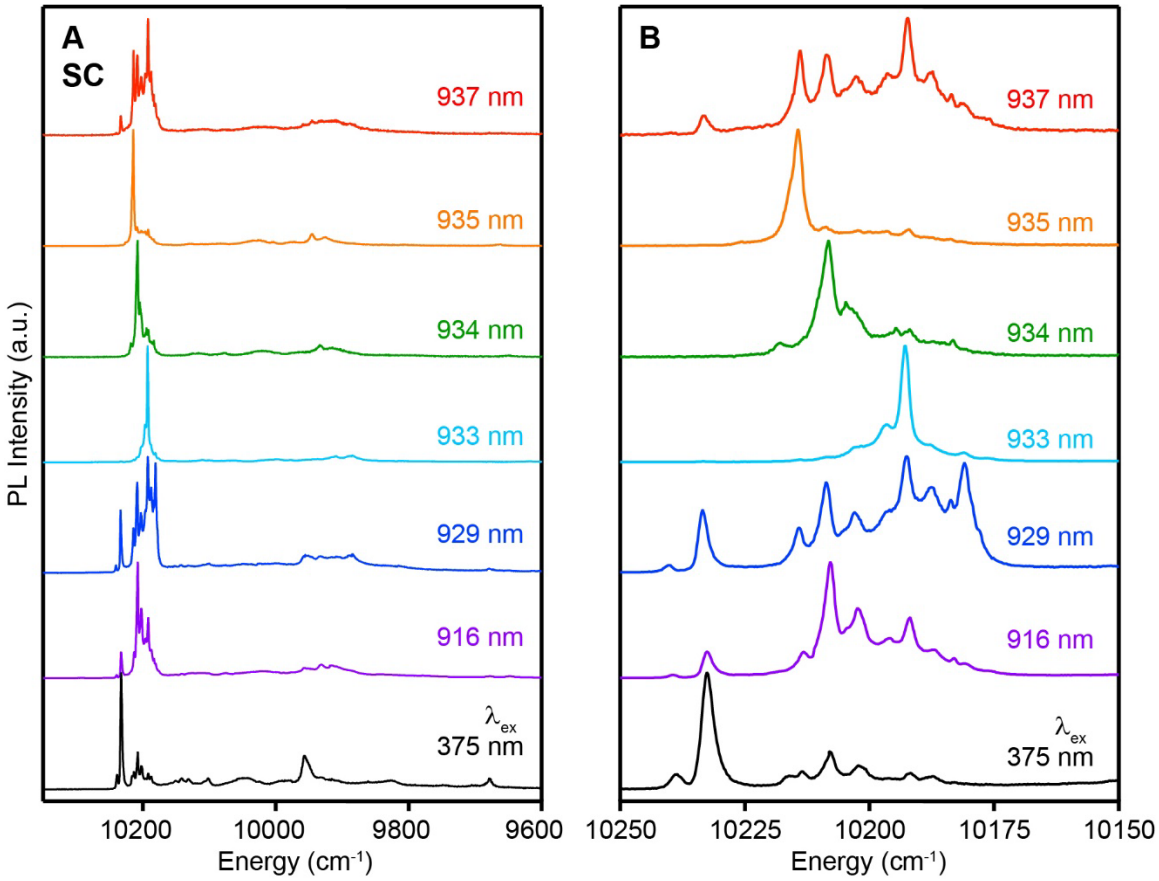

Figure 2.9. (a) 5 K PL spectra of the Yb^{3+}:$CsPbCl_3$ SC measured using site-selective laser excitation at 916 (purple), 929 (dark blue), 933 (blue), 934 (green), 935 (orange), and 937 (red) nm. The perovskite-sensitized quantum-cutting Yb^{3+} PL spectrum excited at 375 nm (black) is included for comparison. **(b)** An expanded view of the set of peaks at highest energies in panel (a).

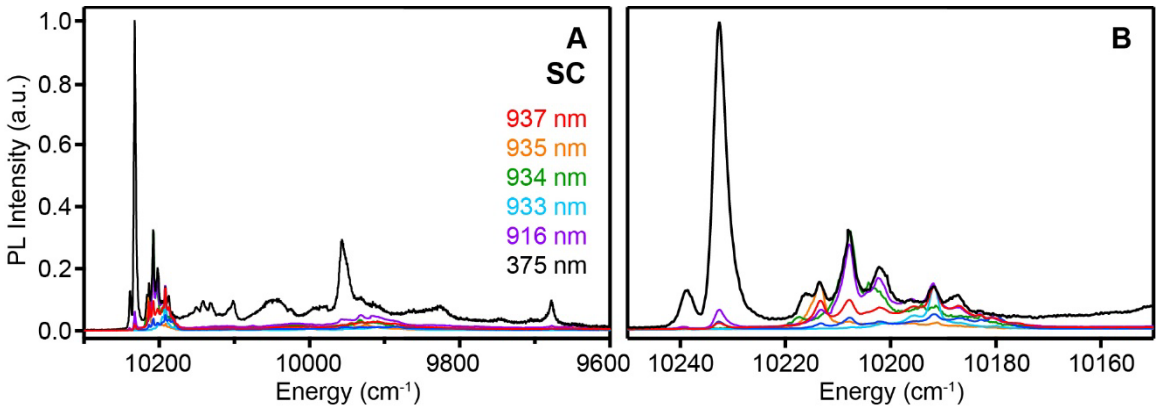

Figure 2.10. (a) 5 K PL spectra of the Yb^{3+}:$CsPbCl_3$ SC from Figure 2.9 (colored), scaled to reflect the maximum possible contribution of each to the quantum-cutting PL spectrum (black). **(b)** An expanded view of the set of peaks at highest energies from panel (a).

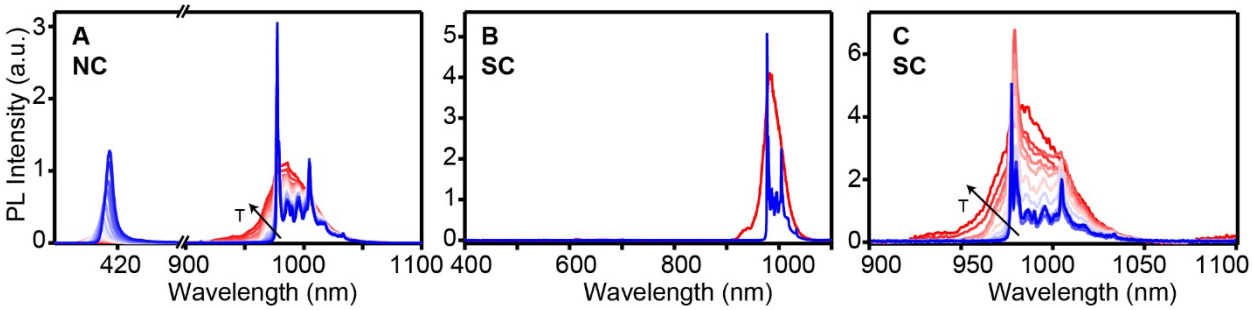

Figure 2.11. Variable-temperature PL spectra of **(a)** Yb^{3+}:$CsPbCl_3$ NCs ([Yb^{3+}] = 1.7%) and **(b)**, **(c)** the Yb^{3+}:$CsPbCl_3$ SC ([Yb^{3+}] = 2%(nom.)) measured from 5 (blue) to 295 K (red). There was no excitonic PL from the Yb^{3+}:$CsPbCl_3$ SC detectable at any temperature. λ_{ex} = 375 nm.

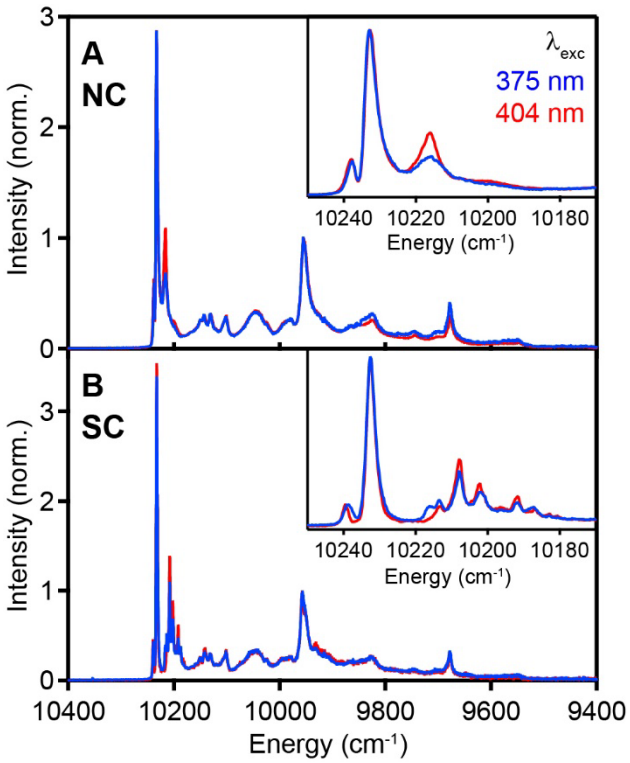

Figure 2.12. 5 K PL spectra of **(a)** Yb^{3+}:$CsPbCl_3$ NCs and **(b)** the Yb^{3+}:$CsPbCl_3$ SC, normalized to the peak at ~9960 cm^{-1}, measured using excitation at 375 (blue) and 404 nm (red). *Insets*: Expanded views of the set of peaks at highest energies. The spectra collected at the two different excitation wavelengths are very similar but not identical.

Average Yb^{3+} PL decay times for the Yb^{3+}:$CsPbCl_3$ SC were determined by fitting the PL decay traces in Figure 2.4b to a biexponential function. The amplitude-weighted average of decay time constants, $\tau_{decay}(avg)$, are given by eq 2.5, where A_n denotes the amplitude of the nth decay component, τ_n. These weighted averages are plotted in Figure 2.5d. The complete fitting results for the Yb^{3+}:$CsPbCl_3$ SC are summarized in Table 2.2.

$$\tau_{decay}(avg) = \frac{\sum A_n \tau_n^2}{\sum A_n \tau_n} \tag{2.5}$$

Table 2.2. Fitting parameters obtained from analysis of Yb^{3+} PL decay data for the 2% Yb^{3+}:$CsPbCl_3$ SC.

Temp. (K)	A_1	τ_1 (ms)	A_2	τ_2 (ms)	τ_{decay}(avg) (ms)
5	0.527	2.98	0.473	5.70	4.70
15	0.523	2.74	0.478	5.44	4.48
25	0.405	2.39	0.595	4.91	4.29
30	0.181	1.46	0.820	4.12	3.93
45	0.177	1.24	0.823	3.84	3.67
60	0.164	0.85	0.836	3.50	3.38
80	0.137	0.72	0.863	3.34	3.25
100	0.206	0.48	0.795	2.83	2.73
125	0.331	0.38	0.669	2.47	2.32
150	0.345	0.45	0.655	2.15	1.98
200	0.391	0.26	0.609	1.75	1.62
250	0.447	0.20	0.553	1.48	1.36
295	0.476	0.13	0.524	1.35	1.25

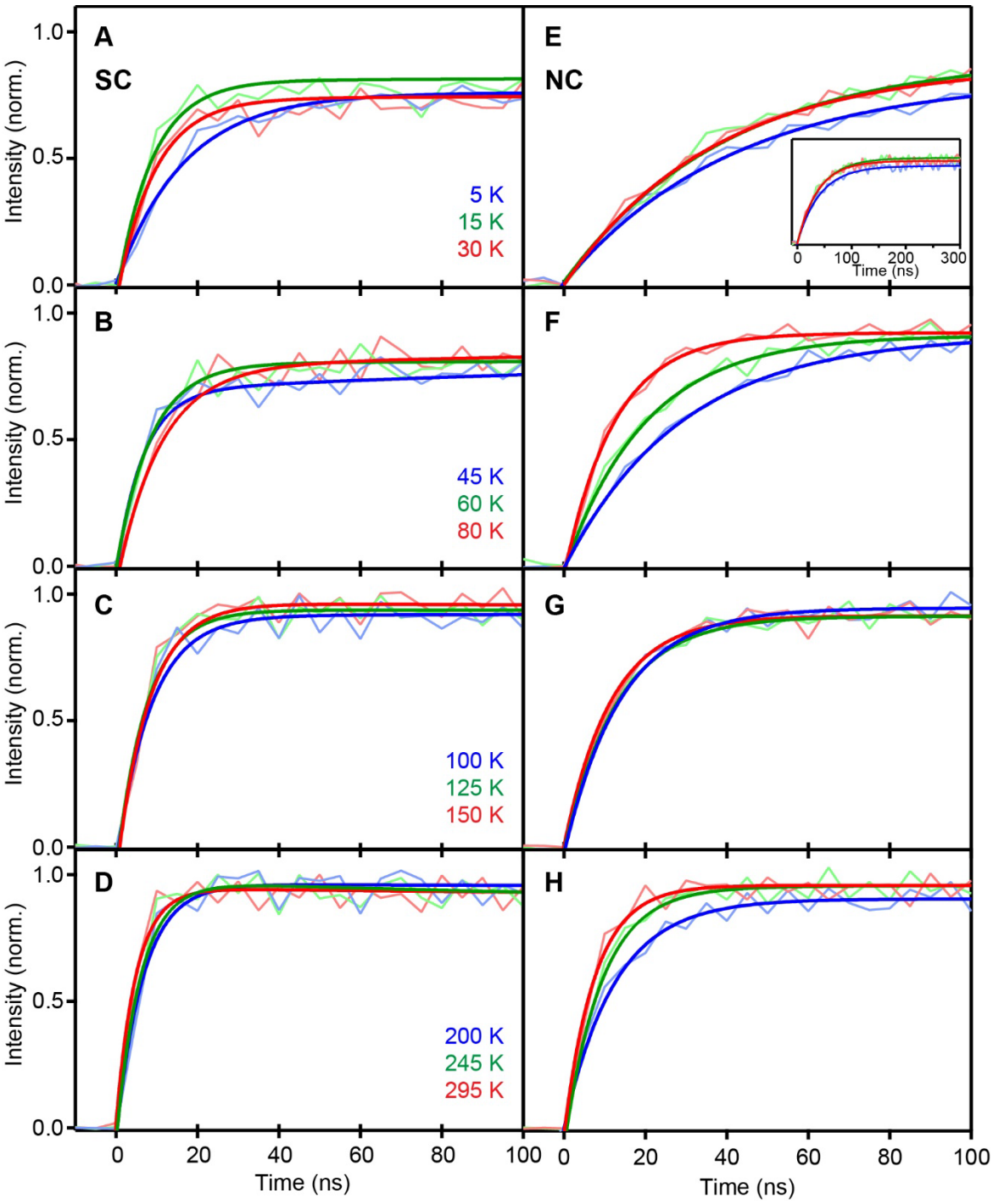

Figure 2.13. First 100 ns of TRPL traces (faint lines) measured at various temperatures from 5 to 295 K, and bi-exponential fits (solid lines) of each experimental trace. **(a)**, **(b)**, **(c)**, **(d)** Data for the 2.0%(nom.) Yb^{3+}:$CsPbCl_3$ SC, and **(e)**, **(f)**, **(g)**, **(h)** data for the 1.7% Yb^{3+}:$CsPbCl_3$ NCs. *Inset to panel (e)*: First 300 ns of the TRPL traces and fits for the NC data measured at 5, 15, and 30 K, showing the complete rise. λ_{ex} = 404 nm, λ_{em} = 982 nm (at 5-150 K), 985 nm (at 200-295 K).

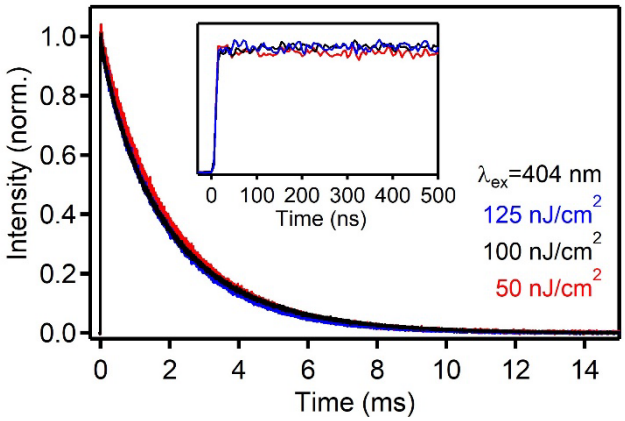

Figure 2.14. Excitation-fluence dependence of Yb^{3+} PL decay measured for the 1.7% Yb^{3+}:$CsPbCl_3$ NCs at room temperature. λ_{ex} = 404 nm, λ_{em} = 985 nm. *Inset*: Expanded view of the first 500 ns of each Yb^{3+} PL decay curve shown in Section 2.4.

Yb^{3+} NIR Photoluminescence Excitation (PLE) Spectra. Numerous publications have reported PLE measurements of both doped and undoped perovskite NCs that appear to show decreasing PLQYs at short excitation wavelengths [3-7]. The large extinction coefficients of $CsPbX_3$ make PLE measurements susceptible to artifacts both experimental in origin and stemming from incorrect data representation. Experimental artifacts come from the fact that the absorption length in concentrated samples is short and changes substantially when the wavelength is scanned above the perovskite absorption edge, resulting in inconsistent PL collection efficiencies under normal measurement conditions. To illustrate, Figure 2.15 plots PLE spectra collected for the same Yb^{3+}:$CsPbCl_3$ NCs at two different concentrations, and shows that at low concentration the first PLE maximum aligns well with the first absorption maximum but at high concentration the first PLE maximum appears red-shifted and the PLE does not continue to rise at shorter wavelengths as the absorption spectrum does. These two observations are both artifacts and can be eliminated by using an integrating sphere during the PLE measurements (see below).

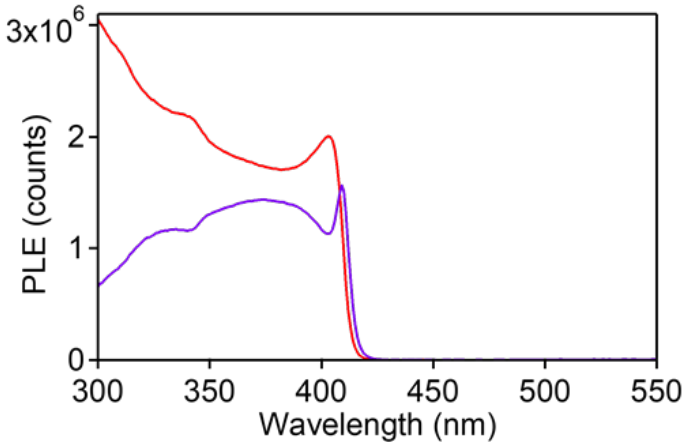

Figure 2.15. PLE spectra of low (red) and high (purple) concentration colloidal 0.3% Yb^{3+}:$CsPbCl_3$ NC samples suspended in hexane, measured without using an integrating sphere. The optical densities of these two samples were 0.22 and 1.88 at the first absorption maximum (403 nm), using a 1.0 cm pathlength cuvette.

Furthermore, PLE intensities reflect sample absorptance, not absorbance, where absorptance (α) is defined as $\alpha = 1 - R - T$, R is reflectance, and T is transmittance. The absorptance approaches unity as the sample's effective concentration or path length increases, suppressing spectral structure at high optical density. To illustrate, Figure 2.16 plots Yb^{3+} NIR PLE spectra of the same Yb^{3+}:$CsPbCl_3$ NCs collected at a series of different NC concentrations, and compares these with the absorptance spectra of the same samples. The PLE and absorptance plots agree well in every case. Only in the limit of large T do the shapes of the absorptance and absorption spectra resemble one another closely, and in this limit the PLE also resembles the absorption spectrum.

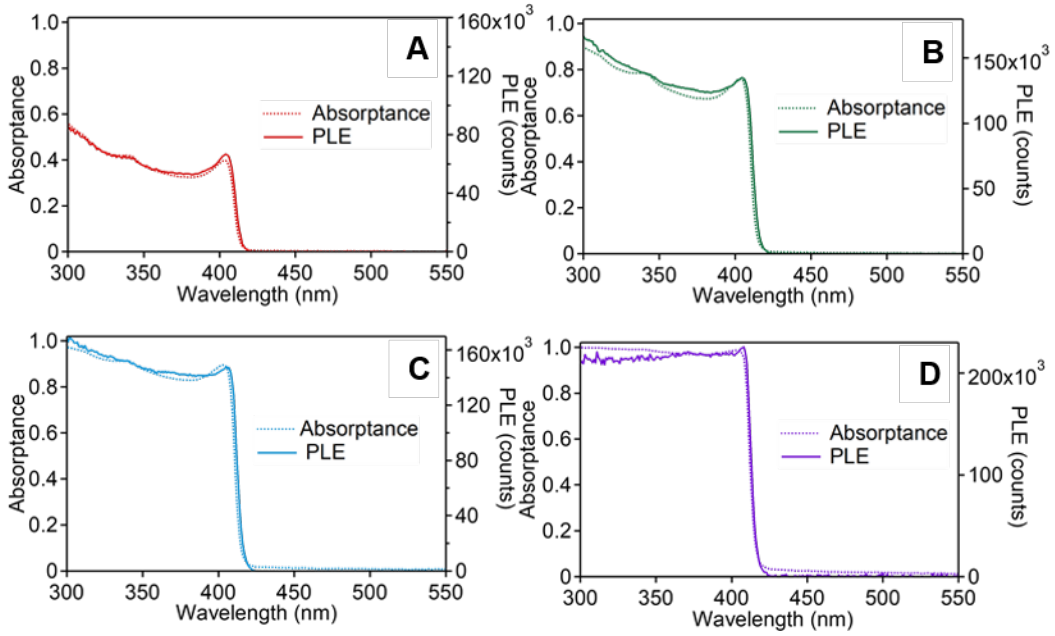

Figure 2.16. Absorptance and PLE spectra of colloidal 0.3% Yb^{3+}:$CsPbCl_3$ NCs at different NC concentrations in hexane. The optical densities at the first absorption maximum (403 nm) were **(a)** 0.22, **(b)** 0.62, **(c)** 0.98, and **(d)** 1.88 for samples, using a 1.0 cm pathlength cuvette. PLE spectra were measured while monitoring the Yb^{3+} *f-f* emission (λ_{em} = 980 nm) using an integrating sphere to capture all emitted photons.

The NC PLE data in Figures 2.15 and 2.16 show that the Yb^{3+} *f-f* luminescence is sensitized by the $CsPbCl_3$ host, and that the PLQY remains essentially constant as the excitation wavelength is scanned across the $CsPbCl_3$ absorption spectrum. Furthermore, no new sub-bandgap features are observed in the PLE spectra, even at the highest NC concentration.

Similar to the scenario with high-optical-density NCs, bulk-crystal PLE spectra with direct $CsPbCl_3$ photoexcitation are strongly influenced by being in the high-optical-density limit. To illustrate, Figure 2.17 plots PLE spectra collected for the 2% Yb^{3+}:$CsPbCl_3$ SC sample in three different powder forms. For the first PLE spectrum, small but macroscopic crystal fragments that were generated during sample cleavage were gathered and used for the PLE measurement. This sample gave a strongly red-shifted first PLE maximum, and a heavily distorted PLE response at shorter excitation wavelengths. This sample was then gently ground twice to reduce crystallite size, and the PLE spectrum was remeasured after each grinding. Reducing the crystallite size dramatically changed the PLE spectrum, reducing and then eliminating these artifacts. In the finest powder, the PLE spectrum now closely resembles the NC PLE spectrum, confirming sensitization of Yb^{3+} by $CsPbCl_3$ in both forms of Yb^{3+}:$CsPbCl_3$.

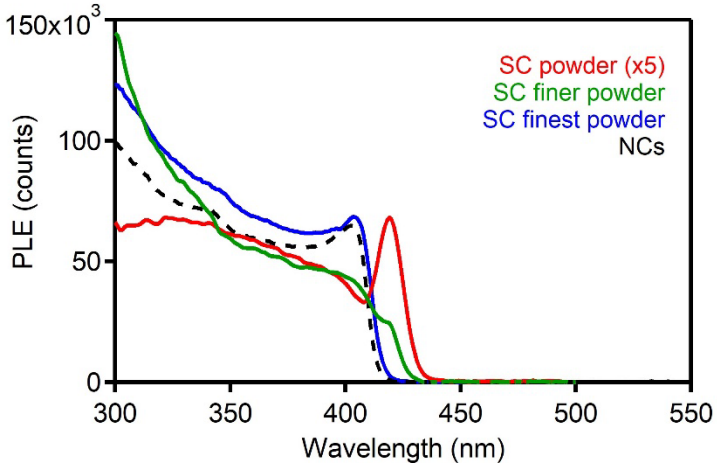

Figure 2.17. PLE spectra of various forms of the 2% Yb^{3+}:$CsPbCl_3$ SC sample described in Section 2.4, measured without an integrating sphere. The PLE spectrum resembles the NC PLE spectrum more and more closely as the grain size decreases, and PLE artifacts are essentially eliminated in the finest powder form. (λ_{em} = 985 nm)

2.8.3 *References*

1. Meyer, G., The Ammonium Ion for Inorganic Synthesis. In *Advances in the Synthesis and Reactivity of Solids*, Mallouk, T. E., Ed. JAI Press: Greenwich, Connecticut, 1994; Vol. 2, pp 1-26.
2. Milstein, T. J.; Kroupa, D. M.; Gamelin, D. R. Picosecond Quantum Cutting Generates Photoluminescence Quantum Yields Over 100% in Ytterbium-Doped $CsPbCl_3$ Nanocrystals. *Nano Lett.* **2018,** *18*, 3792-3799.
3. Zhou, D.; Liu, D.; Pan, G.; Chen, X.; Li, D.; Xu, W.; Bai, X.; Song, H. Cerium and Ytterbium Codoped Halide Perovskite Quantum Dots: A Novel and Efficient Downconverter for Improving the Performance of Silicon Solar Cells. *Adv. Mater.* **2017,** *29*, 1704149.
4. Pan, G.; Bai, X.; Yang, D.; Chen, X.; Jing, P.; Qu, S.; Zhang, L.; Zhou, D.; Zhu, J.; Xu, W.; Dong, B.; Song, H. Doping Lanthanide into Perovskite Nanocrystals: Highly Improved and Expanded Optical Properties. *Nano Lett.* **2017,** *17*, 8005-8011.
5. Zhang, X.; Zhang, Y.; Zhang, X.; Yin, W.; Wang, Y.; Wang, H.; Lu, M.; Li, Z.; Gu, Z.; Yu, W. W. Yb^{3+} and Yb^{3+}/Er^{3+} Doping for Near-Infrared Emission and Improved Stability of $CsPbCl_3$ Nanocrystals. *J. Mater. Chem. C* **2018,** *6*, 10101-10105.
6. Zhou, L.; Liu, T.; Zheng, J.; Yu, K.; Yang, F.; Wang, N.; Zuo, Y.; Liu, Z.; Xue, C.; Li, C.; Cheng, B.; Wang, Q. Dual-Emission and Two Charge-Transfer States in Ytterbium-doped Cesium Lead Halide Perovskite Solid Nanocrystals. *J. Phys. Chem. C* **2018,** *122*, 26825-26834.
7. Zhou, D.; Sun, R.; Xu, W.; Ding, N.; Li, D.; Chen, X.; Pan, G.; Bai, X.; Song, H. Impact of Host Composition, Codoping, or Tridoping on Quantum-Cutting Emission of Ytterbium in Halide Perovskite Quantum Dots and Solar Cell Applications. *Nano Lett.* **2019,** *19*, 6904-6913.

Chapter 3. Negative Thermal Quenching in Quantum-Cutting Yb^{3+}-Doped $CsPb(Cl_{1-x}Br_x)_3$ Perovskite Nanocrystals

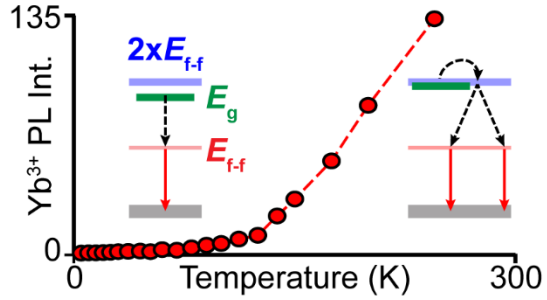

3.1 Overview

Ytterbium-doped all-inorganic lead-halide perovskites (Yb^{3+}:$CsPb(Cl_{1-x}Br_x)_3$) show broadband absorption and exceptionally high near-infrared photoluminescence quantum yields, providing unique opportunities for solar spectral shaping to improve photovoltaic power-conversion efficiencies. Here, we report that Yb^{3+}:$CsPb(Cl_{1-x}Br_x)_3$ NCs also show extremely strong negative thermal quenching of the Yb^{3+} luminescence, with intensities at room temperature >100 times those at 5 K for some compositions. Analysis of this temperature dependence as a function of *x* shows that it stems from thermally activated quantum cutting related to temperature dependence of the spectral overlap between the PL of the perovskite (donor) and the simultaneous-pair absorption of two Yb^{3+} ions (acceptor). In the Yb^{3+}:$CsPbBr_3$ limit, this spectral overlap goes to zero at 5 K, such that only single-Yb^{3+} sensitization requiring massive phonon emission occurs. At room temperature, Yb^{3+} PL in this composition is enhanced ~135 fold by thermally activated quantum cutting, highlighting the extreme efficiency of quantum cutting relative to single-Yb^{3+} sensitization. These results advance the fundamental mechanistic understanding of quantum cutting in doped perovskites, with potential ramifications for solar and photonics technologies.

3.2 Introduction

Optoelectronic materials that promote photomultiplication (*e.g.*, singlet fission, carrier multiplication, and quantum cutting[1-5]) have attracted broad interest because of their potential to overcome the Shockley-Queisser thermodynamic limit in single-junction photovoltaics.[6-8] Such

processes split the energies of single absorbed solar photons to generate multiple lower-energy excitations that, in principal, may be used to generate additional photocurrent and reduce thermalization losses.[9, 10] Ytterbium-doped all-inorganic lead-halide perovskites (Yb^{3+}:$CsPb(Cl_{1-x}Br_x)_3$) have demonstrated extremely efficient quantum cutting, in some cases achieving photoluminescence quantum yields (PLQYs) approaching 200%.[11-13] Unlike quantum cutting in other materials, Yb^{3+}:$CsPb(Cl_{1-x}Br_x)_3$ quantum cutting involves broadband absorption by a direct-bandgap semiconductor, allowing efficient harvesting of solar photons. The near-infrared (NIR) Yb^{3+} emission that results from quantum cutting also aligns very well with the maximum energy-conversion efficiency of crystalline Si photovoltaics.[11-26] These attractive properties have motivated both fundamental and applied investigations into these materials in the forms of colloidal nanocrystals (NCs),[11, 13-16, 18-23, 25, 26] single crystals,[25] and solution-processed and vapor-deposited thin films.[12, 17, 24]

A critical factor in Yb^{3+}:$CsPb(Cl_{1-x}Br_x)_3$ quantum cutting is the energy of the perovskite's lowest excited state relative to that of the Yb^{3+} *f-f* excited states. Narrowing the perovskite energy gap (E_g) in Yb^{3+}:$CsPb(Cl_{1-x}Br_x)_3$ by increasing x from 0.00 ($CsPbCl_3$) to 1.00 ($CsPbBr_3$) initially has little effect but then results in dramatic loss of Yb^{3+} PL intensity as E_g crosses approximately twice the energy of the Yb^{3+} ($^2F_{7/2} \rightarrow {}^2F_{5/2}$) absorption ($2\times E_{f\text{-}f}$, ~20500 cm^{-1}).[20] This behavior was interpreted as reflecting a thermodynamic threshold for energy-conserving quantum cutting.

Here, we report results from variable-temperature (VT) absorption and PL studies of Yb^{3+}:$CsPb(Cl_{1-x}Br_x)_3$ ($0.00 \leq x \leq 1.00$) NCs that reveal a very large negative thermal quenching of Yb^{3+} PL when $E_g < 2\times E_{f\text{-}f}$, increasing by ~135× between 5 and 295 K for $x = 1.00$. We show that this negative thermal quenching stems from a strong temperature dependence of the donor-acceptor spectral overlap between perovskite PL and Yb^{3+}-Yb^{3+} simultaneous-pair absorption spectra, due to both the anti-Varshni shift in E_g and thermal spectral broadening. In the extreme case, we show that quantum cutting is fully suppressed at 5 K for Yb^{3+}:$CsPbBr_3$ NCs ($x = 1.00$), allowing detection of the competing single-Yb^{3+} energy-transfer process for the first time. This process requires massive phonon emission to release ~10000 cm^{-1} excess energy per energy-transfer event, and large increases in Yb^{3+} internal temperature are observed.

The negative thermal quenching reported here is anomalously large for doped perovskites. Previous work has shown that Yb^{3+} PL intensities in Yb^{3+}:$CsPbCl_3$ NCs increase by a modest factor of ~3 upon heating from 5 to 298 K,[13, 25] and that Er^{3+} PL in Yb^{3+}/Er^{3+} co-doped $CsPbCl_3$

NCs and thin films also shows similar increases,[27, 28] but the effect of Br alloying on such PL temperature dependence has never been examined. Indeed, Yb^{3+}:$CsPb(Cl_{1-x}Br_x)_3$ samples with $E_g < 2\times E_{f\text{-}f}$ have received virtually no attention at all and, for example, neither the PL temperature dependence nor even the low-temperature Yb^{3+} PL spectrum of Yb^{3+}:$CsPbBr_3$ have been reported. The new findings presented here advance our mechanistic understanding of Yb^{3+} sensitization in these unique materials, thereby informing their potential future applications in solar or other technologies.

3.3 Results and Discussion

3.3.1 *Yb^{3+}:$CsPb(Cl_{1-x}Br_x)_3$ nanocrystal synthesis, characterization, and anion-exchange chemistry*

Yb^{3+}:$CsPbCl_3$ NCs were prepared by hot-injection using TMS-Cl as the halide source, as reported previously (see Section 3.5).[13, 18, 20, 25] Yb^{3+}:$CsPb(Cl_{1-x}Br_x)_3$ NCs with x up to 1.00 were prepared from these Yb^{3+}:$CsPbCl_3$ NCs by post-synthetic anion exchange using trimethylsilyl bromide (TMS-Br).[29-31] Yb^{3+}:$CsPbBr_3$ NCs were also synthesized directly by hot-injection of TMS-Br. X-ray diffraction and transmission electron microscopy (TEM) data for these NCs resemble those reported previously, all showing rectangular shapes with average edge lengths of ~14-17 nm, and powder diffraction that agrees well with the reference perovskite crystal structures with no detectable crystalline impurities (Figures 3.7, 3.8).

3.3.2 *The effects of anion exchange on Yb^{3+}:$CsPb(Cl_{1-x}Br_x)_3$ nanocrystal photoluminescence*

Figure 3.1 plots exciton and Yb^{3+} PL spectra for 0.2% Yb^{3+}:$CsPbCl_3$, 0.2% Yb^{3+}:$CsPb(Cl_{1-x}Br_x)_3$ NCs at various anion compositions (x), and 7.8% Yb^{3+}:$CsPbBr_3$ NCs, each measured at several temperatures from 5 to 295 K using continuous-wave (CW) excitation. Due to the low dopant concentrations used in Figures 3.1a, b, the excitonic PL is substantially stronger than the Yb^{3+} PL in some of these spectra, and the NIR region has been magnified in the figure (250× and 30×) for clarity. At 5 K, the Yb^{3+} $^2F_{5/2} \rightarrow {}^2F_{7/2}$ PL of the Yb^{3+}:$CsPbCl_3$ NCs (Figure 3.1a) shows several resolved features, as previously reported.[13, 25] Elevating the temperature broadens these features and also causes an *increase* in the integrated NIR PL intensity (*i.e.*, negative thermal quenching)

until near room temperature, where nonradiative relaxation is sometimes observed to decrease intensities again. In concert, the excitonic PL intensities gradually decrease with increasing temperature, accompanied by the expected anti-Varshni blue shifts.[13, 32, 33] Note that the onset and magnitude of the Yb^{3+} PL intensity decrease at high temperature varies from sample to sample (*e.g.*, it is not observed in the 3.5% and 7.8% Yb^{3+}:$CsPb(Cl_{1-x}Br_x)_3$ NCs of this study, Figures 3.13, 3.14),[13, 25] and it is therefore not considered further in our analysis. Figures 3.1d-f summarize this Yb^{3+} PL temperature dependence by plotting the integrated NIR PL intensities at each temperature relative to the 5 K NIR PL intensities of the same sample ($I_{Yb}(T)/I_{Yb}(5\ K)$).

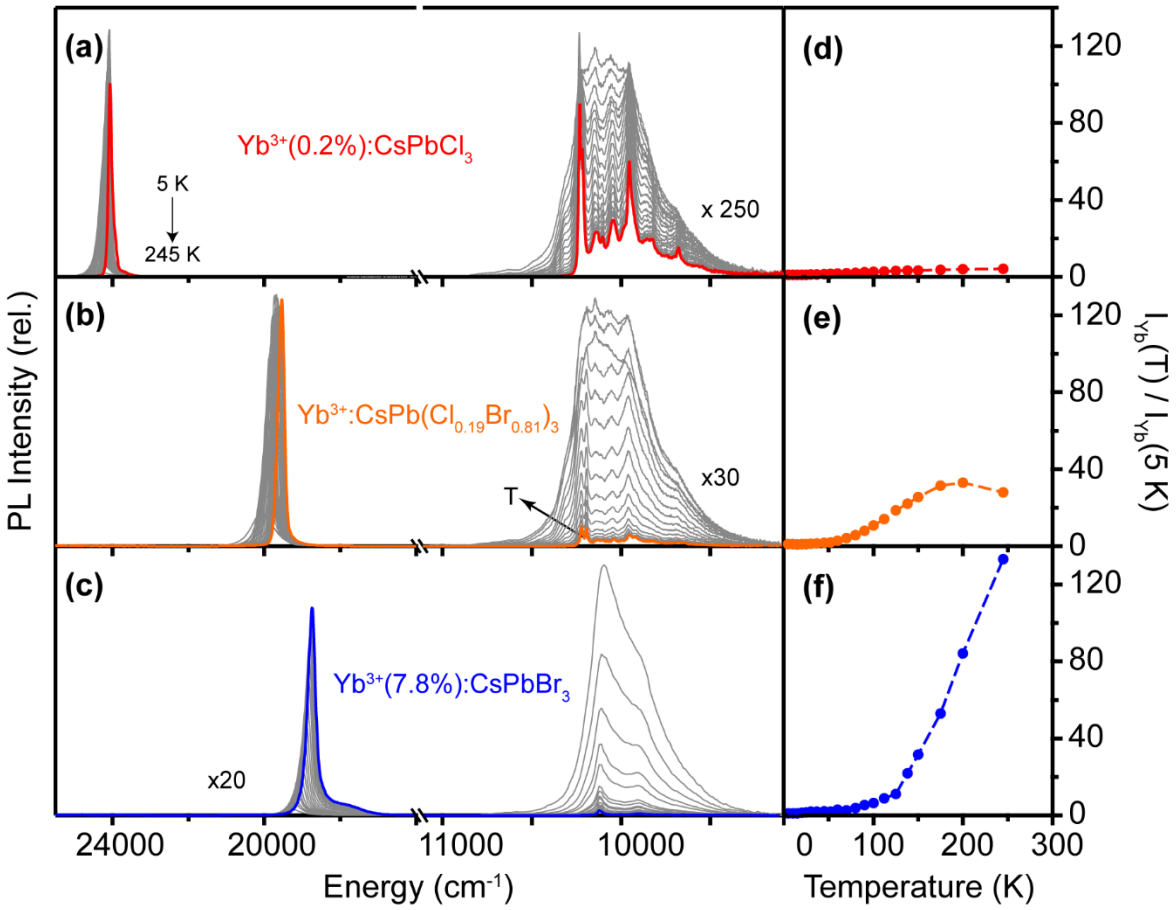

Figure 3.1. VTPL of **(a)** 0.2% Yb^{3+}:$CsPbCl_3$, **(b)** anion-exchanged 0.2% Yb^{3+}:$CsPb(Cl_{0.19}Br_{0.81})_3$, and **(c)** 7.8% Yb^{3+}:$CsPbBr_3$ NCs from 5 (colored) to 295 K. **(d-f)** Integrated Yb^{3+} PL intensity at each temperature point relative to 5 K ($I_{Yb}(T)/I_{Yb}(5\ K)$) is plotted as a function of temperature for each sample from (a-c). All measurements used CW excitation at λ_{ex} = 375 nm (26700 cm^{-1}).

Although the same general trends are observed for all Yb^{3+}:$CsPb(Cl_{1-x}Br_x)_3$ NC samples, a

striking observation from Figure 3.1 is that the Yb^{3+} negative thermal quenching increases dramatically as x increases. For example, Figure 3.1 shows that the Yb^{3+} PL intensity in Yb^{3+}:$CsPbCl_3$ NCs increases roughly 4× going from 5 to 245 K, whereas that of the Yb^{3+}:$CsPbBr_3$ NCs increases by >135×. These data also reveal that the onset of Yb^{3+} negative thermal quenching systematically shifts to higher temperature with increasing x, *e.g.*, from ~5 K in Yb^{3+}:$CsPbCl_3$ NCs (Figure 3.1d) to ~150 K in Yb^{3+}:$CsPbBr_3$ NCs (Figure 3.1f).

The observations described by Figure 3.1 are summarized in a different way in Figure 3.2. Three series of Yb^{3+}:$CsPb(Cl_{1-x}Br_x)_3$ ($0.00 \leq x \leq 1.00$) NCs, having [Yb^{3+}] = 7.8%, 3.5%, and 0.2%, respectively, were prepared by extracting sample aliquots during stepwise partial anion-exchange reactions, and VTPL data were measured for each sample (Figures 3.13-3.15). Figure 3.2a plots the integrated Yb^{3+} PL intensities for each sample measured at room temperature as a function of the sample's excitonic PL energy measured at the same temperature. The data collected at 5 K are also plotted in the same way. At room temperature, the Yb^{3+} PL intensity of the initial Yb^{3+}:$CsPbCl_3$ NCs is retained upon partial anion exchange, but decreases rapidly when $E_g \approx 20000$ cm^{-1}. These room-temperature data follow precisely the trend reported previously,[20] summarized by the dashed curve in Figure 3.2a. We previously interpreted this trend as reflecting the existence of a quantum-cutting energy threshold, defined by $E_g \approx 2 \times E_{f\text{-}f}$.[20] Above this threshold ($E_g > 2 \times E_{f\text{-}f}$), quantum cutting is exothermic and can occur spontaneously. Below this threshold ($E_g < 2 \times E_{f\text{-}f}$), the excited perovskite possesses insufficient energy to excite two Yb^{3+} ions. The data in Figure 3.2a show that decreasing from 295 to 5 K shifts the apparent threshold ~750 cm^{-1} higher in energy. Notably, all three series of samples behave in the same way, showing that these trends are independent of Yb^{3+} concentration.

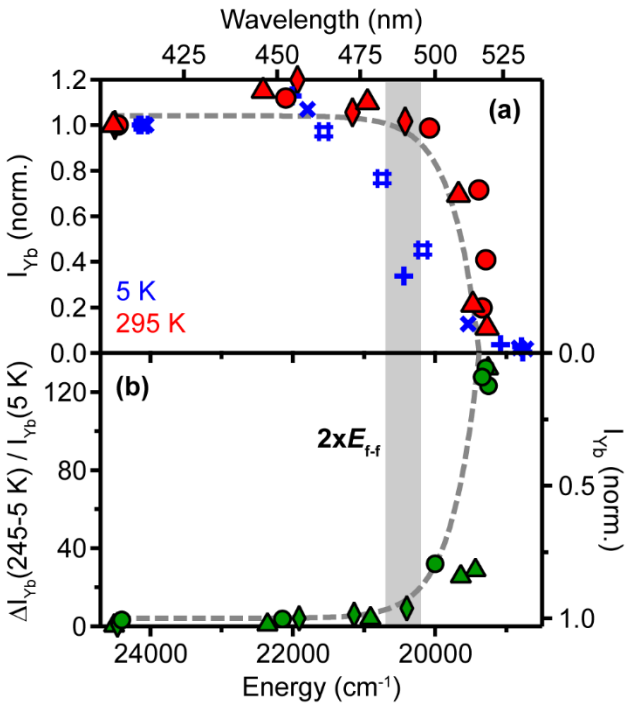

Figure 3.2. (a) Integrated Yb^{3+} ($^2F_{5/2} \rightarrow {}^2F_{7/2}$) PL intensities of (*i*) 0.2% Yb^{3+}:$CsPbCl_3$ and anion-exchanged Yb^{3+}:$CsPb(Cl_{1-x}Br_x)_3$ NCs, and 7.8% Yb^{3+}:$CsPbBr_3$ NCs taken from Figures 3.1 and 3.15 (circles and + marks), (*ii*) 3.5% Yb^{3+}:$CsPbCl_3$ and anion-exchanged Yb^{3+}:$CsPb(Cl_{1-x}Br_x)_3$ (Figure 3.14, diamonds and # marks), (*iii*) 7.8% Yb^{3+}:$CsPbCl_3$ and anion-exchanged Yb^{3+}:$CsPb(Cl_{1-x}Br_x)_3$ NCs, and 5.5% Yb^{3+}:$CsPbBr_3$ NCs from (Figure 3.13, triangles and × marks), all measured at room temperature (solid red marks) and at 5 K (open blue marks). Data are plotted *vs* the exciton PL energy measured at the same temperature, equated with E_g. The gray dashed line reproduces the experimental trend at room temperature reported in ref. [20], showing good agreement. Data for each anion-exchange series are normalized to the Yb^{3+}:$CsPbCl_3$ NC data point of that series, and data points for independently synthesized Yb^{3+}:$CsPbBr_3$ NCs are scaled to match the Yb^{3+}:$CsPb(Cl_{1-x}Br_x)_3$ NC trends in the limit of $x = 1.00$. **(b)** The change in Yb^{3+} PL intensity from 5 to 245 K normalized by the 5 K intensity (ΔI_{Yb}(245-5 K)/I_{Yb}(5 K)) for the samples in Figure 3.2a, plotted *vs* E_g at 245 K for each sample. The vertical gray bar indicates approximately twice the Yb^{3+} ($^2F_{7/2} \rightarrow {}^2F_{5/2}$) absorption threshold ($2\times E_{f\text{-}f}$), representing the proposed quantum-cutting energy threshold.

The difference between the 295 and 5 K curves in Figure 3.2a emphasizes a central conclusion that can be drawn from these data, namely that quantum cutting is strongly temperature dependent when E_g is near the quantum-cutting energy threshold. Figure 3.2b highlights the intimate relationship between the PL temperature dependence and the quantum-cutting energy threshold by plotting the relative Yb^{3+} PL intensity increase from 5 to 245 K (ΔI_{Yb}(245-5 K)/I_{Yb}(5 K)) *vs* the

245 K exciton PL energy (E_g(245 K)) from the Yb^{3+} PL data of Figures 3.1, 3.13-3.15. This plot shows the same curvature as found in Figure 3.2a, only inverted (dashed curve). We note that although Yb^{3+}:$CsPbBr_3$ NCs show ΔI_{Yb}(245-5 K)/I_{Yb}(5 K) > 135, the Yb^{3+} PL of this sample is actually extremely dim at all temperatures (Figures 3.2a, 3.13f, 3.15f), meaning the increase in *absolute* Yb^{3+} PL intensity for this composition is still very small (Figure 3.18).

Having established the strong and systematic temperature dependence of Yb^{3+} PL intensities in the region where $E_g \lesssim 2\times E_{f\text{-}f}$, we now turn to clarifying the fundamental origins of this temperature dependence, and specifically we test the hypothesis that it ultimately reflects the changing efficiency of quantum-cutting energy transfer from the perovskite host (donor) to pairs of Yb^{3+} dopants (acceptors). An important factor in this efficiency is the quantum-cutting rate constant (k_{QC}), which can be described within the general framework of Fermi's golden rule using eq 3.1. Here, k_{QC} is a function of the donor/acceptor electronic coupling (M_{DA}) and the overlap (ρ) between donor PL and acceptor absorption spectra.

$$k_{QC} = \frac{2\pi}{\hbar} |M_{DA}|^2 \rho \tag{3.1}$$

The data in Figure 3.2 speak primarily to the effect of changing E_g (through anion exchange) on ρ. To model ρ, we use the experimental near-band-edge PL as the donor emission spectrum for a given temperature and composition, including any contribution from dopant-induced defect states.[33] Previously, we have argued that quantum cutting in this system is concerted,[13] in which case we may consider the acceptor to be a *pair* of Yb^{3+} ions (whether proximal or distal), and the final state in the energy-transfer process to be the pair's doubly excited $|^2F_{5/2}, {}^2F_{5/2}\rangle$ state. In Yb^{3+}:$CsPb(Cl_{1-x}Br_x)_3$, experimental and computational results indicate that direct Yb^{3+}-Yb^{3+} interactions are extremely weak, allowing the Yb^{3+}-Yb^{3+} simultaneous pair absorption spectrum (f_{YbYb} in the visible energy region, $x = 2y$) to be generated from the single-Yb^{3+} absorption spectrum (f_{Yb} in the NIR energy region, y) using the convolution theorem (see Section 3.7),[34, 35] as given by eq 3.2.

$$f_{YbYb}(x) = [f_{Yb}(y)]^2 \tag{3.2}$$

The donor/acceptor spectral overlap for Dexter-type energy transfer can then be quantified using the product of the area-normalized perovskite PL (g_{perov}) and Yb^{3+}-Yb^{3+} pair absorption (f_{YbYb}) spectra as described by eq 3.3.[36, 37]

$$\rho = \int_0^\infty f_{YbYb}(x)\ g_{perov}(x)dx \tag{3.3}$$

Figure 3.3a plots the 5 K Yb^{3+}-Yb^{3+} simultaneous-pair absorption spectrum obtained from the experimental NIR absorption spectrum of a pressed powder of 5.1% Yb^{3+}:$CsPb(Cl_{0.25}Br_{0.75})_3$ NCs using eq 3.2, compared with the perovskite PL spectra collected at the same temperature for these NCs across the full anion-exchange series. Figure 3.3b shows analogous room-temperature data. We note that the Yb^{3+} absorption spectrum is broader than its emission spectrum, which likely reflects the diverse speciation described previously.[25, 38]

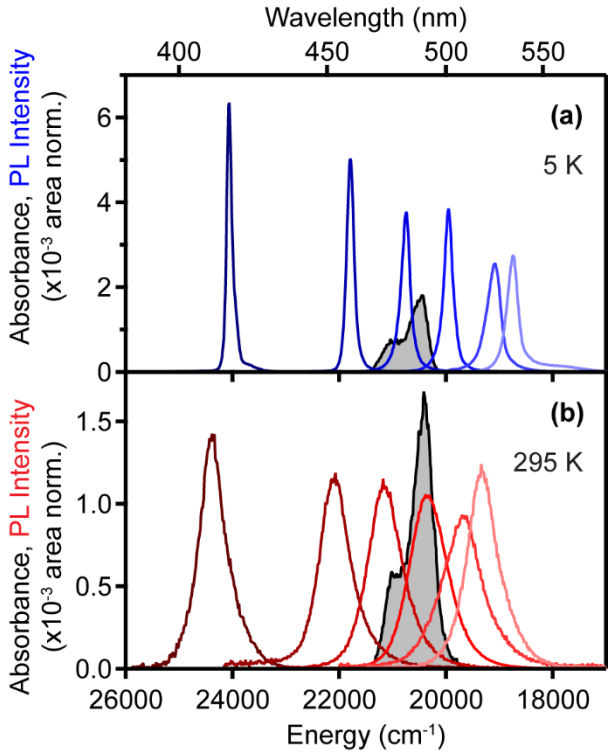

Figure 3.3. (a) Calculated Yb^{3+}-Yb^{3+} simultaneous-pair absorption spectrum ($|^2F_{7/2}, {}^2F_{7/2}\rangle \rightarrow |^2F_{5/2}, {}^2F_{5/2}\rangle$, filled gray) for 5.1% Yb^{3+}:$CsPb(Cl_{0.25}Br_{0.75})_3$ NC powder at 5 K, compared with excitonic PL spectra of Yb^{3+}:$CsPb(Cl_{1-x}Br_x)_3$ NCs also at 5 K. **(b)** Calculated Yb^{3+}-Yb^{3+} simultaneous-pair absorption spectrum for 5.1% Yb^{3+}:$CsPb(Cl_{0.25}Br_{0.75})_3$ NC powder at 295 K, compared with excitonic PL spectra of Yb^{3+}:$CsPb(Cl_{1-x}Br_x)_3$ NCs also at 295 K. All excitonic PL spectra and absorption spectra are area-normalized.

Considering first the high-temperature results (Figure 3.3b), ρ is clearly very small at large E_g, but the data in Figure 3.2a show that quantum cutting is independent of ρ as long as $E_g > 2\times E_{f\text{-}f}$, so eq 3.1 obviously does not fully account for the efficiency of quantum cutting; exothermic (phonon-emitting) quantum cutting in this range must be sufficiently rapid to outcompete other non-productive relaxation channels. In this regime, eq 3.3 is therefore modified as described by eq

3.4.

$$P_{QC} = \int_0^c f_{YbYb}(x)\ g_{Exciton}(x)dx + \int_c^\infty g_{Exciton}(x)\ dx \quad (3.4)$$

Here, c indicates the lowest energy at which 10% of the Yb^{3+}-Yb^{3+} absorption maximum is reached (20230 and 20000 cm^{-1} at 5 and 295 K, respectively, in Figure 3.3). For $x \leq c$, the quantum-cutting energy-transfer probability (P_{QC}) is calculated as in eq 3.3. For $x > c$, P_{QC} is given its maximum value, represented here as the integrated excitonic PL intensities. The value of 10% is arbitrarily chosen to reproduce experiment at room temperature, but qualitatively similar results are obtained for other values between 0 and ~75%. Using eq 3.4, the data in Figure 3.3 can thus be used to model the dependence of I_{Yb} on E_g shown in Figure 3.2a.

Figure 3.4a re-plots excitonic PL and Yb^{3+}-Yb^{3+} simultaneous-pair absorption spectra for 5.1% Yb^{3+}:$CsPb(Cl_{0.25}Br_{0.75})_3$ NCs at 5 and 295 K from Figure 3.3 using an expanded x axis, highlighting the substantial change in spectral overlap for the same sample between these two temperatures. For this sample, E_g is smaller than $2\times E_{f\text{-}f}$ at 5 K but rises to ~$2\times E_{f\text{-}f}$ with increasing temperature, accompanied by spectral broadening, dramatically increasing P_{QC}. The Yb^{3+}-Yb^{3+} pair absorption spectrum also broadens at elevated temperature to a lesser extent. From these spectra, application of eq 3.4 yields the values of P_{QC} indicated by the blue and red stars in Figure 3.4b (5 and 295 K, respectively). Notably, for the sample shown in Figure 3.4a, the spectral overlap increases ~11 fold between 5 and 295 K (*i.e.*, ΔP_{QC}(295-5 K)/P_{QC}(5 K) ≈ 11), which agrees well with the value of ΔI_{Yb}(295-5 K)/I_{Yb}(5 K) = 12.5 measured for this sample (Figure 3.17). Similarly, P_{QC} values have been determined from the other spectra in Figure 3.3 as well as for other independent samples (Figure 3.19), and the results are plotted in Figure 3.4b as blue and red symbols (5 and 295 K, respectively) as a function of E_g.

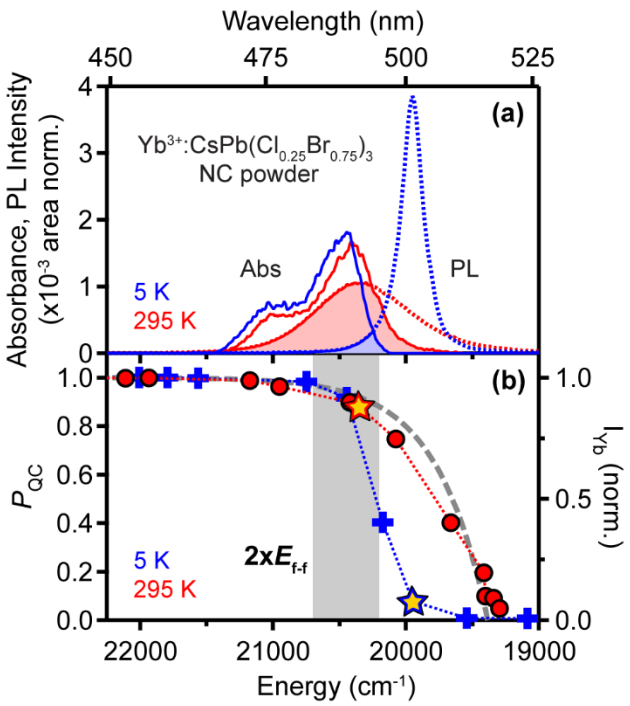

Figure 3.4. (a) Calculated Yb^{3+}-Yb^{3+} simultaneous-pair absorption ($|^2F_{7/2}, {}^2F_{7/2}\rangle \rightarrow |^2F_{5/2}, {}^2F_{5/2}\rangle$, solid traces, calculated) and excitonic PL (dotted traces) spectra of 5.1% Yb^{3+}:$CsPb(Cl_{0.25}Br_{0.75})_3$ NC powder measured at 5 (blue) and 295 K (red). The filled areas correspond to the donor/acceptor spectral overlap at 5 (blue) and 295 K (pink). **(b)** Values of the quantum-cutting energy-transfer probability (P_{QC}) at 5 (blue) and 295 K (red) calculated using eq 3.4 with the Yb^{3+}-Yb^{3+} pair absorption spectra from panel (a) and excitonic PL spectra for Yb^{3+}:$CsPb(Cl_{1-x}Br_x)_3$ ($0.40 \leq x \leq 0.90$) from Figures 3.3 and 3.19 (see Figure 3.21 for the full x range), plotted as a function of E_g at 5 and 295 K, respectively. The gray dashed line is taken from Figure 3.2a. Stars denote P_{QC} values calculated from the spectra in panel (a).

The calculated results in Figure 3.4b agree well with the experimental data in Figure 3.2a, demonstrating that this analysis captures the essence of the experimental phenomenon. This analysis also explains the strong negative thermal quenching observed when $E_g < 2\times E_{f\text{-}f}$ as coming from the combination of temperature-dependent E_g and thermal spectral broadening. The relatively small negative thermal quenching of Yb^{3+}:$CsPbCl_3$ and nearby compositions with when $E_g > 2\times E_{f\text{-}f}$ may reflect thermal acceleration of energy transfer from the intermediate defect state as identified previously.[25]

3.3.3 *Yb^{3+} sensitization below the quantum-cutting energy threshold*

The sensitization mechanism operative in Yb^{3+}:$CsPbBr_3$ deserves special mention, because in this

case E_g is well below $2\times E_{f\text{-}f}$. The energy mismatch between donor (E_g) and acceptor (single $|^2F_{5/2}\rangle \rightarrow |^2F_{7/2}\rangle$) transitions in this case is very large (~10000 cm^{-1}), and for energy conservation must be compensated, *e.g.*, by nonradiative multiphonon emission or Auger-type carrier excitation.

Figure 3.5a compares the 5 K steady-state NIR PL spectra of 0.2% Yb^{3+}:$CsPbCl_3$ and 7.8% Yb^{3+}:$CsPbBr_3$ NCs. The complex Yb^{3+}:$CsPbCl_3$ spectrum has been discussed previously in terms of a combination of crystal-field and vibronic contributions.[25] The Yb^{3+}:$CsPbBr_3$ spectrum has not been reported previously. This spectrum shows a narrow peak at 10113 cm^{-1}, interpreted as the $\Gamma_8 \rightarrow \Gamma_6$ electronic origin (zero-phonon line, compared with the similar peak at 10233 cm^{-1} in Yb^{3+}:$CsPbCl_3$). The energy difference between the Cl and Br peaks is similar to that observed between Yb^{3+}-doped $Cs_2NaHoCl_6$ (10248 cm^{-1}) and $Cs_2NaHoBr_6$ (10144 cm^{-1}).[39] Yb^{3+}:$CsPbCl_3$ shows a low-symmetry splitting of the emissive $\Gamma_8(^2F_{5/2})$ level into 0' and 1' crystal-field components.[25] Similarly, we tentatively assign the Yb^{3+}:$CsPbBr_3$ peaks at 9907 and 9886 cm^{-1} to the split $\Gamma_8(^2F_{7/2})$ level. This splitting (21 cm^{-1}) is comparable those in other bromide lattices (*e.g.* 26 cm^{-1} in $Cs_3Yb_2Br_9$[35] and 52 cm^{-1} in $CsCdBr_3$[40]). The peak at 9645 cm^{-1} is tentatively assigned to the 0' → 3 transition, which is again similar to those in related lattices (9678 cm^{-1} and 9658 cm^{-1} in $Cs_3Yb_2Br_9$[35] and $CsCdBr_3$,[40] respectively). The Yb^{3+} crystal-field splittings in $CsPbBr_3$ are thus similar to those in $Cs_2NaHoBr_6$,[39] $Cs_3Yb_2Br_9$,[35] and $CsCdBr_3$,[40] indicating a similar $[YbBr_6]^{3-}$ structure.

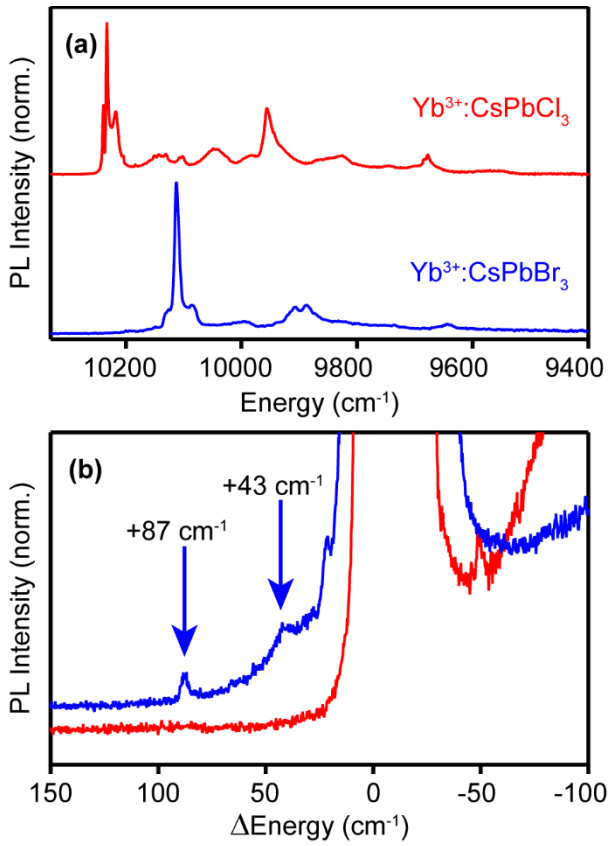

Figure 3.5. (a) 5 K PL spectra of 0.2% Yb^{3+}:$CsPbCl_3$ (red) and 7.8% Yb^{3+}:$CsPbBr_3$ (blue) NCs. **(b)** The PL spectra in panel (a), magnified and replotted on an energy axis relative to the first electronic origins. The spectra in (b) are both normalized at their peak maxima of 10233 and 10113 cm^{-1} for Yb^{3+}:$CsPbCl_3$ and Yb^{3+}:$CsPbBr_3$, respectively. The arrows mark hot bands at ΔE = 43 cm^{-1} and 87cm^{-1} in the Yb^{3+}:$CsPbBr_3$ spectrum. λ_{ex} = 375 nm (26700 cm^{-1}) for both samples.

Figure 3.5b plots the same two spectra on expanded energy and intensity scales, where the energy axis is now referenced to the first electronic origin in each spectrum. The Yb^{3+}:$CsPbBr_3$ NC spectrum shows two weak features at ΔE = +43 and +87 cm^{-1} that have no analog in the Yb^{3+}:$CsPbCl_3$ spectrum, and there is possibly also a third at ΔE = +20 cm^{-1}. These new features both in intensity with increasing temperature relative to the first electronic origin (Figure 3.22) and are thus assigned as "hot" sidebands.

Figure 3.6 shows gated PL spectra of the Yb^{3+}:$CsPbBr_3$ NCs measured at 5 K and collected in 500 ns integration windows at different delay times over the first 4 μs following 40 ps excitation of the perovskite (Figure 3.23). Because of slow emission by Yb^{3+}, these gated spectra could not be collected with the same spectral resolution as the CW PL spectra in Figure 3.5. Nonetheless,

the spectrum collected in the first 500 ns window following excitation shows a dramatic increase in the relative intensity of a feature on the high-energy side of the first electronic origin ($\Delta E \approx +50$ cm^{-1}), attributed to the same hot bands as seen in Figure 3.5b. Note that this hot-band intensity is independent of excitation power under these conditions (Figure 3.25), showing that it is intrinsic to the excitation process. With increasing delay time, the intensity of this peak decreases, and its maximum redshifts slightly to align with the ~43 cm^{-1} feature seen in the CW spectrum of Figure 3.5b. The peak is almost no longer discernible in the spectrum integrated from 3.5 to 4.0 μs. By that time, the spectrum resembles the CW PL spectrum of these Yb^{3+}:$CsPbBr_3$ NCs (Figure 3.5). The inset of Figure 3.6 plots the ratio of I_{hot} to (I_{origin} + I_{hot}) as a function of delay time after excitation. $I_{hot}/(I_{origin} + I_{hot})$ decreases exponentially, approaching the 5 K steady-state value obtained with low-power CW photoexcitation at long times (Figure 3.24). Similar hot bands can be seen for other features throughout the spectrum, but with poorer clarity due to overlapping peaks. These observations suggest extensive local heating of the emissive Yb^{3+}, followed by internal cooling with a time constant of ~2 μs. To estimate the Yb^{3+} internal temperature, the data in Figure 3.6 are compared to CW VTPL spectra of the same NCs (Figure 3.22b). In the VTPL data, the hot band intensities are only reliably quantifiable up to ~70 K, where the thermal contribution to $I_{hot}/(I_{origin} + I_{hot})$ is ~0.20 (using $I_{hot} = I_{+43} + I_{+87}$). The value of $I_{hot}/(I_{origin} + I_{hot})$ ~ 0.40 at $t = 0$ in Figure 3.6 thus indicates an initial Yb^{3+} internal temperature well over 100 K, and likely several hundred degrees Kelvin. A more precise determination of the internal temperature at short times is unreliable because of the high internal temperatures involved.

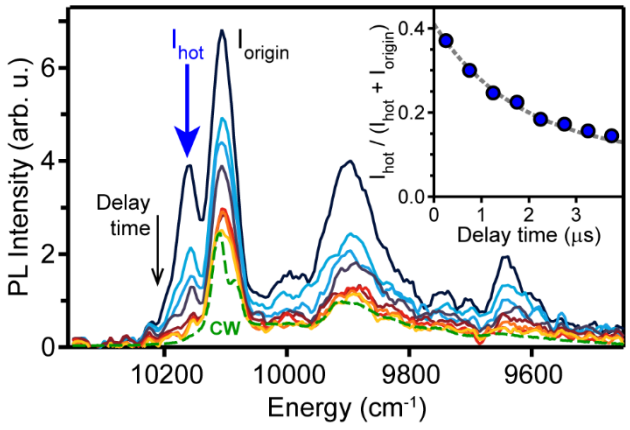

Figure 3.6. PL spectrum of the Yb^{3+}:$CsPbBr_3$ NCs from Figure 3.6a measured at 5 K using CW excitation (green dashed), compared to gated PL spectra collected under the same

conditions over the first 4 μs of decay following a 40 ps laser pulse (solid, λ_{ex} = 355 nm (28200 cm^{-1})). Each gated spectrum was integrated over a 500 ns interval. *Inset:* The ratio of integrated hot-band (10156 cm^{-1}) to first-electronic-origin (10113 cm^{-1}) PL intensities from the gated PL spectra, plotted as a function of delay time after the photoexcitation pulse. The data points mark the centers of the 500 ns integration periods for each delay time. The gray dashed trace shows an exponential fit of the ratio. The spectral bandwidth is ~11 cm^{-1}.

These results highlight that at 5 K, Yb^{3+} sensitization in Yb^{3+}:$CsPbBr_3$ is dominated by direct perovskite-to-Yb^{3+} energy transfer (not quantum cutting), accompanied by nonradiative multiphonon emission of the excess ~10000 cm^{-1} per energy-transfer event which leads to massive Yb^{3+} local heating. No similar local heating is observed in Yb^{3+}:$CsPbCl_3$ (Figures 3.5b, 3.26), reflecting the change in sensitization mechanism above the quantum-cutting energy threshold and emphasizing the much higher *energy* efficiency of the quantum-cutting mechanism.

As described above, the integrated Yb^{3+} PL increases by ~135 times with increasing temperature, attributable to the onset of small but non-zero spectral overlap for resonant concerted quantum cutting. This interpretation is supported by Yb^{3+} PL decay traces measured for these Yb^{3+}:$CsPbBr_3$ NCs. Unlike in Yb^{3+}:$CsPbCl_3$ NCs,[25] the Yb^{3+} PL of Yb^{3+}:$CsPbBr_3$ NCs does not show any discernable Yb^{3+} PL rise time at 5 K but instead primarily decays with a fast time constant (~10s of ns, Figure 3.23), tentatively attributed to the effects of local heating. With increasing temperature, the decay curves grow increasingly similar to those of Yb^{3+}:$CsPbCl_3$ NCs, and by room temperature show slow decay with a rise time of ~10 ns, very similar to Yb^{3+}:$CsPbCl_3$.[25] Critically, although ρ is very small, room-temperature quantum cutting in Yb^{3+}:$CsPbBr_3$ NCs is still >100× *more* efficient than the phonon-assisted single-Yb^{3+} sensitization identified at 5 K, highlighting the extreme efficiency of quantum cutting in these materials.

The results presented above provide new insights into the unique photophysics of Yb^{3+}-doped $CsPb(Cl_{1-x}Br_x)_3$ perovskites by demonstrating a link between the quantum-cutting energy threshold and negative thermal quenching. Scheme 3.1 summarizes the different mechanistic regimes identified in this study. In regime (*i*), Yb^{3+}:$CsPb(Cl_{1-x}Br_x)_3$ NCs ($0.00 \leq x \leq \sim 0.50$) have $E_g > 2\times E_{f\text{-}f}$ and are capable of quantum cutting at all temperatures with release of excess energy *via* phonon emission.[20] In regime (*ii*), Yb^{3+}:$CsPb(Cl_{1-x}Br_x)_3$ NCs ($\sim 0.50 \leq x \leq \sim 1.00$) have $E_g \approx 2\times E_{f\text{-}f}$. At low temperature, these compositions have reduced spectral overlap because their lowest donor transitions occur at energies below the lowest Yb^{3+}-Yb^{3+} simultaneous-pair absorption transitions

and therefore cannot contribute. Compositions in this regime show improved quantum cutting at elevated temperatures with the assistance of thermal band-gap widening and line broadening, manifested as strong negative thermal quenching of Yb^{3+} PL. In regime (*iii*), Yb^{3+}:$CsPb(Cl_{1-x}Br_x)_3$ NCs ($\sim 0.80 \leq x \leq \sim 1.00$) at low temperature have effectively no donor/acceptor spectral overlap and thus show no quantum cutting. In this regime, energy transfer from the perovskite to Yb^{3+} involves an inefficient non-resonant single-Yb^{3+} process that requires massive phonon emission to dissipate ~10000 cm^{-1} per energy-transfer event. This excess energy heats the sample, with internal temperatures of Yb^{3+} reaching hundreds of degrees Kelvin when measured at a cryostat temperature of 5 K. For compositions in regimes (*ii*) and (*iii*), elevated temperatures broaden the donor and acceptor spectra and blueshift the excitonic PL energy, rapidly increasing the spectral overlap required for resonant quantum cutting and causing strong negative thermal quenching of Yb^{3+} PL.

Scheme 3.1. Quantum-cutting energy transfer in Yb^{3+}:$CsPb(Cl_{1-x}Br_x)_3$ NCs for three scenarios: (*i*) $E_g > 2\times E_{f\text{-}f}$, (*ii*) $E_g \approx 2\times E_{f\text{-}f}$, and (*iii*) $E_g < 2\times E_{f\text{-}f}$. At 5 K, energy transfer in (*iii*) occurs only *via* nonradiative multiphonon emission, but at room temperature the same composition shows energy transfer dominated by quantum cutting.

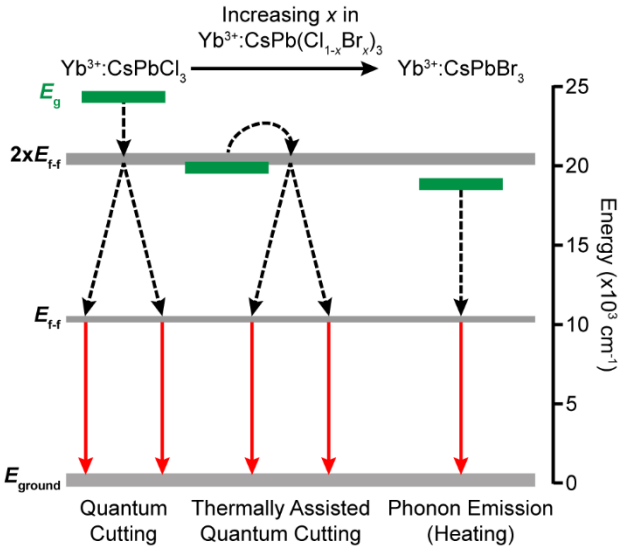

3.4 Conclusion

In summary, we report the observation of strong negative thermal quenching in Yb^{3+}:$CsPb(Cl_{1-x}Br_x)_3$ NCs ($0.00 \leq x \leq 1.00$). Data analysis and modeling conclusively show that this phenomenon

stems from the temperature dependence of quantum cutting. The probability of quantum cutting is modeled in terms of the spectral overlap between donor (perovskite) PL and acceptor (Yb^{3+}-Yb^{3+}) simultaneous pair absorption, which becomes strongly temperature dependent for compositions approaching $CsPbBr_3$. In the limit of Yb^{3+}:$CsPbBr_3$, the dominant energy-transfer mechanism itself changes between 5 K (non-resonant single-ion excitation compensated by multiphonon emission) and room temperature (quantum cutting), resulting in the most dramatic negative thermal quenching of Yb^{3+} PL, with intensities increasing by $>10^2$ over this temperature range. These results advance our fundamental understanding of the photophysical properties of Yb^{3+}:$CsPb(Cl_{1-x}Br_x)_3$ quantum cutters and provide more detailed quantitative assessment of the quantum-cutting mechanism than reported previously, aiding and informing further development of these materials for future solar and photonic applications.

3.5 Experimental

3.5.1 *Nanocrystal synthesis and anion-exchange reaction*

Materials. Oleic acid (OA, 90%, Sigma Aldrich), 1-octadecene (ODE, 90%, Sigma Aldrich), oleylamine (OAm, 70%, Sigma Aldrich), lead acetate trihydrate ($Pb(OAc)_2{\cdot}3H_2O$, 99.999%, Sigma Aldrich), cesium acetate (CsOAc, 99.9%, Sigma Aldrich), anhydrous ethanol (EtOH, 200 proof, Decon Laboratories, Inc.), trimethylsilyl chloride (TMS-Cl, 99%, Sigma Aldrich), trimethylsilyl bromide (TMS-Br, 97%, Sigma Aldrich), n-hexane (99%, Sigma Aldrich), and ethyl acetate (EtOAc, 99%, Sigma Aldrich) were used as received unless otherwise noted. As-received ytterbium acetate hydrate ($Yb(OAc)_3{\cdot}xH_2O$, 99.9%, Alfa Aesar) was refluxed in glacial acetic acid for 1 hour and stored in a desiccator prior to use.

Nanocrystal synthesis. Doped $CsPbX_3$ (X = Cl, Br) NCs were synthesized as detailed previously.[13] In a typical synthesis, $Yb(OAc)_3$ (1-12 mg), $Pb(OAc)_2{\cdot}3H_2O$ (76 mg), ODE (5.0 mL), OA (1.0 mL), OAm (0.25 mL) and 1 M CsOAc in EtOH (0.28 mL) were combined in an oven-dried round bottom flask and degassed on a Schlenk line for 1 hour at 110 °C. The vessel was then flushed with N_2 and heated to 240 °C, whereupon a room-temperature TMS-X solution prepared in a nitrogen-filled glovebox (0.2 mL of TMS-X and 0.5 mL of anhydrous ODE) was injected. Following the injection, the reaction vessel was immediately cooled using a room-temperature water bath. The reaction vessel with the resulting NC solution was transferred to a nitrogen-filled

glovebox, where the solution was centrifuged at 6000 rpm for 10 min. The supernatant was discarded, leaving a white Yb^{3+}-doped $CsPbCl_3$ or yellow Yb^{3+}-doped $CsPbBr_3$ NC pellet. The NC pellet was resuspended in n-hexane and flocculated out of the solution with EtOAc. The suspension then was centrifuged again for 10 min, and the supernatant was discarded. The resulting pellet was resuspended in n-hexane and centrifuged for another 15 min. The supernatant, this time, containing NCs was stored in anhydrous hexane in a nitrogen glovebox.

Nanocrystal pellet preparation. Multiple batches of Yb^{3+}-doped $CsPbCl_3$ NCs in hexane were flocculated out of solution with EtOAc and centrifuged for 20 min, and the supernatant was discarded. The resulting pellet was dried under nitrogen air and broken into powder in mortal and pestle. The resulting powder (~0.2 g) was loaded onto a pellet die and pressed at 8 tons for about 2 min under vacuum.

Anion exchange. Doped $CsPb(Cl_{1-x},Br_x)_3$ NCs were prepared by anion exchange using Yb^{3+}:$CsPbCl_3$ NCs according to protocols as detailed previously.[20, 29, 30] In short, the NC solution stored in a nitrogen glovebox was titrated with 1M TMS-Br until the desired band gap was achieved, as determined by PL spectroscopy at room temperature. The residual TMS-Br and solvent were removed by vacuum evaporation, and the resulting NCs were then resuspended in anhydrous hexane and stored in a nitrogen glovebox.

~30% of the Yb^{3+}:$CsPbCl_3$ NC pellet was anion exchanged to achieve the desired bandgap (Yb^{3+}:$CsPb(Cl_{0.25}Br_{0.75})_3$) via gas-phase anion exchange using neat TMS-Br in a nitrogen-filled glovebox. The anion-exchanged NC powder was loaded onto a pellet die and pressed at 8 tons under vacuum.

3.5.2 *General materials characterization and spectroscopic measurements*

Physical characterization. TEM images were obtained using an FEI TECNAI F20 microscope operating at 200 kV. TEM samples were prepared by dropcasting NCs onto ultrathin carbon-coated copper grids from TED Pella, Inc. Elemental composition of NC samples was determined using inductively coupled plasma-atomic emission spectroscopy (ICP-AES, PerkinElmer 8300). NC samples were prepared by digesting NC powders in concentrated nitric acid overnight with ultrasonication. Then, the nitric acid mixture was diluted in ultrapure H_2O. All dopant concentrations in perovskites were determined as the *B*-site cation mole fraction (in %). pXRD data were collected using a Bruker D8 Discover diffractometer with a high-efficiency IμS

microfocus x-ray source for CuKα radiation (50 kV, 1mA). Samples for XRD measurements were prepared by dropcasting NCs onto a silicon substrate.

Spectroscopic measurements. Samples for variable-temperature NIR absorption measurements were cooled to 5 K in a helium flow cryostat. All absorption spectra were collected using an Agilent Cary 5000 spectrometer operation in transmission mode. Samples for PL and gated PL measurements were prepared by dropcasting NCs onto quartz disks that were cooled to 4.5 K in a closed-cycle helium cryostat (Janis, SHI-4H-5). PL spectra were measured at each temperature using a 375-nm light-emitting diode (LED) for excitation, operating at ~0.6 mW/cm^2. PL data were measured using a LN_2-cooled silicon charge-coupled device (CCD) camera mounted on a monochromator with a spectral bandwidth of about 0.38 nm (~3.87 cm^{-1}) and 0.03 nm (~0.31 cm^{-1}) for variable-temperature and high-resolution PL data, respectively.

For time-resolved PL measurements, photoexcitation was provided by an Ekspla Nd:yttrium aluminum garnet laser (355 nm) firing at a repetition rate of 50 Hz with a 40 ps pulse width. The excitation energy was held at ~35 μJ/cm^2 per pulse. The NIR PL signals were focused into a monochromator, detected by a Hamamatsu InGaAs/InP NIR photomultiplier tube, and recorded using either a multichannel scalar (Stanford Research Systems SR430) or a gated photon counter (Stanford Research Systems, SR400). A spectral bandwidth of 1.10 nm (~11 cm^{-1}) was used for all time-resolved PL measurements.

Photoluminescence excitation (PLE) spectrum was measured at room temperature using an Edinburgh FLS 1000 photoluminescence spectrometer equipped with a 450 W xenon lamp as an excitation source, detected by a Hamamatsu InGaAs/InP NIR photomultiplier with a spectral bandwidth of 1 nm (~10 cm^{-1}).

3.6 References

1. Wegh, R. T.; Donker, H.; Oskam, K. D.; Meijerink, A. Visible Quantum Cutting in $LiGdF_4:Eu^{3+}$ Through Downconversion. *Science* **1999,** *283*, 663-666.
2. Vergeer, P.; Vlugt, T. J. H.; Kox, M. H. F.; den Hertog, M. I.; van der Eerden, J. P. J. M.; Meijerink, A. Quantum Cutting by Cooperative Energy Transfer in $Yb_xY_{1-x}PO_4:Tb^{3+}$. *Phys. Rev. B* **2005,** *71*, 014119.
3. Chen, D.; Wang, Y.; Yu, Y.; Huang, P.; Weng, F. Near-Infrared Quantum Cutting in Transparent Nanostructured Glass Ceramics. *Opt. Lett.* **2008,** *33*, 1884-1886.
4. Van der Ende, B. M.; Aarts, L.; Meijerink, A. Near-Infrared Quantum Cutting for Photovoltaics. *Adv. Mater.* **2009,** *21*, 3073-3077.

5. Eilers, J. J.; Biner, D.; van Wijngaarden, J. T.; Krämer, K.; Güdel, H.-U.; Meijerink, A. Efficient Visible to Infrared Quantum Cutting Through Downconversion with the Er^{3+}–Yb^{3+} Couple in $Cs_3Y_2Br_9$. *Appl. Phys. Lett.* **2010,** *96*, 151106.
6. Shockley, W.; Queisser, H. J. Detailed Balance Limit of Efficiency of *p-n* Junction Solar Cells. *J. Appl. Phys.* **1961,** *32*, 510-519.
7. Dexter, D. L. Two Ideas on Energy Transfer Phenomena: Ion-Pair Effects Involving the OH Stretching Mode, and Sensitization of Photovoltaic Cells. *J. Lumin.* **1979,** *18-19*, 779-784.
8. Trupke, T.; Green, M. A.; Würfel, P. Improving Solar Cell Efficiencies by Down-Conversion of High-Energy Photons. *J. Appl. Phys.* **2002,** *92*, 1668-1674.
9. Hanna, M. C.; Nozik, A. J. Solar Conversion Efficiency of Photovoltaic and Photoelectrolysis Cells with Carrier Multiplication Absorbers. *J. Appl. Phys.* **2006,** *100*, 074510.
10. Nozik, A. J.; Beard, M. C.; Luther, J. M.; Law, M.; Ellingson, R. J.; Johnson, J. C. Semiconductor Quantum Dots and Quantum Dot Arrays and Applications of Multiple Exciton Generation to Third-Generation Photovoltaic Solar Cells. *Chem. Rev.* **2010,** *110*, 6873-6890.
11. Pan, G.; Bai, X.; Yang, D.; Chen, X.; Jing, P.; Qu, S.; Zhang, L.; Zhou, D.; Zhu, J.; Xu, W.; Dong, B.; Song, H. Doping Lanthanide into Perovskite Nanocrystals: Highly Improved and Expanded Optical Properties. *Nano Lett.* **2017,** *17*, 8005-8011.
12. Kroupa, D. M.; Roh, J. Y.; Milstein, T. J.; Creutz, S. E.; Gamelin, D. R. Quantum-Cutting Ytterbium-Doped $CsPb(Cl_{1-x}Br_x)_3$ Perovskite Thin Films with Photoluminescence Quantum Yields over 190%. *ACS Energy Lett.* **2018,** *3*, 2390-2395.
13. Milstein, T. J.; Kroupa, D. M.; Gamelin, D. R. Picosecond Quantum Cutting Generates Photoluminescence Quantum Yields Over 100% in Ytterbium-Doped $CsPbCl_3$ Nanocrystals. *Nano Lett.* **2018,** *18*, 3792-3799.
14. Mir, W. J.; Mahor, Y.; Lohar, A.; Jagadeeswararao, M.; Das, S.; Mahamuni, S.; Nag, A. Postsynthesis Doping of Mn and Yb into $CsPbX_3$ (X = Cl, Br, or I) Perovskite Nanocrystals for Downconversion Emission. *Chem. Mater.* **2018,** *30*, 8170-8178.
15. Zhang, X.; Zhang, Y.; Zhang, X.; Yin, W.; Wang, Y.; Wang, H.; Lu, M.; Li, Z.; Gu, Z.; Yu, W. W. Yb^{3+} and Yb^{3+}/Er^{3+} Doping for Near-Infrared Emission and Improved Stability of $CsPbCl_3$ Nanocrystals. *J. Mater. Chem. C* **2018,** *6*, 10101-10105.
16. Cohen, T. A.; Milstein, T. J.; Kroupa, D. M.; MacKenzie, J. D.; Luscombe, C. K.; Gamelin, D. R. Quantum-Cutting Yb^{3+}-Doped Perovskite Nanocrystals for Monolithic Bilayer Luminescent Solar Concentrators. *J. Mater. Chem. A* **2019,** *7*, 9279-9288.
17. Crane, M. J.; Kroupa, D. M.; Roh, J. Y.; Anderson, R. T.; Smith, M. D.; Gamelin, D. R. Single-Source Vapor Deposition of Quantum-Cutting Yb^{3+}:$CsPb(Cl_{1-x}Br_x)_3$ and Other Complex Metal-Halide Perovskites. *ACS Appl. Energy Mater.* **2019,** *2*, 4560-4565.
18. Erickson, C. S.; Crane, M. J.; Milstein, T. J.; Gamelin, D. R. Photoluminescence Saturation in Quantum-Cutting Yb^{3+}-Doped $CsPb(Cl_{1-x}Br_x)_3$ Perovskite Nanocrystals: Implications for Solar Downconversion. *J. Phys. Chem. C* **2019,** *123*, 12474-12484.
19. Luo, X.; Ding, T.; Liu, X.; Liu, Y.; Wu, K. Quantum-Cutting Luminescent Solar Concentrators Using Ytterbium-Doped Perovskite Nanocrystals. *Nano Lett.* **2019,** *19*, 338-341.
20. Milstein, T. J.; Kluherz, K. T.; Kroupa, D. M.; Erickson, C. S.; De Yoreo, J. J.; Gamelin, D. R. Anion Exchange and the Quantum-Cutting Energy Threshold in Ytterbium-Doped $CsPb(Cl_{1-x}Br_x)_3$ Perovskite Nanocrystals. *Nano Lett.* **2019,** *19*, 1931-1937.

21. Zhou, D.; Sun, R.; Xu, W.; Ding, N.; Li, D.; Chen, X.; Pan, G.; Bai, X.; Song, H. Impact of Host Composition, Codoping, or Tridoping on Quantum-Cutting Emission of Ytterbium in Halide Perovskite Quantum Dots and Solar Cell Applications. *Nano Lett.* **2019,** *19*, 6904-6913.
22. Cai, T.; Wang, J.; Li, W.; Hills-Kimball, K.; Yang, H.; Nagaoka, Y.; Yuan, Y.; Zia, R.; Chen, O. Mn^{2+}/Yb^{3+} Codoped $CsPbCl_3$ Perovskite Nanocrystals with Triple-Wavelength Emission for Luminescent Solar Concentrators. *Adv. Sci.* **2020,** *7*, 2001317.
23. Ding, N.; Xu, W.; Zhou, D.; Ji, Y.; Wang, Y.; Sun, R.; Bai, X.; Zhou, J.; Song, H. Extremely Efficient Quantum-Cutting Cr^{3+}, Ce^{3+}, Yb^{3+} Tridoped Perovskite Quantum Dots for Highly Enhancing the Ultraviolet Response of Silicon Photodetectors with External Quantum Efficiency Exceeding 70%. *Nano Energy* **2020,** *78*, 105278.
24. Ishii, A.; Miyasaka, T. Sensitized Yb^{3+} Luminescence in $CsPbCl_3$ Film for Highly Efficient Near-Infrared Light-Emitting Diodes. *Adv. Sci.* **2020,** *7*, 1903142.
25. Roh, J. Y. D.; Smith, M. D.; Crane, M. J.; Biner, D.; Milstein, T. J.; Krämer, K. W.; Gamelin, D. R. Yb^{3+} Speciation and Energy-Transfer Dynamics in Quantum-Cutting Yb^{3+}-Doped $CsPbCl_3$ Perovskite Nanocrystals and Single Crystals. *Phys. Rev. Mater.* **2020,** *4*, 105405.
26. Zeng, M.; Artizzu, F.; Liu, J.; Singh, S.; Locardi, F.; Mara, D.; Hens, Z.; Van Deun, R. Boosting the Er^{3+} 1.5 μm Luminescence in $CsPbCl_3$ Perovskite Nanocrystals for Photonic Devices Operating at Telecommunication Wavelengths. *ACS Appl. Nano Mater.* **2020,** *3*, 4699-4707.
27. Li, D.; Chen, G. Near-Infrared Photoluminescence from Ytterbium- and Erbium-Codoped $CsPbCl_3$ Perovskite Quantum Dots with Negative Thermal Quenching. *J. Phys. Chem. Lett.* **2023,** *14*, 2837-2844.
28. Li, H.; Liu, X.; Zhou, D.; Dong, B.; Xu, L.; Bai, X.; Song, H. Realization of 1.54-μm Light-Emitting Diodes Based on Er^{3+}/Yb^{3+}Co-Doped $CsPbCl_3$ Films. *Adv. Mater.* **2023**, 2300118.
29. Creutz, S. E.; Crites, E. N.; De Siena, M. C.; Gamelin, D. R. Anion Exchange in Cesium Lead Halide Perovskite Nanocrystals and Thin Films Using Trimethylsilyl Halide Reagents. *Chem. Mater.* **2018,** *30*, 4887-4891.
30. Creutz, S. E.; Crites, E. N.; De Siena, M. C.; Gamelin, D. R. Colloidal Nanocrystals of Lead-Free Double-Perovskite (Elpasolite) Semiconductors: Synthesis and Anion Exchange To Access New Materials. *Nano Lett.* **2018,** *18*, 1118-1123.
31. De Siena, M. C.; Sommer, D. E.; Creutz, S. E.; Dunham, S. T.; Gamelin, D. R. Spinodal Decomposition During Anion Exchange in Colloidal Mn^{2+}-Doped $CsPbX_3$ (X = Cl, Br) Perovskite Nanocrystals. *Chem. Mater.* **2019,** *31*, 7711-7722.
32. Han, Q.; Wu, W.; Liu, W.; Yang, Q.; Yang, Y. Temperature-Dependent Photoluminescence of $CsPbX_3$ Nanocrystal Films. *J. Lumin.* **2018,** *198*, 350-356.
33. Milstein, T. J.; Roh, J. Y. D.; Jacoby, L. M.; Crane, M. J.; Sommer, D. E.; Dunham, S. T.; Gamelin, D. R. Ubiquitous Near-Band-Edge Defect State in Rare-Earth-Doped Lead-Halide Perovskites. *Chem. Mater.* **2022,** *34*, 3759-3769.
34. Ovsyankin, V. V., CHAPTER 7 - Spectroscopy of Collective States and Cooperative Transitions in Disordered Rare-Earth Activated Solids. In *Modern Problems in Condensed Matter Sciences*, Kaplyanskii, A. A.; Macfarlane, R. M., Eds. Elsevier: 1987; Vol. 21, pp 343-480.
35. Hehlen, M. P.; Güdel, H. U. Optical Spectroscopy of the Dimer System $Cs_3Yb_2Br_9$. *J. Chem. Phys.* **1993,** *98*, 1768-1775.
36. Miyakawa, T.; Dexter, D. L. Cooperative and Stepwise Excitation of Luminescence: Trivalent Rare-Earth Ions in Yb^{3+}-Sensitized Crystals. *Phys. Rev. B* **1970,** *1*, 70-80.

37. Kushida, T. Energy Transfer and Cooperative Optical Transitions in Rare-Earth Doped Inorganic Materials. I. Transition Probability Calculation. *J. Phys. Soc. Jpn.* **1973,** *34*, 1318-1326.
38. Sommer, D. E.; Gamelin, D. R.; Dunham, S. T. Defect Formation in Yb-Doped $CsPbCl_3$ from First Principles with Implications for Quantum Cutting. *Phys. Rev. Mater.* **2022,** *6*, 025404.
39. Tanner, P. A. Electronic Spectra of Yb^{3+} in Elpasolite Lattices. *Molec. Phys.* **1986,** *58*, 317-328.
40. Hehlen, M. P.; Kuditcher, A.; Rand, S. C.; Tischler, M. A. Electron–Phonon Interactions in $CsCdBr_3:Yb^{3+}$. *J. Chem. Phys.* **1997,** *107*, 4886-4892.

3.7 Appendix

3.7.1 *Additional structural characterization data for Yb^{3+}:$CsPb(Cl_{1-x}Br_x)_3$ nanocrystals*

Additional TEM images for Yb^{3+}:$CsPbX_3$ nanocrystals

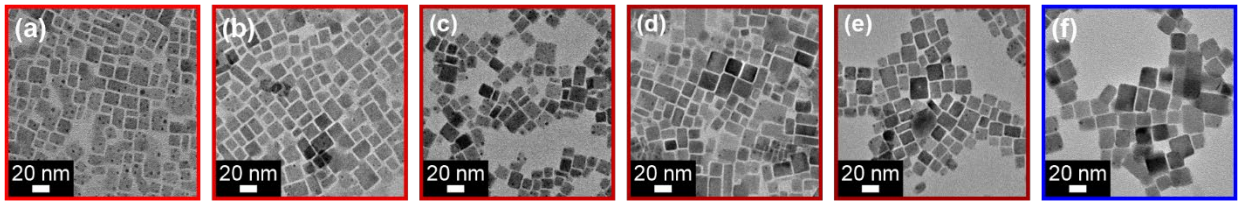

Figure 3.7. Representative transmission electron microscopy (TEM) images of **(a)** 7.8% Yb^{3+}:$CsPbCl_3$ NCs (l = 13.9 ± 2.5 nm), **(b)** anion-exchanged Yb^{3+}:$CsPb(Cl_{0.35}Br_{0.65})_3$ NCs (l = 14.9 ± 2.7 nm) **(c)** Yb^{3+}:$CsPb(Cl_{0.63}Br_{0.37})_3$ NCs (l = 14.4 ± 2.0 nm), **(d)** Yb^{3+}:$CsPb(Cl_{0.07}Br_{0.93})_3$ NCs (l = 15.3 ± 2.6 nm), **(e)** Yb^{3+}:$CsPb(Cl_{0.00}Br_{1.00})_3$ NCs (l = 15.4 ± 2.0 nm) obtained from the 7.8% Yb^{3+}:$CsPbCl_3$ NCs of panel (a), and **(f)** 5.5% Yb^{3+}:$CsPbBr_3$ NCs (l = 17.4 ± 2.3 nm) prepared by direct synthesis. The Br^- mole fraction (x) was determined using Vegard's law analysis of powder X-ray diffraction (pXRD) data.

Additional XRD data for Yb^{3+}:$CsPb(Cl_{1-x}Br_x)_3$ nanocrystals

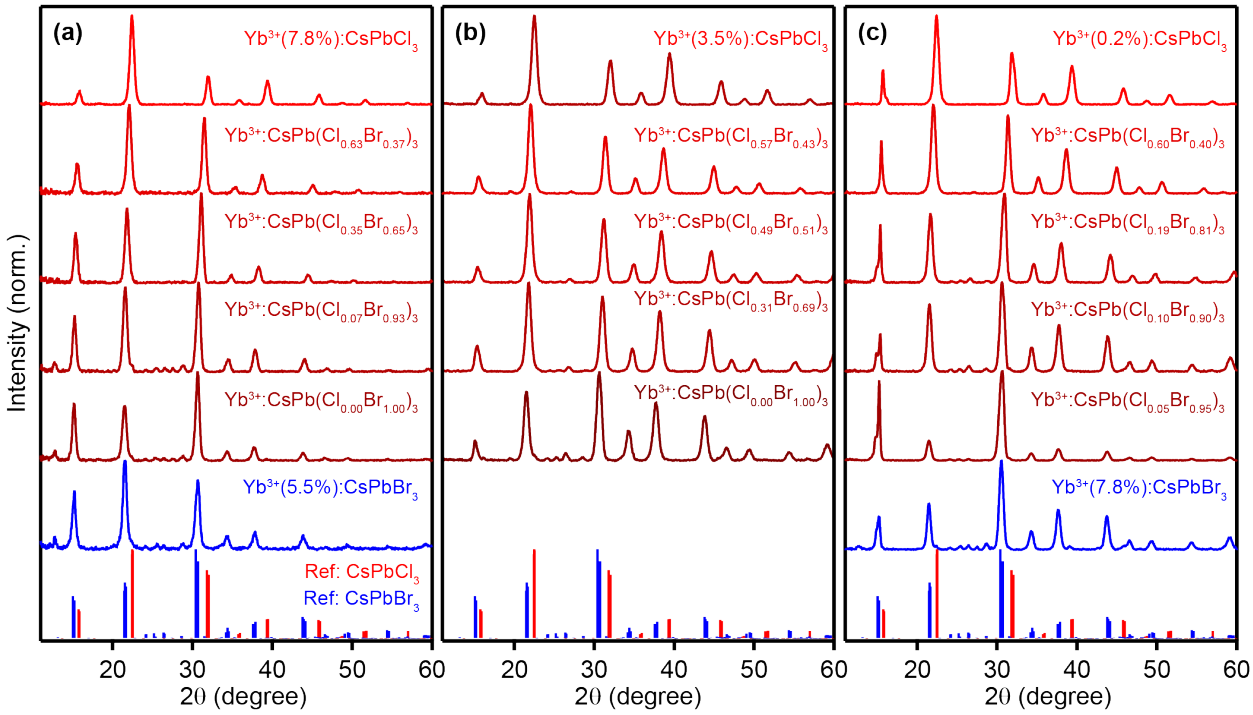

Figure 3.8. Powder X-ray diffraction (pXRD) data collected for the **(a)** 7.8% Yb^{3+}:$CsPbCl_3$ NCs (red), anion-exchanged Yb^{3+}:$CsPb(Cl_{1-x}Br_x)_3$ NCs (dark red, brown) obtained from

the 7.8% Yb^{3+}:$CsPbCl_3$ NCs at the top of the panel, and 5.5% Yb^{3+}:$CsPbBr_3$ NCs (blue) prepared by direct synthesis. PXRD data collected for **(b)** the 3.5% Yb^{3+}:$CsPbCl_3$ NCs (red), anion-exchanged Yb^{3+}:$CsPb(Cl_{1-x}Br_x)_3$ NCs (dark red, brown) obtained from the 3.5% Yb^{3+}:$CsPbCl_3$ NCs, **(c)** 0.2% Yb^{3+}:$CsPbCl_3$ NCs (red), anion-exchanged Yb^{3+}:$CsPb(Cl_{1-x}Br_x)_3$ NCs (dark red, brown) obtained from the 0.2% Yb^{3+}:$CsPbCl_3$ NCs, and 7.8% Yb^{3+}:$CsPbBr_3$ NCs (blue). Reference indices are shown for the cubic high-temperature forms of $CsPbCl_3$ (red) and $CsPbBr_3$ (blue). Although $CsPbCl_3$ and $CsPbBr_3$ adopt the orthorhombic structure (space group *Pnma*) at room temperature,[1] the resulting splittings would not be detectible on the scale shown here.

XRD data for of Yb^{3+}:$CsPb(Cl_{1-x}Br_x)_3$ nanocrystal powders

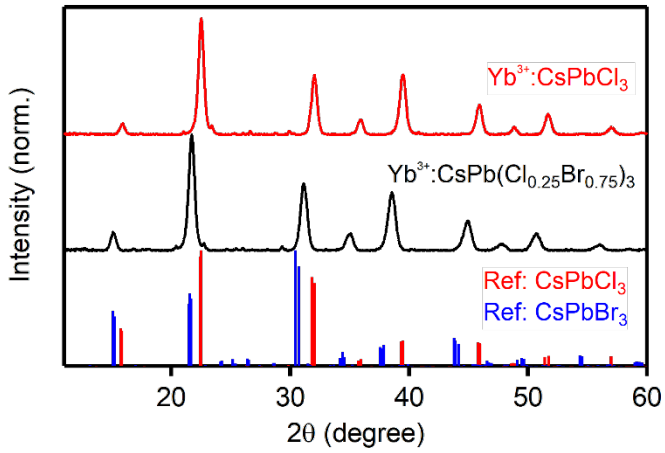

Figure 3.9. pXRD data collected for the Yb^{3+}:$CsPbCl_3$ NC powder (red), anion-exchanged Yb^{3+}:$CsPb(Cl_{0.25}Br_{0.75})_3$ NC powder (black) obtained from the Yb^{3+}:$CsPbCl_3$ NC powder at the top of the panel. Reference: $CsPbCl_3$ (red) and $CsPbBr_3$ (blue).[1]

3.7.2 *Absorption data for Yb^{3+}:$CsPb(Cl_{1-x}Br_x)_3$ nanocrystals*

Room-temperature absorption data for Yb^{3+}:$CsPb(Cl_{1-x}Br_x)_3$ nanocrystals

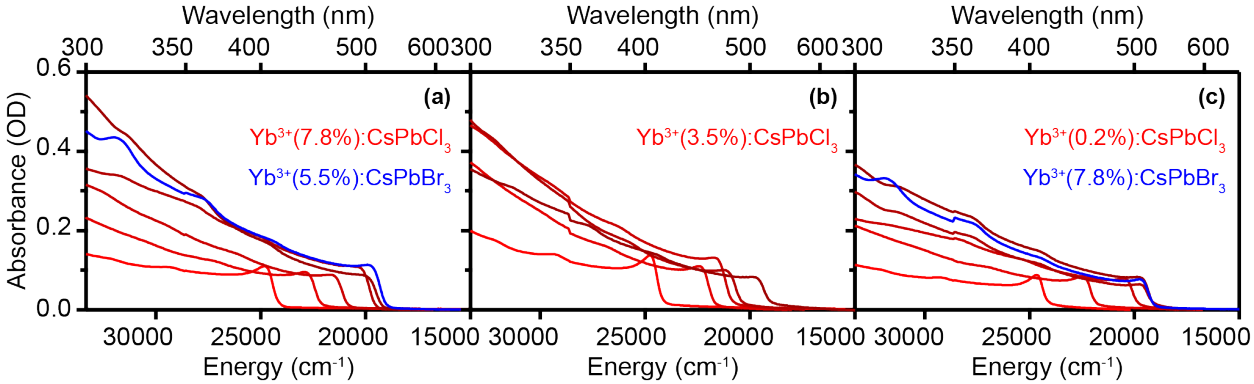

Figure 3.10. Room-temperature absorption spectra for the **(a)** 7.8% Yb^{3+}:$CsPbCl_3$ NCs (red), anion-exchanged Yb^{3+}:$CsPb(Cl_{1-x}Br_x)_3$ NCs (dark red, brown) obtained from the 7.8% Yb^{3+}:$CsPbCl_3$ NCs, and 5.5% Yb^{3+}:$CsPbBr_3$ NCs (blue). Room temperature absorption spectra for **(b)** the 3.5% Yb^{3+}:$CsPbCl_3$ NCs (red), anion-exchanged Yb^{3+}:$CsPb(Cl_{1-x}Br_x)_3$ NCs (dark red, brown) obtained from the 3.5% Yb^{3+}:$CsPbCl_3$ NCs, **(c)** the 0.2% Yb^{3+}:$CsPbCl_3$ NCs (red), anion-exchanged Yb^{3+}:$CsPb(Cl_{1-x}Br_x)_3$ NCs (dark red, brown) obtained from the 0.2% Yb^{3+}:$CsPbCl_3$ NCs, and 7.8% Yb^{3+}:$CsPbBr_3$ NCs (blue).

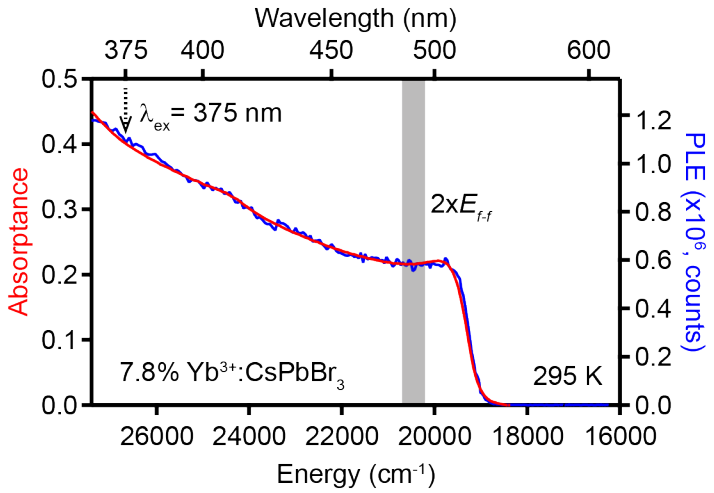

Figure 3.11. Absorptance (red) and photoluminescence excitation (PLE, blue) spectra of 7.8% Yb^{3+}:$CsPbBr_3$ NCs at room temperature. The PLE spectrum was measured while monitoring the Yb^{3+} *f-f* luminescence (λ_{em} = 990 nm) with an integrating sphere to capture all emitted photons. The dotted arrow marks the continuous-wave (CW) excitation

wavelength (λ_{ex} = 375 nm (26700 cm^{-1})) used for all steady-state PL measurements described in this manuscript. The gray bar indicates the proposed quantum-cutting energy threshold ($2\times E_{f\text{-}f}$). These data show that there is no increase in PLQY when exciting above $2\times E_{f\text{-}f}$ relative to exciting below $2\times E_{f\text{-}f}$, ruling out any significant "hot" quantum cutting from upper excited states.

Variable-temperature absorption data for Yb^{3+}:$CsPb(Cl_{1-x}Br_x)_3$ nanocrystal powders

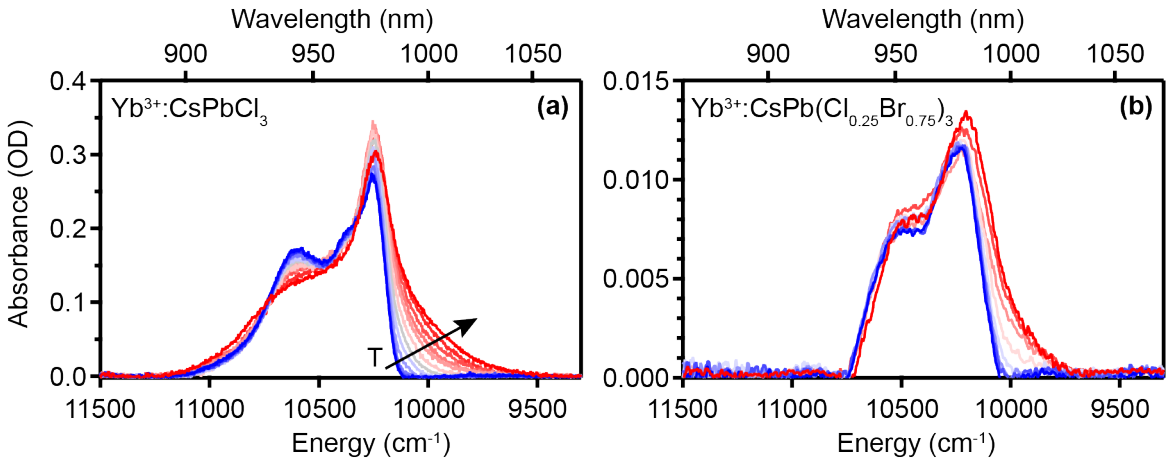

Figure 3.12. Variable-temperature (VT) NIR absorption spectra for the **(a)** Yb^{3+}:$CsPbCl_3$ NC powder from 4.5 (blue) to 295 K (red) and **(b)** anion-exchanged Yb^{3+}:$CsPb(Cl_{0.25}Br_{0.75})_3$ NC powder from 4.5 (blue) to 295 K (red) obtained from Figure 3.12. Temperature points: 4.5, 15, 30, 45, 60, 80, 100, 125, 150, 175, 200, 245, 295 K and 4.5, 30, 60, 100, 150, 200, 245, 295 K, respectively for Yb^{3+}:$CsPbCl_3$ and Yb^{3+}:$CsPb(Cl_{0.25}Br_{0.75})_3$ NC powder.

3.7.3 *Additional photoluminescence data for Yb^{3+}:$CsPb(Cl_{1-x}Br_x)_3$ nanocrystals*

Variable-temperature photoluminescence data for Yb^{3+}:$CsPb(Cl_{1-x}Br_x)_3$ nanocrystals

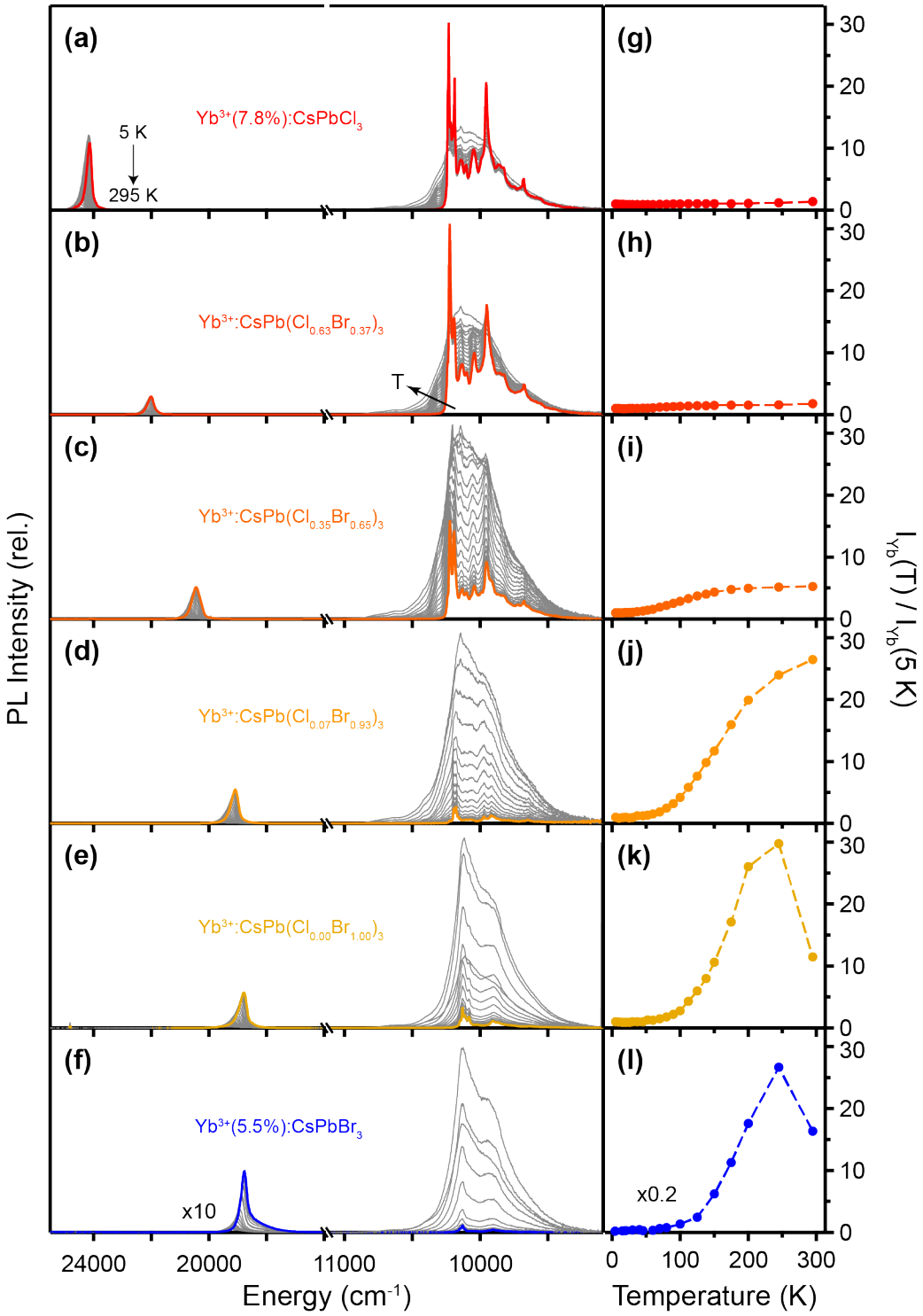

Figure 3.13. VTPL spectra of **(a)** 7.8% Yb^{3+}:$CsPbCl_3$, **(b-e)** anion-exchanged 7.8% Yb^{3+}:$CsPb(Cl_{1-x}Br_x)_3$, and **(f)** 5.5% Yb^{3+}:$CsPbBr_3$ NCs from 5 (colored) to 295 K. **(g-l)**

Integrated Yb^{3+} PL intensity at each temperature point relative to 5 K ($I_{Yb}(T)/I_{Yb}(5\ K)$) is plotted as a function of temperature for each sample from (a-f). All measurements used CW excitation at λ_{ex} = 375 nm (26700 cm^{-1}).

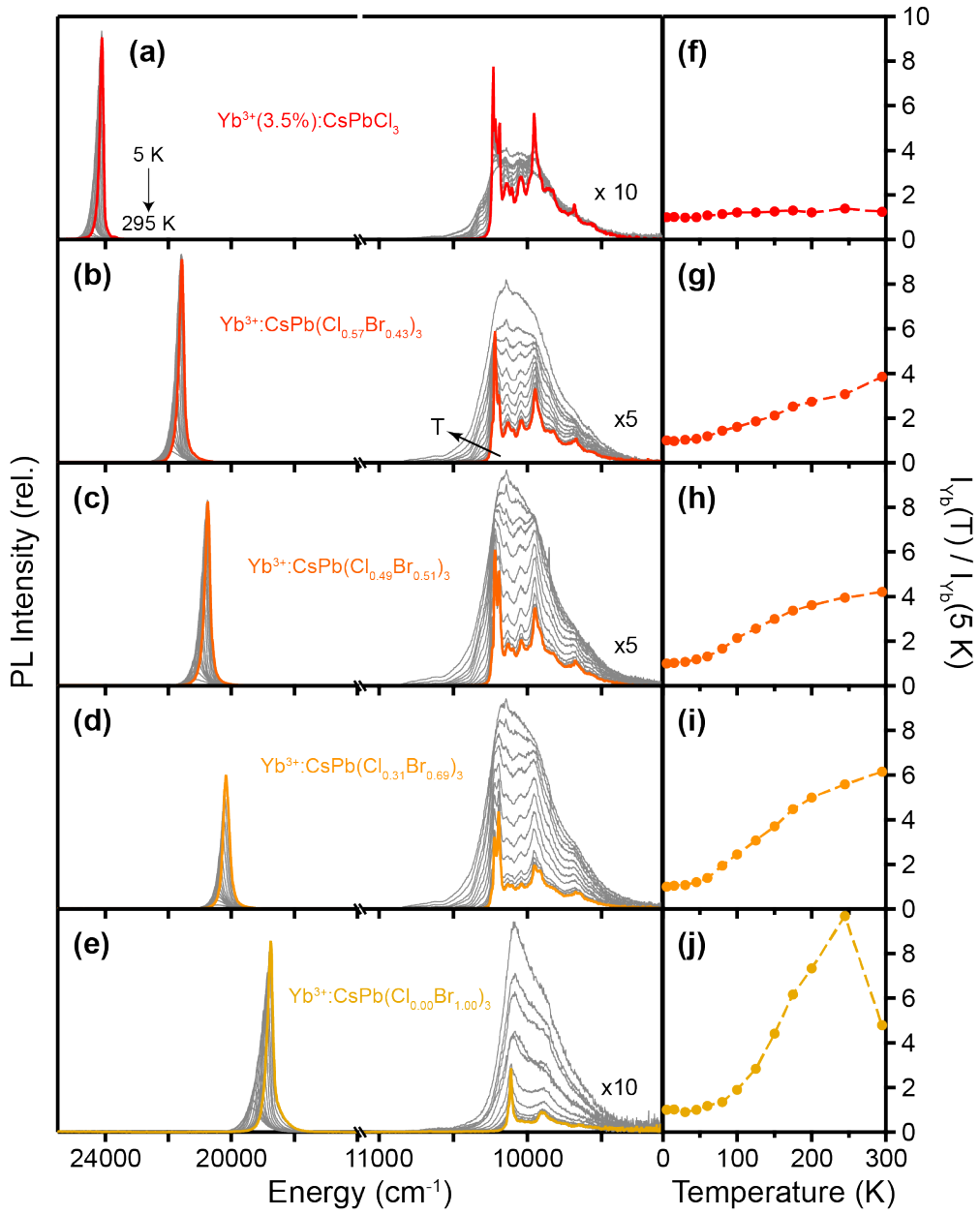

Figure 3.14. VTPL spectra of **(a)** 3.5% Yb^{3+}:$CsPbCl_3$, **(b-d)** anion-exchanged 3.5% Yb^{3+}:$CsPb(Cl_{1-x}Br_x)_3$. **(e-h)** Integrated Yb^{3+} PL intensity at each temperature point relative to 5 K ($I_{Yb}(T)/I_{Yb}(5\ K)$) is plotted as a function of temperature for each sample from (a-f). All measurements used CW excitation at λ_{ex} = 375 nm (26700 cm^{-1}).

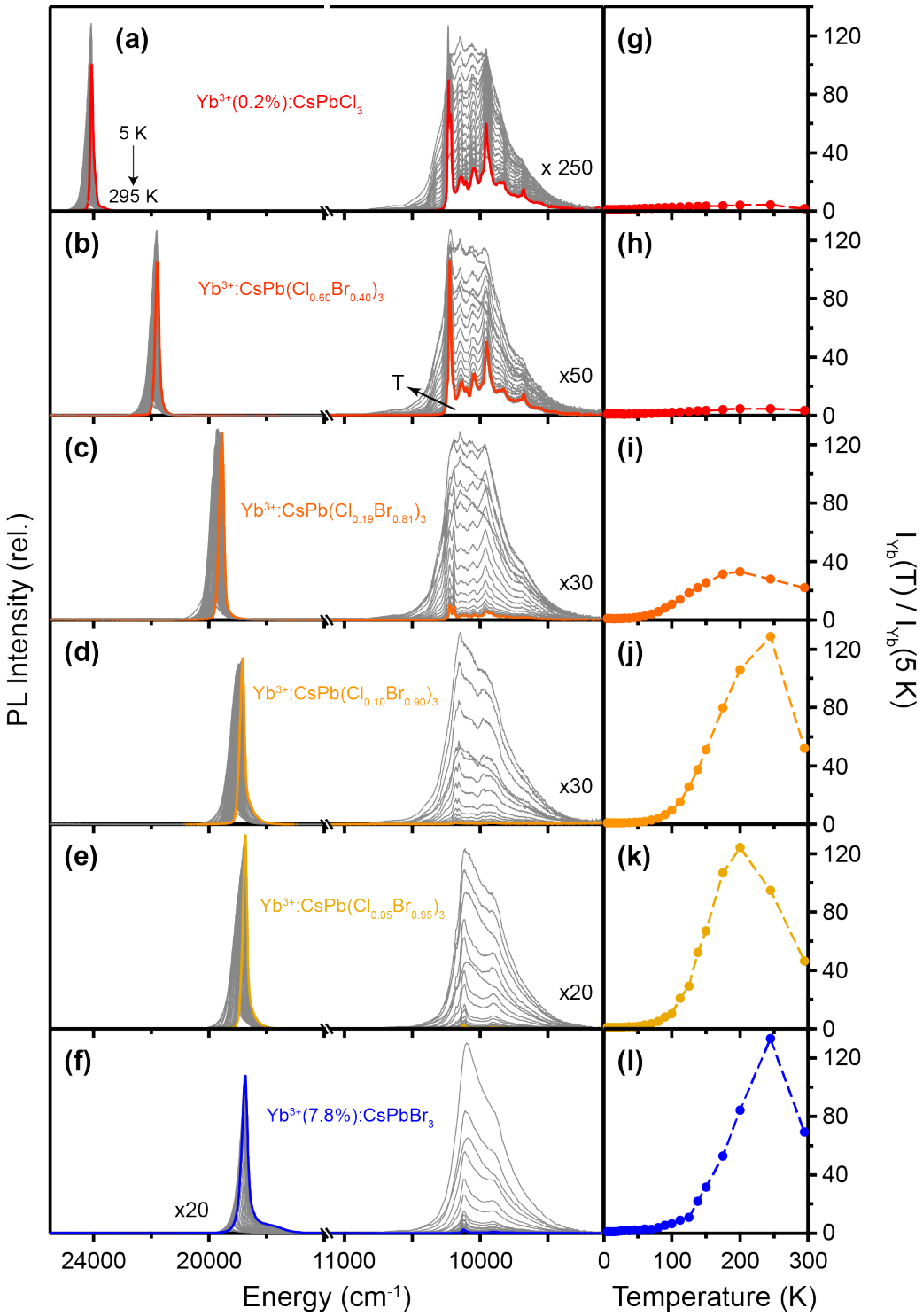

Figure 3.15. VTPL spectra of **(a)** 0.2% Yb^{3+}:$CsPbCl_3$, **(b-e)** anion-exchanged 0.2% Yb^{3+}:$CsPb(Cl_{1-x}Br_x)_3$, and **(f)** 7.8% Yb^{3+}:$CsPbBr_3$ NCs from 5 (colored) to 295 K. **(g-l)** Integrated Yb^{3+} PL intensity at each temperature point relative to 5 K ($I_{Yb}(T)/I_{Yb}(5\ K)$) is plotted as a function of temperature for each sample from (a-f). All measurements used CW excitation at $\lambda_{ex} = 375$ nm (26700 cm^{-1}). Note: panels a, c, f, g, i, l also shown in Figure 3.1.

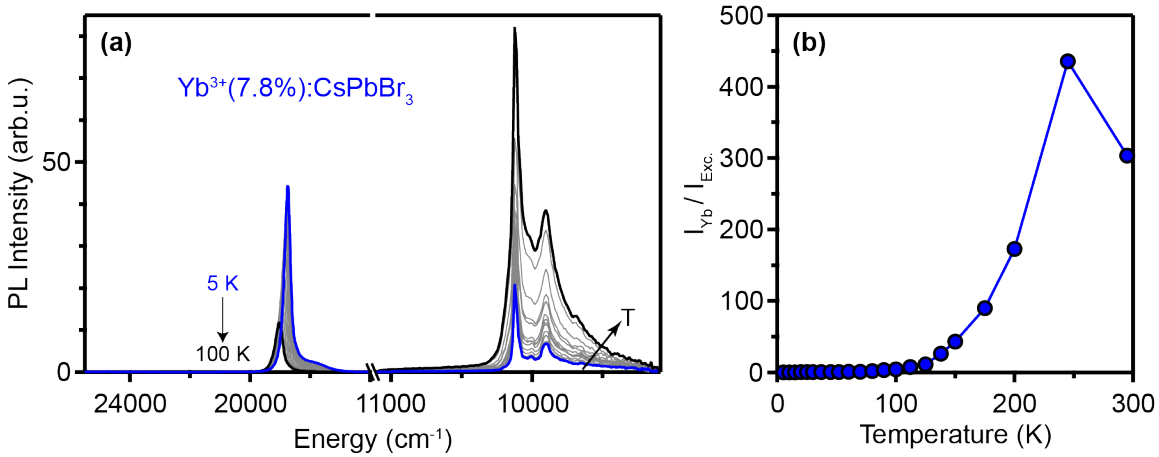

Figure 3.16. (a) VTPL spectra of 7.8% Yb^{3+}:$CsPbBr_3$ NCs from 5 (blue) to 100 K (black). **(b)** Integrated Yb^{3+} PL intensity taken from Figure 3.15 at each temperature point relative to integrated excitonic PL intensity (I_{Yb}/I_{Exc}), plotted as a function of temperature. CW excitation at λ_{ex} = 375 nm (26700 cm^{-1}).

Variable-temperature photoluminescence data for Yb^{3+}:$CsPb(Cl_{1-x}Br_x)_3$ nanocrystal powders

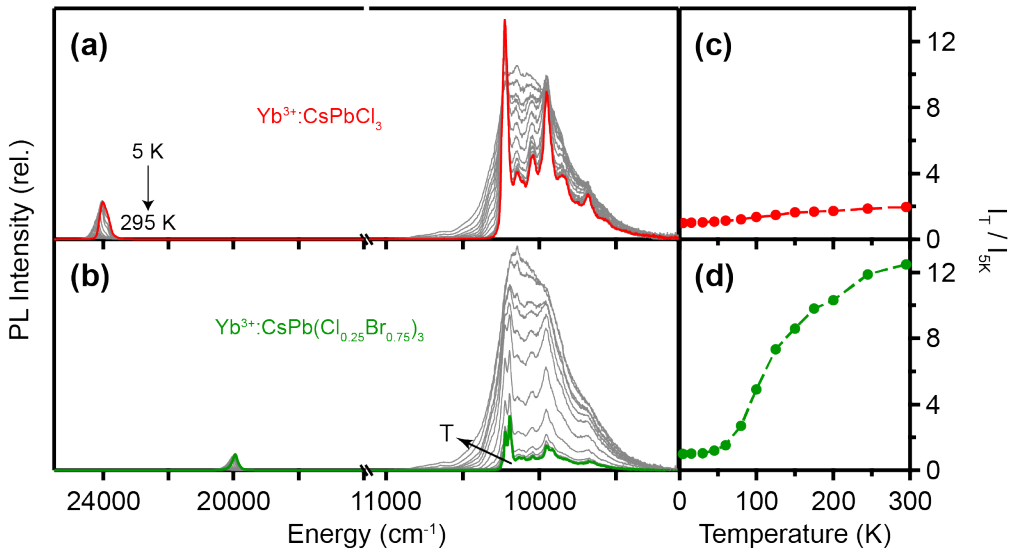

Figure 3.17. VTPL spectra of **(a)** Yb^{3+}:$CsPbCl_3$, **(b)** anion-exchanged Yb^{3+}:$CsPb(Cl_{0.25}Br_{0.75})_3$ NC powder from 5 (colored) to 295 K. **(c,d)** Integrated Yb^{3+} PL intensity at each temperature point relative to 5 K (I_T / I_{5K}) is, plotted as a function of temperature for each sample from (a, b). All measurements used CW excitation at λ_{ex} = 375 nm (26700 cm^{-1}).

Additional photoluminescence data and analysis

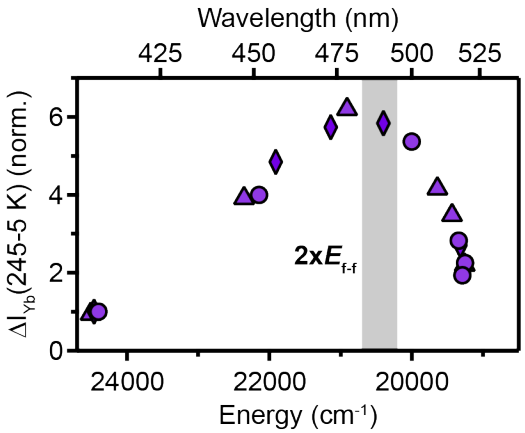

Figure 3.18. The change in integrated Yb^{3+} ($^2F_{5/2} \rightarrow {}^2F_{7/2}$) PL intensities from 5 to 245 K (ΔI_{Yb}(245-5 K)) plotted *vs* E_g at 245 K for (*i*) 0.2% Yb^{3+}:$CsPbCl_3$ and anion-exchanged Yb^{3+}:$CsPb(Cl_{1-x}Br_x)_3$ NCs, and 7.8% Yb^{3+}:$CsPbBr_3$ NCs taken from Figures 3.1 and 3.15 (circles), (*ii*) 3.5% Yb^{3+}:$CsPbCl_3$ and anion-exchanged Yb^{3+}:$CsPb(Cl_{1-x}Br_x)_3$ (Figure 3.14, diamonds), (*iii*) 7.8% Yb^{3+}:$CsPbCl_3$ and anion-exchanged Yb^{3+}:$CsPb(Cl_{1-x}Br_x)_3$ NCs, and 5.5% Yb^{3+}:$CsPbBr_3$ NCs from (Figure 3.13, triangles). The data for each anion-exchange series of NCs are normalized to the Yb^{3+}:$CsPbCl_3$ NC data point of that series, and data points for independently synthesized Yb^{3+}:$CsPbBr_3$ NCs are scaled to match the Yb^{3+}:$CsPb(Cl_{1-x}Br_x)_3$ NC trends in the limit of x = 1.00. The gray bar represents the proposed quantum-cutting energy threshold ($2\times E_{f\text{-}f}$).

Yb^{3+}-Yb^{3+} Simultaneous Pair Absorption Spectrum

The relationship between the absorption of single Yb^{3+} in the NIR and two Yb^{3+} in the visible regions was previously explained in $Cs_3Yb_2Br_9$ using the convolution theorem,[2] where $g(x) \times h(x)$ defines the convolution integral of two functions:[3]

$$g(x) \times h(x) = \int_0^x g(\tau)h(x-\tau)d\tau. \quad (3.5)$$

According to the theorem, the Fourier transform of the convolution integral (eq 3.5) is proportional to the product of Fourier transforms of each function.

$$\frac{1}{\sqrt{2\pi}}\int_{-\infty}^{\infty} g(x) \times h(x)e^{ixy}dx = \sqrt{2\pi}\, G(y)H(y) \quad (3.6)$$

In the case of quantum cutting, we can assume that Yb^{3+}-Yb^{3+} simultaneous pair absorption ($|{}^2F_{7/2}, {}^2F_{7/2}\rangle \rightarrow |{}^2F_{5/2}, {}^2F_{5/2}\rangle$) consists of two of the single Yb^{3+} NIR absorption, establishing that $f_{Yb}(y) = G(y) = H(y)$. Thus, we can simplify eq 3.6 to write eq 3.2.

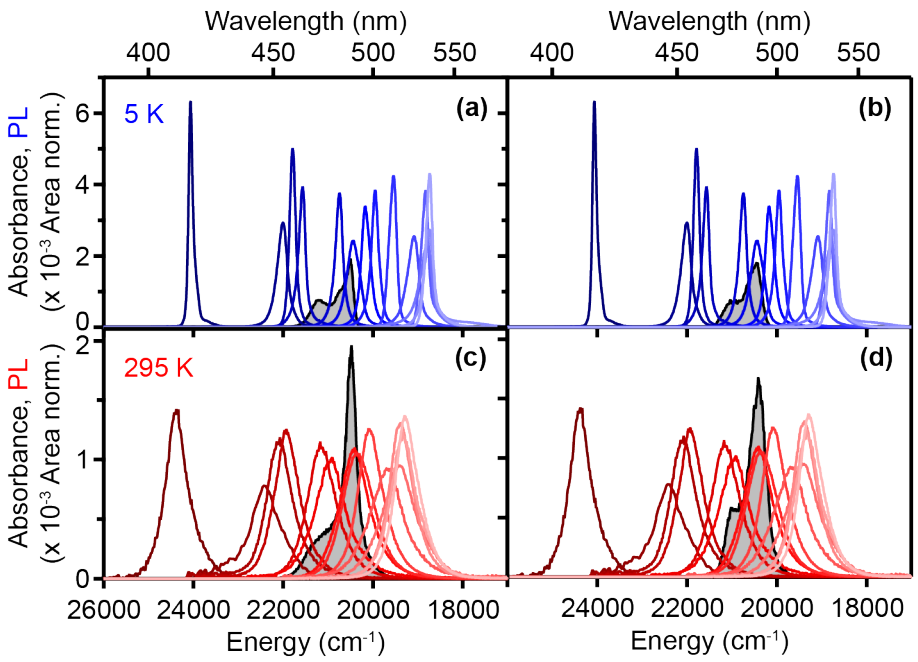

Figure 3.19. Calculated Yb^{3+}-Yb^{3+} simultaneous pair absorption spectrum ($|^2F_{7/2}, {}^2F_{7/2}\rangle \rightarrow |^2F_{5/2}, {}^2F_{5/2}\rangle$, filled gray) for Yb^{3+}:$CsPbCl_3$ NC powder at **(a)** 5 and **(c)** 295 K, compared with excitonic PL spectra of Yb^{3+}:$CsPb(Cl_{1-x}Br_x)_3$ NCs also at 5 (series of blue traces) and 295 K (series of red traces). Calculated Yb^{3+}-Yb^{3+} simultaneous pair absorption spectrum ($|^2F_{7/2}, {}^2F_{7/2}\rangle \rightarrow |^2F_{5/2}, {}^2F_{5/2}\rangle$, filled gray) for Yb^{3+}:$CsPb(Cl_{0.25}Br_{0.75})_3$ NC powder at **(b)** 5 and **(d)** 295 K, taken from Figures 3.3a and b, compared with excitonic PL spectra of Yb^{3+}:$CsPb(Cl_{1-x}Br_x)_3$ NCs also 5 (series of blue traces) and 295 K (series red traces). All the excitonic PL spectra and absorption spectra are area-normalized.

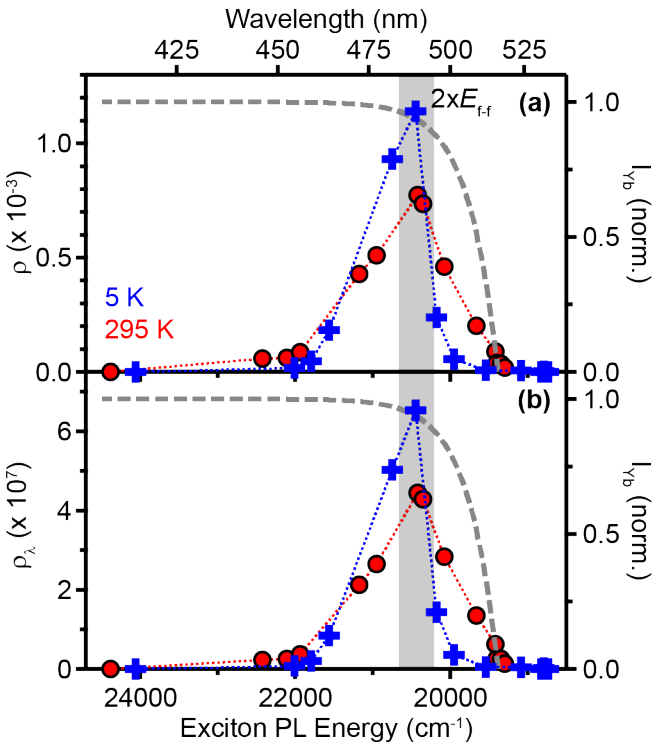

Figure 3.20. Values of spectral overlap (ρ) at 5 (blue) and 295 K (red) calculated using **(a)** eq 3.3 and **(b)** eq 3.7 with the Yb^{3+}-Yb^{3+} simultaneous pair absorption spectra ($|^2F_{7/2}, {}^2F_{7/2}\rangle \rightarrow |^2F_{5/2}, {}^2F_{5/2}\rangle$ for Yb^{3+}:$CsPbCl_3$ (when $E_g > 2\times E_{f\text{-}f}$) and Yb^{3+}:$CsPb(Cl_{0.25}Br_{0.75})_3$ (when $E_g \leq 2\times E_{f\text{-}f}$) NC powder and excitonic PL spectra taken from Figure 3.19.

Values of ρ in Figure 3.20a are calculated using eq 3.3, a spectral overlap integral for Dexter-type energy transfer, while values of ρ_λ in Figure 3.20b are calculated using eq 3.7, describing the spectral overlap for Förster-type energy transfer. Despite the mechanistic differences, spectral overlap calculated for both Dexter- and Förster-type energy transfer show the same dependence on perovskite E_g.

$$\rho_\lambda(\lambda) = \int_0^\infty f_{YbYb}(\lambda)\ g_{Exciton}(\lambda)\ \lambda^4\ d\lambda \tag{3.7}$$

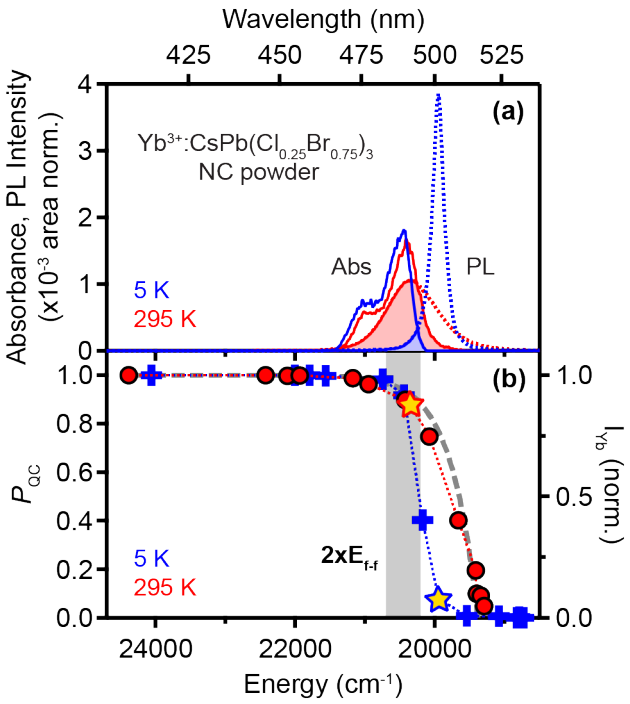

Figure 3.21. (a) Calculated Yb^{3+}-Yb^{3+} simultaneous-pair absorption ($|^2F_{7/2}, {}^2F_{7/2}\rangle \rightarrow |^2F_{5/2}, {}^2F_{5/2}\rangle$, solid traces, calculated) and excitonic PL (dotted traces) spectra of 5.1% Yb^{3+}:$CsPb(Cl_{0.25}Br_{0.75})_3$ NC powder measured at 5 (blue) and 295 K (red). The filled areas correspond to the donor/acceptor spectral overlap at 5 (blue) and 295 K (pink). **(b)** Values of the quantum-cutting energy-transfer probability (P_{QC}) at 5 (blue) and 295 K (red) calculated using eq 3.4 with the Yb^{3+}-Yb^{3+} simultaneous pair absorption spectra from panel (a) and excitonic PL spectra for Yb^{3+}:$CsPb(Cl_{1-x}Br_x)_3$ ($0.00 \leq x \leq 1.00$) from Figures 3.1 and 3.13-3.15, plotted as a function of E_g at 5 and 295 K, respectively. The gray dashed line is taken from Figure 3.2a. Stars denote P_{QC} values for the spectra shown in panel (a).

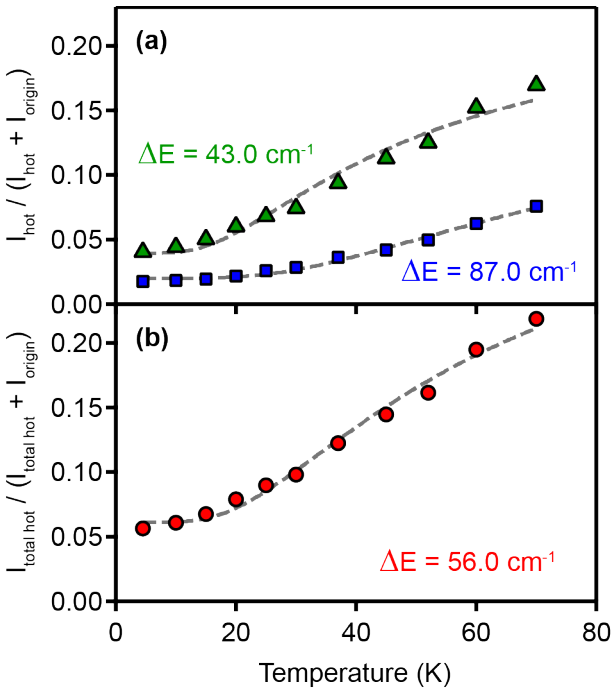

Figure 3.22. Temperature dependence of the relative integrated hot-band intensities for **(a)** the 10156 cm^{-1} (+43 cm^{-1}, green) and 10200 cm^{-1} (+87cm^{-1}, blue) peaks individually, and **(b)** the total hot-band intensity (+43 and +87 cm^{-1}, red). I_{origin} refers to the integrated intensity of the first electronic origin (10113 cm^{-1}). These data were collected from 5 to 70 K for the 7.8% Yb^{3+}:$CsPbBr_3$ NCs from Figure 3.5 of Section 3.3. Above ~70 K, integration of the hot-band intensities is unreliable. The gray dashed line in each figure plots the best fit to eq 3.8 using fixed values of ΔE = +43 and +87 cm^{-1} in panel (a), and a fitted value of ΔE = +56 cm^{-1} (reflecting the weighted average of +43 and +87 cm^{-1}) in panel (b). $\frac{I_i}{I_0}(0)$ accounts for the non-zero values of these ratios at T = 0 K (attributed to local heating, see Section 3.3). The fits yield prefactors of C = 0.35, 0.41, and 0.63, respectively.

$$\frac{I_{hot}}{I_{origin}+I_{hot}} = C\frac{e^{-\Delta E_{hot}/k_bT}}{1+e^{-\Delta E_{hot}/k_bT}} + \frac{I_i}{I_0}(0) \qquad (3.8)$$

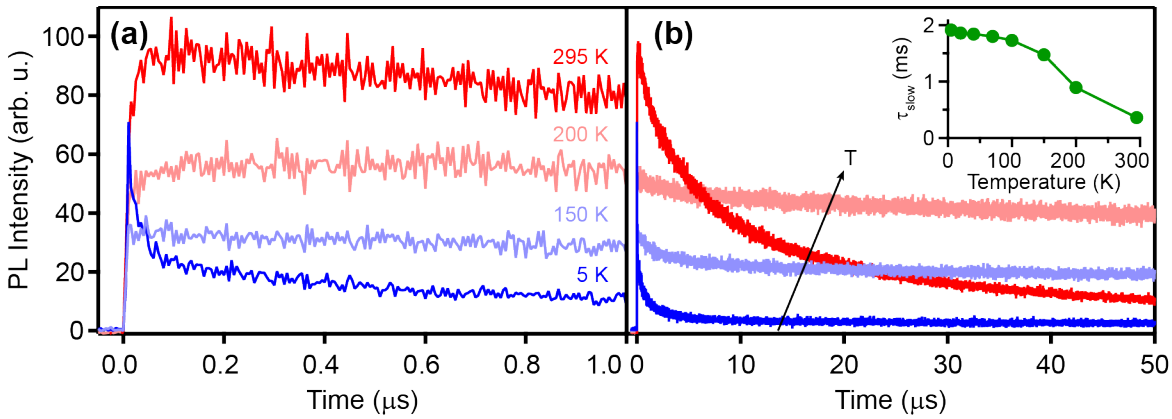

Figure 3.23. (a, b) Variable-temperature time-resolved photoluminescence traces measured for 7.8% Yb^{3+}:$CsPbBr_3$ NCs from 5 (blue) to 295 K (red). *Inset*: decay time of the slow component (green), plotted as a function of temperature. λ_{ex} = 355 nm (28200 cm^{-1}), λ_{em} = 989 nm (10110 cm^{-1}).

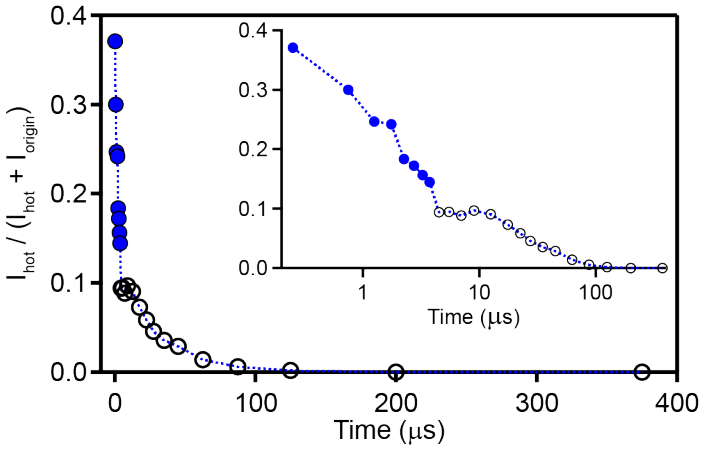

Figure 3.24. The ratios of the ~10156 cm^{-1} (+43 cm^{-1}) hot band peak the first electronic origin (10113 cm^{-1}) from the gated PL spectra measured for Yb^{3+}:$CsPbBr_3$ NCs at 5 K, plotted as a function of delay time from 250 ns to 375 μs. *Inset*: The ratio of 10156 cm^{-1} and 10113 cm^{-1} peak intensities (linear scale) *vs* the delay time plotted on a logarithmic scale. Each closed circle marks the center of the 500 ns integration period for the first 4 μs, and each open circle marks the center of the 1, 2, 5, 10, 25, 50, 100, and 250 μs integration period from 4 to 500 μs.

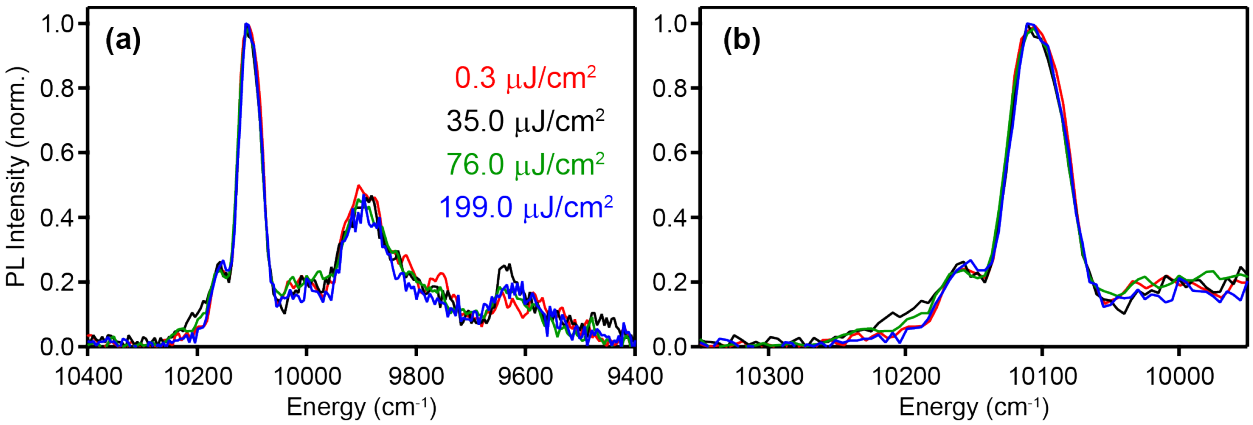

Figure 3.25. (a) Excitation-fluence dependence of gated Yb^{3+} PL measured for Yb^{3+}(7.8%):$CsPbBr_3$ NCs from Figure 3.6 at 5 K over the first 5 μs. **(b)** Expanded view of the highest energy feature with the hot band. Gated PL spectra in Figures 3.6 and 3.23 were measured an excitation fluence of 35.0 μJ/cm^2. The spectral bandwidth is ~ 11 cm^{-1}. λ_{ex} = 355 nm (28200 cm^{-1})

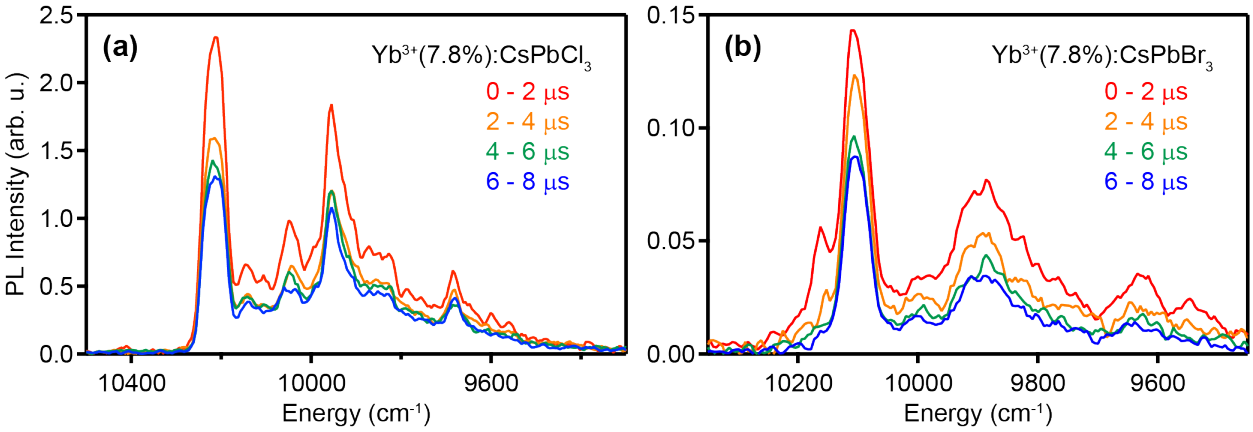

Figure 3.26. Gated PL spectra of **(a)** Yb^{3+}(7.8%):$CsPbCl_3$ NCs from Figure 3.13a and **(b)** Yb^{3+}(7.8%):$CsPbBr_3$ NCs from Figure 3.6 measured at 5 K over the first 8 μs of decay following a laser pulse (λ_{ex} = 355 nm (28200 cm^{-1})). Each gated spectrum was integrated over a 2 μs interval. The spectral bandwidth is ~11 cm^{-1}.

3.7.4 *References*

1. Linaburg, M. R.; McClure, E. T.; Majher, J. D.; Woodward, P. M. $Cs_{1-x}Rb_xPbCl_3$ and $Cs_{1-x}Rb_xPbBr_3$ Solid Solutions: Understanding Octahedral Tilting in Lead Halide Perovskites. *Chem. Mater.* **2017,** *29*, 3507-3514.
2. Hehlen, M. P.; Güdel, H. U. Optical Spectroscopy of the Dimer System $Cs_3Yb_2Br_9$. *J. Chem. Phys.* **1993,** *98*, 1768-1775.
3. Ovsyankin, V. V., CHAPTER 7 - Spectroscopy of Collective States and Cooperative Transitions in Disordered Rare-Earth Activated Solids. In *Modern Problems in Condensed Matter Sciences*, Kaplyanskii, A. A.; Macfarlane, R. M., Eds. Elsevier: 1987; Vol. 21, pp 343-480.

Chapter 4. Evolution of Yb^{3+} Speciation in Cl^-/Br^-- and Yb^{3+}/Gd^{3+}-Alloyed Quantum-Cutting Lead-Halide Perovskite Nanocrystals

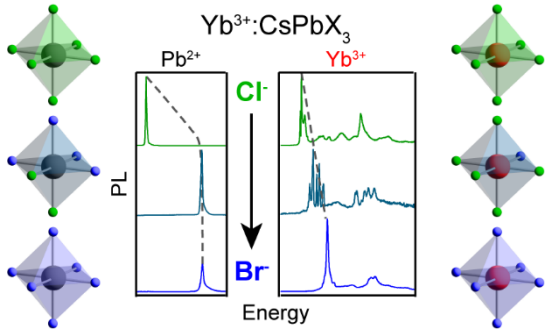

Reproduced with permission from Roh, J. Y. D.; Sommer, D. E.; Milstein, T. J.; Dunham, S. T.; Gamelin, D. R. *Submitted*. Copyright 2023 American Chemical Society.

4.1 Overview

Ytterbium doped all-inorganic lead-halide perovskites (Yb^{3+}:$CsPb(Cl_{1-x}Br_x)_3$) generate near-infrared photoluminescence quantum yields exceeding 100% by quantum cutting. Experimental and computational studies have suggested complex dopant speciation in these materials arising from the formation of lattice defects needed to compensate the excess charge of Yb^{3+} relative to Pb^{2+}, but the relationship between quantum cutting and such speciation is still poorly understood. Here, we use cryogenic photoluminescence spectroscopy and DFT-assisted kinetic Monte Carlo simulations to investigate changes in Yb^{3+} speciation induced by anion (Cl^- *vs* Br^-) and trivalent-dopant (Yb^{3+} *vs* Gd^{3+}) alloying in $CsPb(Cl_{1-x}Br_x)_3$ ($0.00 \leq x \leq 1.00$) perovskite nanocrystals. The experimental results reveal non-statistical distributions of Yb-Cl and Yb-Br bonds in Yb^{3+}:$CsPb(Cl_{1-x}Br_x)_3$ nanocrystals. Monte Carlo simulations reproduce the experimental trends well and predict thermodynamic favorability for Yb^{3+} dopants to retain Cl^- coordination even in the presence of high lattice Br^- concentrations. For a given lattice composition (e.g., $CsPbCl_3$), low-temperature photoluminescence spectra reveal that the relative populations of three dominant Yb^{3+} species change substantially with Gd^{3+} co-doping. These results further show that quantum cutting is largely insensitive to these differences in Yb^{3+} speciation, ruling out any "magic" configuration of Yb^{3+} ions and defects. These results are discussed in relation to the microscopic prerequisites for concerted sensitization of two Yb^{3+} ions during quantum cutting. Overall, these

findings highlight the mechanistic robustness of Yb^{3+}:$CsPb(Cl_{1-x}Br_x)_3$ quantum cutting in lead-halide perovskites, and provide deeper insight into the inner workings of this unique phenomenon.

4.2 Introduction

Ytterbium-doped all-inorganic lead-halide perovskite (Yb^{3+}:$CsPb(Cl_{1-x}Br_x)_3$) nanocrystals (NCs) have attracted broad research interest since the recent discovery of their remarkably high photoluminescence quantum yields (PLQYs), which can exceed 100% *via* quantum cutting.[1-4] This photomultiplication process converts the energy from an absorbed blue or ultraviolet (UV) photon to excite two Yb^{3+} dopant ions, which then re-emit that energy in the near-infrared (NIR) at a wavelength that matches the bandgap of silicon solar cells. Yb^{3+}:$CsPb(Cl_{1-x}Br_x)_3$ is unique among known quantum-cutting materials[1-7] in that it combines the strong and broadband absorption of a direct-gap semiconductor with the efficient luminescence of a lanthanide dopant, making it particularly attractive for solar harvesting and spectral conversion. Anion alloying within Yb^{3+}:$CsPb(Cl_{1-x}Br_x)_3$ ($0.00 \leq x \leq 1.00$) tunes the bandgap energy (E_g) and hence the portion of the solar spectrum absorbed by the perovskite, but efficiency drops rapidly when E_g is reduced below the thermodynamic threshold for energy-conserving quantum cutting ($2\times E_{f\text{-}f}$, at $x \approx 0.66$).[5, 8] These materials have already demonstrated substantial increases in power conversion efficiencies of silicon and CIGS solar cells,[2, 9] and offer the opportunity to overcome the Shockley-Queisser thermodynamic limit of single-junction photovoltaics.[10-13] To advance such applications, fundamental studies of these materials in the forms of colloidal NCs,[1, 4, 5, 9, 14-17] single crystals (SCs),[18] and solution-processed and vapor-deposited thin films[3, 19] remain essential.

Substitutional Yb^{3+} dopants require charge compensation, and experiment and computation both indicate that lead vacancies (V_{Pb}) constitute the primary defect allowing charge neutrality. Computational work shows similar thermodynamics for various dopant-bound or dissociated defect configurations in Yb^{3+}:$CsPbCl_3$.[20] At high Yb^{3+} doping, where PLQYs are greatest, charge-neutral defect clusters (Yb_{Pb}-V_{Pb}-Yb_{Pb}, both linear and bent) are predicted to be most prevalent. The identities and influence of these different species are still poorly understood. Multiple Yb^{3+} species are evident from low-temperature high-resolution PL spectra of Yb^{3+}:$CsPbCl_3$ SCs and NCs, although one primary Yb^{3+} species appears disproportionately active in quantum cutting.[18]

Here, we report results from two sets of experiments aimed at using compositional changes to reveal aspects of Yb^{3+} speciation and its influence on PL sensitization in Yb^{3+}:$CsPb(Cl_{1-x}Br_x)_3$

NCs. Specifically, high-resolution low-temperature PL spectra of Yb^{3+}:$CsPb(Cl_{1-x}Br_x)_3$ NCs have been measured as a function of anion alloying ($0.00 \leq x \leq 1.00$) and B-site cation alloying (replacing Yb^{3+} with Gd^{3+}) to observe the evolution of Yb^{3+} local environments in each compositional dimension. From the anion alloying experiments, the data reveal that Cl-to-Br anion exchange at Yb^{3+} lags behind that of the surrounding lattice, such that $[YbCl_6]^{3-}$ units remain prevalent even at $x \sim 0.50$. Computations reproduce the experimental trend well and show that this non-statistical local coordination of Yb^{3+} is thermodynamically favorable. From the B-site alloying experiments, the data show that introduction of Gd^{3+} co-dopants changes the relative probabilities of different Yb^{3+} species but that quantum cutting is largely undisturbed by this change, even though the population of correlated Yb^{3+} dopant pairs is (statistically) diminished. These results shed light on the microscopic environments around Yb^{3+} dopants involved in quantum cutting in Yb^{3+}:$CsPb(Cl_{1-x}Br_x)_3$ nanocrystals, and they demonstrate a substantially richer diversity of active Yb^{3+} sites than previously recognized.

4.3 Results and Discussion

4.3.1 *Halide alloying*

General characterization. Yb^{3+}-doped $CsPbCl_3$ (x = 0.00) NCs were prepared as described previously.[4] Yb^{3+}-doped $CsPb(Cl_{1-x}Br_x)_3$ NCs were prepared by anion exchange from those Yb^{3+}:$CsPbCl_3$ NCs using trimethylsilyl-bromide (TMS-Br), following methods described previously.[5, 21-23] Yb^{3+}-doped $CsPbBr_3$ NCs (x = 1.00) were synthesized directly by hot injection of TMS-Br. Figure 4.1 summarizes representative structural data for a series of Yb^{3+}-doped $CsPb(Cl_{1-x}Br_x)_3$ NCs ranging from $0.00 \leq x \leq 1.00$. The transmission electron microscopy (TEM) image of 7.8% Yb^{3+}:$CsPbCl_3$ NCs in Figure 4.1a shows an average edge length of 13.9 ± 2.5 nm, consistent with previous findings.[4, 5, 18, 24] The average edge length of the 7.8% Yb^{3+}:$CsPb(Cl_{0.07}Br_{0.93})_3$ NCs in Figure 4.1b is slightly larger (15.3 ± 2.6 nm), which reflects the increased ionic radius of Br^-.[5] Figure 4.1c shows a TEM image of 5.5% Yb^{3+}:$CsPbBr_3$ NCs, whose average edge length is 17.4 ± 2.3 nm. Figure 4.1d shows powder x-ray diffraction (pXRD) patterns collected from 0.2% Yb^{3+}:$CsPbCl_3$ and 0.2% Yb^{3+}:$CsPb(Cl_{0.10}Br_{0.90})_3$ NCs, as well as from 7.8% Yb^{3+}:$CsPbBr_3$ NCs. The data show intensities consistent with the reference perovskite structure without any detectible impurities. As reported previously, doping trivalent rare-earth ions (RE^{3+})

into $CsPbX_3$ NCs does not cause observable shifts of the XRD reflections or any obvious changes to the NC morphology.[3-5, 14, 18, 19, 24]

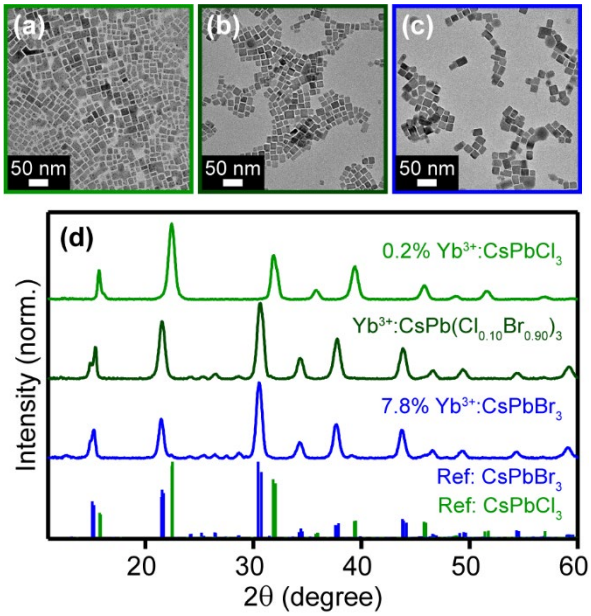

Figure 4.1. Representative TEM images and powder XRD data for Yb^{3+}:$CsPb(Cl_{1-x}Br_x)_3$ NCs. **(a)** 7.8% Yb^{3+}:$CsPbCl_3$ NCs, **(b)** Yb^{3+}:$CsPb(Cl_{0.07}Br_{0.93})_3$ NCs made by anion exchange from the NCs of panel (a), and **(c)** 5.5% Yb^{3+}:$CsPbBr_3$ NCs made by direct synthesis. **(d)** Powder XRD data collected for (light green, top) 0.2% Yb^{3+}:$CsPbCl_3$ NCs, (dark green, middle) Yb^{3+}:$CsPb(Cl_{0.10}Br_{0.90})_3$ NCs made by anion exchange from the NCs of panel (d), and (blue, bottom) 7.8% Yb^{3+}:$CsPbBr_3$ NCs made by direct synthesis. Reference indices for the cubic high-temperature forms of $CsPbCl_3$ (green) and $CsPbBr_3$ (blue) are shown at the bottom.[25] Although $CsPbCl_3$ and $CsPbBr_3$ adopt the orthorhombic structure (space group *Pnma*) at room temperature, the resulting peak splittings are not detectible on the scale plotted here.

The effects of anion exchange on Yb^{3+} speciation and spectroscopy. Figure 4.2 shows steady-state PL spectra of a series of Yb^{3+}:$CsPb(Cl_{1-x}Br_x)_3$ ($0.00 \leq x \leq 1.00$) NCs, all measured at 5 K. Due to the very low dopant concentrations used in all but the $CsPbBr_3$ NCs, the excitonic PL intensities are large and have therefore been scaled for clarity. Looking first at the endpoints (x = 0.00 and 1.00), the Yb^{3+} PL spectra in $CsPbCl_3$ and $CsPbBr_3$ lattices show their most intense features at 10233 and 10113 cm^{-1}, respectively, attributed to the first electronic origin ($\Gamma_8 \rightarrow \Gamma_6$, split by low symmetry) of the characteristic set of $^2F_{5/2} \rightarrow {}^2F_{7/2}$ transitions. These intense peaks are followed by sets of broader and less intense peaks in each sample, attributable to a combination of electronic origins and vibronic side-bands. These spectra and their dependence on the halide are

generally similar to those seen in other chloride and bromide lattices,[26] and are consistent with pseudo-octahedral $[YbX_6]^{3-}$. These endpoint spectra thus define the coordination limits of $[YbCl_6]^{3-}$ and $[YbBr_6]^{3-}$. As described previously[18] for Yb^{3+}:$CsPbCl_3$ and expanded upon below, multiple Yb^{3+} species are observable in each limiting composition, attributed to electrostatic variations in the second (or beyond) coordination spheres.

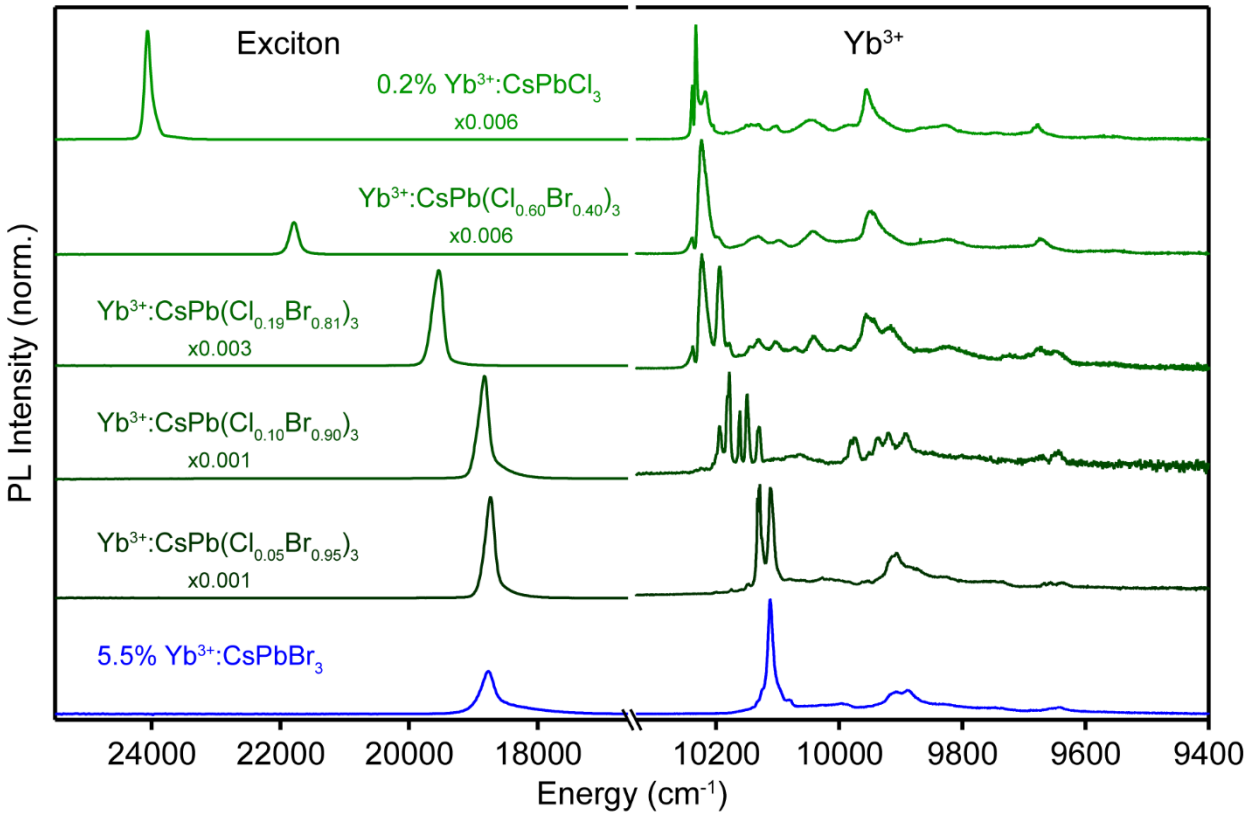

Figure 4.2. 5 K PL spectra of a series of Yb^{3+}:$CsPb(Cl_{1-x}Br_x)_3$ NCs with different Br^- mole fractions: (light green) 0.2% Yb^{3+}:$CsPbCl_3$, (dark green) 0.2% Yb^{3+}:$CsPb(Cl_{1-x}Br_x)_3$ prepared from the same Yb^{3+}:$CsPbCl_3$ NCs by partial anion exchange, and (blue) 5.5% Yb^{3+}:$CsPbBr_3$ NCs prepared by direct synthesis. λ_{ex} = 375 nm (26700 cm^{-1}). From top to bottom, the exciton region has been multiplied by 0.006, 0.006, 0.003, 0.001, 0.001, and 1.0 to display it on the same scale as the Yb^{3+} PL.

With increasing x, the excitonic PL gradually and uniformly shifts to lower energy, reflecting the well-known decrease in E_g of the perovskite. Starting from $CsPbCl_3$, small amounts of Br^- appear to have little effect on the Yb^{3+} PL energy, although the spectrum broadens somewhat. The Yb^{3+} PL energy begins to shift substantially only at relatively large values of x. In this regime, the redshift is accompanied by the appearance of multiple new sharp peaks in the first electronic origin

region (~10240 – 10100 cm^{-1}). These changes are also reflected in the energies and widths of the less-intense peaks to lower energy, but those are not as well resolved. The observation of multiple resolved peaks around the first electronic origin suggests multiple Yb^{3+} species with mixed Cl/Br coordination, *i.e.*, distributions of $[Yb(Cl_{6-z}Br_z)]^{3-}$ ($0 \leq z \leq 6$) populations at intermediate values of x, as expected.

The observations in Figure 4.2 are summarized in Figure 4.3, which plots the peak energies of the excitonic PL and the intensity-weighted average energies of the first Yb^{3+} $^2F_{7/2} \rightarrow {}^2F_{5/2}$ electronic origin (~10240 – 10100 cm^{-1}) *vs* x. The excitonic PL energy decreases linearly with increasing x, as expected.[4, 27, 28] In contrast, the Yb^{3+} PL energy shows little change until $x > \sim 0.5$, at which point it rapidly decreases to approach the energy of Yb^{3+}:$CsPbBr_3$. The divergence between these two curves suggests that the local halide coordination around Yb^{3+} is not the same as that of the rest of the lattice, *i.e.*, the Yb^{3+} coordination is non-statistical. To test whether this observation is reproducible, analogous 5 K PL data were collected for two more anion-exchange series (with $[Yb^{3+}] = 7.8\%$ and 3.5%), as well as for a sample of 7.8% Yb^{3+}:$CsPbBr_3$ NCs prepared by direct synthesis. The curve is highly reproducible, showing that this trend is independent of the specific Yb^{3+} concentration.

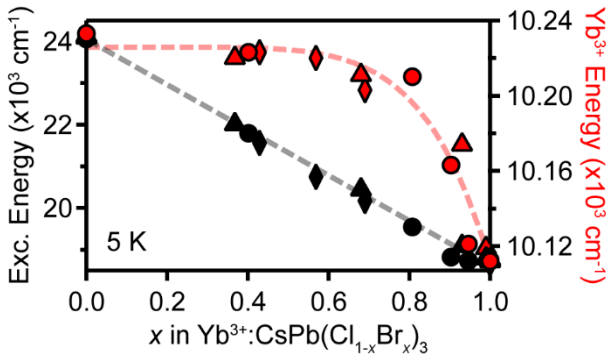

Figure 4.3. Dependence of the excitonic energies (black) and average Yb^{3+} first-electronic-origin energies (red) on x, taken from the 5 K PL spectra of various Yb^{3+}:$CsPb(Cl_{1-x}Br_x)_3$ NCs: (circles) the Yb^{3+}:$CsPb(Cl_{1-x}Br_x)_3$ NCs of Figure 4.2, (triangles) the 7.8% Yb^{3+}:$CsPb(Cl_{1-x}Br_x)_3$ NCs of Figure 4.12, (diamonds) the 3.5% Yb^{3+}:$CsPb(Cl_{1-x}Br_x)_3$ NCs of Figure 4.11. Values of x for each sample were determined from pXRD data using Vegard's law. The dashed lines are guides to the eye.

Anions are highly mobile in $CsPbX_3$ NCs, as evidenced by their facile post-synthetic anion exchange.[5, 21, 22, 24, 29-32] We therefore hypothesize that the non-statistical anion distributions *within*

these Yb^{3+}:$CsPb(Cl_{1-x}Br_x)_3$ NCs reflect lattice thermodynamics, not kinetics. To understand this observation, it is helpful to compare the relevant bond dissociation energies: 385 kJ/mol for Yb-Cl ($YbCl_3$) and 322 kJ/mol for Yb-Br ($YbBr_3$), compared to 304 kJ/mol for Pb-Cl ($PbCl_2$), 260 kJ/mol for Pb-Br ($PbBr_2$).[33] From these numbers, a driving force for retaining Yb-Cl bonds in Yb^{3+}:$CsPb(Cl_{1-x}Br_x)_3$ of ~20 kJ/mol per Cl^- anion may be anticipated. It is further possible that Yb^{3+} itself may migrate to minimize the total energy, including from lattice strain. This latter scenario was observed[21] to cause spontaneous aggregation of $[MnCl_6]^{4-}$ units with increasing x in Mn^{2+}-doped $CsPb(Cl_{1-x}Br_x)_3$ NCs.

To explore the thermodynamics of anion alloying in these doped NCs further, we employed canonical Monte Carlo simulations. Calculations were performed on model systems of 5% Yb^{3+}:$CsPb(Cl_{1-x}Br_x)_3$ at room temperature (see Section 4.5). Figure 4.4a plots the equilibrium populations of all possible $[YbCl_{6-z}Br_z]^{3-}$ species calculated for x = 0.15, 0.50, and 0.85 (see Figure 4.17 for more compositions). At x = 0.15, nearly all Yb^{3+} ions have exclusively Cl^- coordination (z = 0). Increasing x shifts the species distribution to higher z, but at x = 0.50, the distribution remains highly skewed toward small z. Not until x = 0.85 is the distribution centered roughly at z = 3, and even when x = 0.95, ~20% of the halides surrounding Yb^{3+} are still Cl^- ions (Figure 4.17). These results show that the halide distribution in the first coordination sphere of Yb^{3+} is highly non-statistical, with Cl^- strongly favored. Figure 4.4b replots the results from Figure 4.4a to show the average number of Br^- ions (z_{avg}) bound to Yb^{3+} as a function if x. Overlaid with these data are the Yb^{3+} PL energies from Figure 4.3, scaled to highlight the similarity of the two curves. For both the experimental and computed results, the data show that most anion substitution at Yb^{3+} occurs only at large x, *i.e.*, Yb^{3+} ions preferentially bind Cl^- in Yb^{3+}:$CsPb(Cl_{1-x}Br_x)_3$ (x > 1.00).

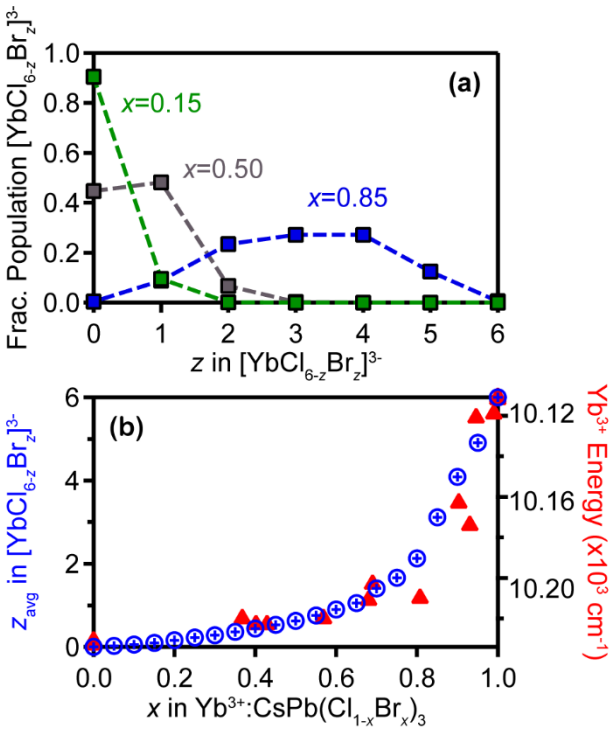

Figure 4.4. (a) Room-temperature Monte Carlo simulation of the fractional population of $[YbCl_{6-z}Br_z]^{3-}$ ($0 \leq z \leq 6$) species in a 5.0% Yb^{3+}:$CsPb(Cl_{1-x}Br_x)_3$ single crystal at $x = 0.15$ (green), 0.50 (gray), and 0.85 (blue), plotted as a function of z. **(b)** The average value of z (z_{avg}) in 5.0% Yb^{3+}:$CsPb(Cl_{1-x}Br_x)_3$, plotted against x. The red data points show the average Yb^{3+} first-electronic-origin energies from Figure 4.3 for comparison.

To probe for structural reorganization during anion exchange, we compared the 5 K Yb^{3+} PL of Yb^{3+}:$CsPbCl_3$ measured before anion exchange with that measured after complete anion exchange followed by complete *reverse* anion exchange: 7.8% Yb^{3+}:$CsPbCl_3$ NCs were first converted to Yb^{3+}:$CsPbBr_3$ NCs, then Cl^- anions were reintroduced to convert them back to Yb^{3+}:$CsPbCl_3$ NCs. Figure 4.5a plots the room-temperature PL spectra for these two samples collected at the same photoexcitation rate, and Figure 4.5b plots the 5 K PL spectra of the same samples normalized to the peak maximum at ~9960 cm^{-1}. The room-temperature spectra are very similar, but the 5 K spectra show marked differences in the intensities of the minority species emitting at energies just below the first intense electronic origin (~10190 - 10230 cm^{-1}), indicating lattice restructuring during anion exchange. Three main features in this region can be identified and attributed to the first electronic origins of three different species, *A*, *B*, and *C*. The as-prepared Yb^{3+}:$CsPbCl_3$ NCs show a prominent feature from species *C* that disappears following the anion-exchange cycle. Interestingly, this substantial change in Yb^{3+} speciation has little effect on the

relative room-temperature Yb^{3+} PLQY, which actually increases by ~10% following the anion exchange/reverse-anion-exchange cycle (Figure 4.5a), similar to our previous observations.[4]

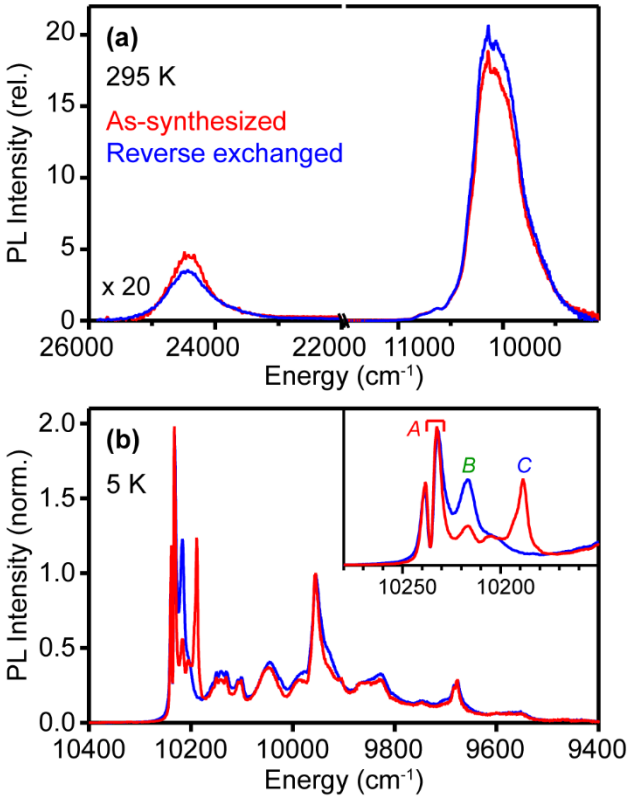

Figure 4.5. (a) Room-temperature PL spectra of 7.8% Yb^{3+}:$CsPbCl_3$ NCs before (red) and after (blue) a full Cl → Br → Cl anion exchange/reverse-anion-exchange cycle (x = 0.00 → ~1.00 → ~0.00). Sample photoexcitation rates are equal, such that intensity changes correspond to changes in relative PL quantum yield. **(b)** 5 K PL spectra of the same NCs, normalized to the peak maximum at ~9960 cm^{-1}. *Inset*: Expansion around the Yb^{3+} first electronic origin, showing peaks from multiple Yb^{3+} species. CW excitation at λ_{ex} = 375 nm (26700 cm^{-1}).

4.3.2 *B-site cation alloying*

General characterization. Previous studies have reported improved quantum cutting in Yb^{3+}:$CsPb(Cl_{1-x}Br_x)_3$ samples co-doped with additional RE^{3+} ions, attributed to reduction of non-radiative losses.[34] To explore the effects of RE^{3+} co-doping on Yb^{3+} speciation and quantum cutting, we investigated the properties of Yb^{3+}/Gd^{3+}-co-doped $CsPbCl_3$ NCs. Previous work

showed that Gd^{3+} and other spectroscopically innocent RE^{3+} dopants universally generate a similar near-band-edge defect state[4, 28] attributed to charge-compensating V_{Pb} defects. Co-doping with Gd^{3+} is thus expected to introduce additional V_{Pb} and, in the case of low Yb^{3+} doping and high Gd^{3+} doping, the occurrence of correlated $[Yb_{Pb}\text{-}V_{Pb}\text{-}Yb_{Pb}]^0$ pairs should be largely suppressed. B-site alloying thus provides the opportunity to probe the importance of co-localization of two Yb^{3+} ions on PL sensitization.

Yb^{3+}/Gd^{3+} co-doped $CsPbCl_3$ NCs were prepared by simply adding $Gd(OAc)_3$ in addition to the $Yb(OAc)_3$ precursor at the desired ratio (see Section 4.5). Figure 4.6a shows pXRD data collected for 5.4% Yb^{3+}/2.5% Gd^{3+}:$CsPbCl_3$ and 6.8% Gd^{3+}:$CsPbCl_3$ NCs. These data resemble those of other RE^{3+}-doped $CsPbCl_3$ NCs.[4, 18, 28, 35] As with Yb^{3+} doping, Gd^{3+} doping does not cause significant shifts in the XRD peak positions relative to $CsPbCl_3$. TEM images of the Yb^{3+}/Gd^{3+}:$CsPbCl_3$ and Gd^{3+}:$CsPbCl_3$ NCs from Figure 4.6a show average edge lengths of 16.9 ± 3.8 nm (Figure 4.6b) and 12.8 ± 2.6 nm (Figure 4.6c), respectively, which are typical of this synthesis.[35, 36]

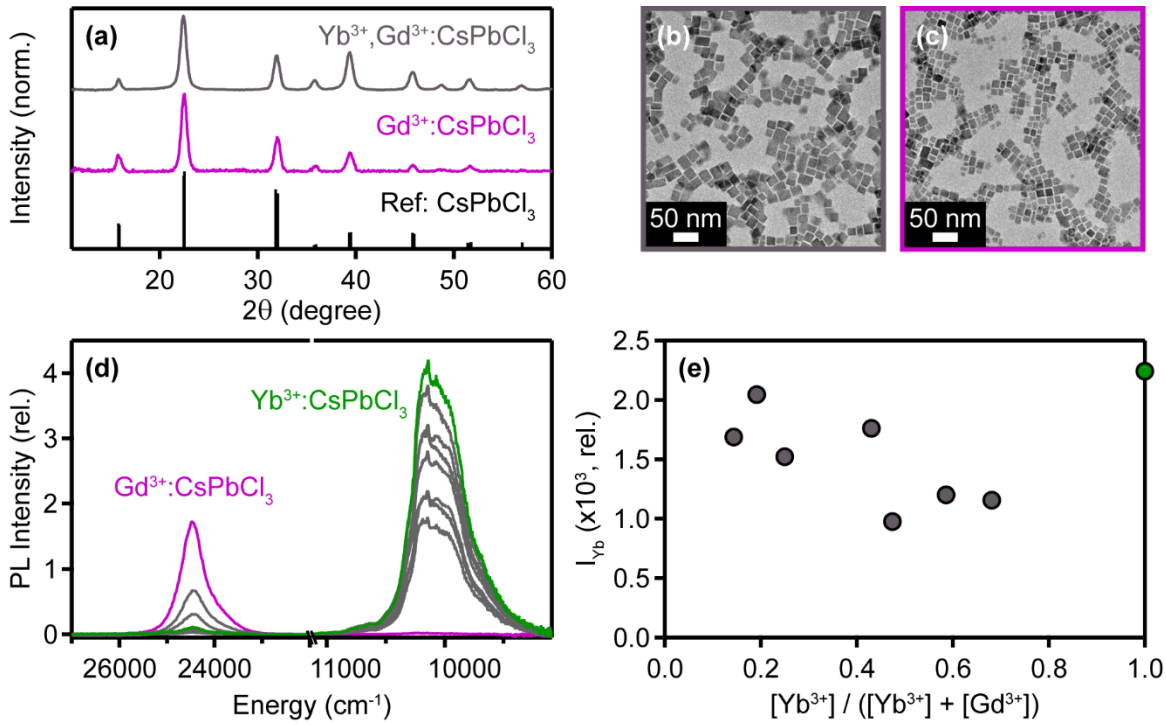

Figure 4.6. (a) pXRD data for (gray) 5.4% Yb^{3+}/2.5% Gd^{3+}:$CsPbCl_3$ and (magenta) 6.8% Gd^{3+}:$CsPbCl_3$ NCs. Reference indices (black) are shown for the cubic high-temperature form of $CsPbCl_3$.[25] Representative TEM images of the same **(b)** Yb^{3+}/Gd^{3+}:$CsPbCl_3$ and **(c)** Gd^{3+}:$CsPbCl_3$ NCs. **(d)** Room-temperature PL spectra of (green) 6.6% Yb^{3+}:$CsPbCl_3$

NCs, (gray) various 0.9-6.9% Yb^{3+}/2.5-7.7% Gd^{3+}:$CsPbCl_3$ NCs, and (magenta) 6.8% Gd^{3+}:$CsPbCl_3$ NCs. **(e)** Integrated Yb^{3+} ($^2F_{5/2} \rightarrow {}^2F_{7/2}$) PL intensities for the Yb^{3+}:$CsPbCl_3$ (green) and Yb^{3+}/Gd^{3+}:$CsPbCl_3$ (gray) NCs from panel (a), plotted *vs* $[Yb^{3+}]/([Yb^{3+}] + [Gd^{3+}])$. All measurements used CW excitation at λ_{ex} = 375 nm (26700 cm^{-1}), using a constant per-NC excitation rate of 100 s^{-1}.

Figure 4.6d plots room-temperature PL spectra of the 6.8% Gd^{3+}:$CsPbCl_3$ NCs from Figure 4.6a, as well as of several other Yb^{3+}/Gd^{3+}:$CsPbCl_3$ NCs with various RE^{3+} concentration levels (0.9-6.9% Yb^{3+}/2.5-7.7% Gd^{3+}). The Gd^{3+}:$CsPbCl_3$ NCs show near-band-edge PL and no NIR luminescence, while the Yb^{3+}-doped $CsPbCl_3$ NCs show strong $^2F_{5/2} \rightarrow {}^2F_{7/2}$ PL in the NIR and weak excitonic PL. When compared to Yb^{3+}:$CsPbCl_3$ NCs with similar Yb^{3+} concentrations, co-doped samples show more excitonic PL and comparable Yb^{3+} PL intensities. Figure 4.6e summarizes the results of Figure 4.6d by plotting the integrated Yb^{3+} PL intensity *vs* $[Yb^{3+}]/([Yb^{3+}] + [Gd^{3+}])$. Despite the large differences in B-site composition, Yb^{3+} sensitization remains constant within a factor of 2 across this series. Most notably, samples with low and high $[Yb^{3+}]$ show similar NIR PL intensities, representing a departure from the usual trend of increasing NIR PL with increasing $[Yb^{3+}]$.[4]

The effects of B-site cation alloying on Yb^{3+} speciation and spectroscopy. To explore the above conclusions in more detail, high-resolution PL measurements were used to probe whether Gd^{3+} co-doping indeed causes any noticeable change in Yb^{3+} speciation. Figure 4.7a shows 5 K steady-state PL spectra measured for the 6.6% Yb^{3+}:$CsPbCl_3$ and 6.8% Gd^{3+}:$CsPbCl_3$ NCs from Figure 4.6, as well as for two Yb^{3+}/Gd^{3+}:$CsPbCl_3$ NC samples with similar total B-site dopant concentrations. The Gd^{3+}:$CsPbCl_3$ NCs show excitonic PL accompanied by the characteristic shallow-defect band ~400 cm^{-1} lower in energy, as detailed previously.[28] The intensities of these features decrease as $[Yb^{3+}]/([Yb^{3+}] + [Gd^{3+}])$ increases until ultimately the shallow-defect emission is not observed in Yb^{3+}:$CsPbCl_3$ NCs. These observations are consistent with depletion of the shallow trap state *via* energy transfer to Yb^{3+}.

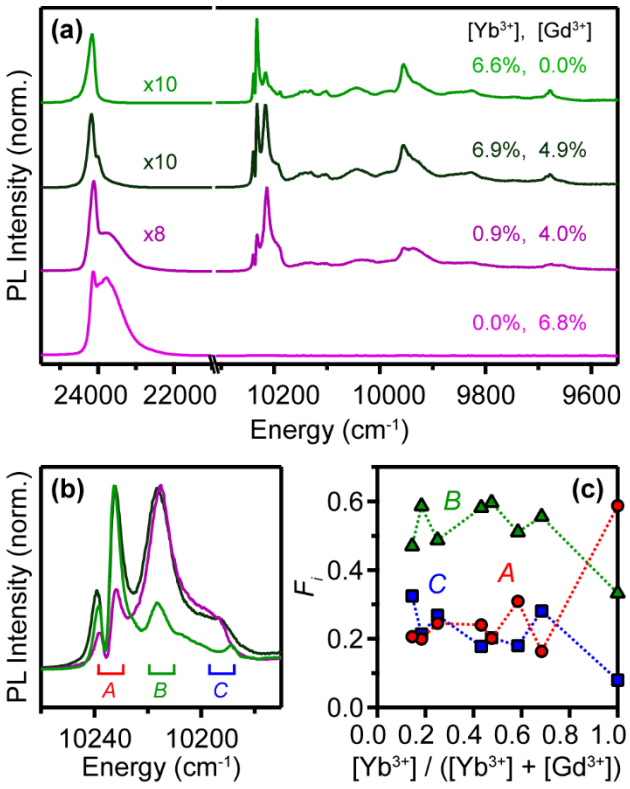

Figure 4.7. (a) 5 K PL spectra of the NCs in Figure 4.6: (light green) 6.6% Yb^{3+}:$CsPbCl_3$, (dark green) 6.9% Yb^{3+}/4.9% Gd^{3+}:$CsPbCl_3$, (purple) 0.9% Yb^{3+}/4.0% Gd^{3+}:$CsPbCl_3$, (magenta) 6.8% Gd^{3+}:$CsPbCl_3$. λ_{ex} = 375 nm (26700 cm^{-1}). From top to bottom, the exciton region has been multiplied by 10, 10, 8, and 1 to display it on the same scale as the Yb^{3+} PL. **(b)** Expanded view of the Yb^{3+} first electronic origin region from panel (a), showing peaks associated with three Yb^{3+} species: *A*, *B*, and *C*. **(c)** The fractional integrated intensities (F_i) of species *A* (red), *B* (green), and *C* (blue) observed in the spectra of various Yb^{3+}/Gd^{3+}:$CsPbCl_3$ NCs, taken from the 5 K PL spectra of panel (a) and Figure 4.13, plotted *vs* [Yb^{3+}]/([Yb^{3+}] + [Gd^{3+}]).

Although the Yb^{3+} PL spectra of the samples in Figure 4.7a are all generally similar, new features are resolved near the first electronic origin (~10240 – 10180 cm^{-1}) upon Gd^{3+} co-doping. These features are precisely the same ones observed in the Yb^{3+}:$CsPbCl_3$ NCs of Figure 4.5 but with different relative intensities, and they are similarly attributable to Yb^{3+} species with different local electrostatic environments beyond the $[YbCl_6]^{3-}$ first coordination sphere. Figure 4.7c plots the 5 K fractional integrated intensities (F_i) of these three peaks against [Yb^{3+}]/([Yb^{3+}] + [Gd^{3+}]) for the samples from Figure 4.7a as well for additional samples from Figure 4.13. Upon introduction of Gd^{3+}, F_A drops rapidly while F_B and F_C increase. These three species also differ in their PL temperature dependence (Figure 4.16). Crucially, co-doping with Gd^{3+} disrupts formation

of proximal $[Yb_{Pb}\text{-}V_{Pb}\text{-}Yb_{Pb}]^0$ pairs, and for the extreme case of 0.9% Yb^{3+}/4.0% Gd^{3+}:$CsPbCl_3$ NCs of Figure 4.7 virtually none of these pairs are expected, replaced instead by $[Yb_{Pb}\text{-}V_{Pb}\text{-}Gd_{Pb}]^0$ pairs (in addition to various partially ($[Yb_{Pb}\text{-}V_{Pb}]^{1-}$) and completely ($[Yb_{Pb}]^{1+}$) dissociated configurations[20]). The increase in peaks *B* and *C* in this sample relative to the 6.6% Yb^{3+}:$CsPbCl_3$ NCs of Figure 4.7 indicates that this PL must be associated with isolated Yb^{3+} ions in some way, rather than with $Yb^{3+}\cdots Yb^{3+}$ pairs. Interestingly, although species *A* dominates the quantum-cutting PL spectrum of Yb^{3+}:$CsPbCl_3$,[18] these results combined with those in Figure 4.6e show that species *B* and *C* can also yield similarly efficient Yb^{3+} PL sensitization. Although the precise microscopic identities of species *A*, *B*, and *C* are unclear, these results thus demonstrate that quantum cutting in Yb^{3+}:$CsPbCl_3$ is tolerant of variations in the microscopic configuration around Yb^{3+} ions. In particular, it is not necessary for participating Yb^{3+} ions to be immediate neighbors to accept energy *via* quantum cutting. This conclusion is consistent with the small binding energy of the shallow-trap state believed to mediate quantum cutting, which endows that state with a relatively large effective radius[20] that allows it to couple with two non-proximal Yb^{3+} ions simultaneously.

4.4 Conclusion

The relationship between Yb^{3+} sensitization and speciation in doped $CsPb(Cl_{1-x}Br_x)_3$ perovskite NCs has been investigated by combining systematic changes in lattice composition with low-temperature high-resolution PL spectroscopy to track the evolution of Yb^{3+} speciation with these changes. Introduction of Br^- changes the local halide coordination around Yb^{3+} ions but is distinctly non-statistical, indicating a thermodynamic preference for retention of Yb-Cl bonds even in the presence of large amounts of lattice Br^-. Addition of Gd^{3+} co-dopants to Yb^{3+}:$CsPbCl_3$ disrupts the formation of proximal $[Yb_{Pb}\text{-}V_{Pb}\text{-}Yb_{Pb}]^0$ pairs and increases the ratio of V_{Pb} to Yb^{3+} ions. Co-doping has little effect on the efficiency of Yb^{3+} sensitization but alters the primary Yb^{3+} speciation, highlighting the tolerance of quantum cutting to variations in the specific identities of participating Yb^{3+} ions, and in particular to the spatial separation between them. These results enhance our fundamental understanding of structure/function relationships in Yb^{3+}:$CsPb(Cl_{1-x}Br_x)_3$ quantum cutters, with ramifications for their optimization and development for future optoelectronic applications.

4.5 Experimental

4.5.1 *Nanocrystal synthesis and anion-exchange reaction*

Materials. Oleylamine (OAm, 70%, Sigma Aldrich), oleic acid (OA, 90%, Sigma Aldrich), 1-octadecene (ODE, 90%, Sigma Aldrich), lead acetate trihydrate ($Pb(OAc)_2 \cdot 3H_2O$, 99.999%, Sigma Aldrich), gadolinium (III) acetate hydrate (99.9%, $Gd(OAc)_3 \cdot xH_2O$, Sigma Aldrich), cesium acetate (CsOAc, 99.9%, Sigma Aldrich), trimethylsilyl chloride (TMS-Cl, 98%, Acros Organics), trimethylsilyl bromide (TMS-Br, 97%, Sigma Aldrich), anhydrous ethanol (EtOH, 200 proof, Decon Laboratories, Inc.), n-hexane (99%, Sigma Aldrich), ethyl acetate (EtOAc, 99%, Sigma Aldrich), and hydrochloric acid (HCl, Macron Fine Chemicals) were used as received unless otherwise noted. As-received ytterbium acetate hydrate ($Yb(OAc)_3 \cdot xH_2O$, 99.9%, Alfa Aesar) was refluxed in glacial acetic acid for 1 hour and stored in a desiccator prior to use.

Nanocrystal synthesis. Doped $CsPbX_3$ (X = Cl, Br) NCs were synthesized as detailed previously.[4] In a typical synthesis, $(Yb(OAc)_3$ (0-12mg), $Gd(OAc)_3$ (0-12mg), $(Pb(OAc)_2 \cdot 3H_2O$ (76 mg), ODE (5.0 mL), OA (1.0 mL), OAm (0.25 mL) and 1M CsOAc in EtOH (0.28 mL) were combined in an oven-dried round bottom flask and degassed on a Schlenk line for 1 hour at 110 °C. The flask was then flushed with N_2 and heated to 240 °C, whereupon a room-temperature TMS-X solution prepared in a nitrogen-filled glovebox (0.2 mL TMS-X and 0.5 mL anhydrous ODE) was injected into the flask. Following the injection, the reaction vessel was immediately cooled using a room-temperature water bath. The reaction vessel with the resulting NC solution was transferred to a nitrogen-filled glovebox, where the solution was centrifuged at 6000 rpm for 10 min. The supernatant was discarded, leaving a white Gd^{3+}-doped, Yb^{3+}-doped, or Gd^{3+}/Yb^{3+}-co-doped $CsPbCl_3$ or yellow Yb^{3+}-doped $CsPbBr_3$ NC pellet. The NC pellet was resuspended in n-hexane and flocculated out of the solution with EtOAc. The suspension then was centrifuged again for 10 min, and the supernatant was discarded. The resulting pellet was resuspended in n-hexane and centrifuged for another 15 min. This solution containing the NCs was stored in anhydrous hexane in a nitrogen glovebox.

Anion exchange using TMS-Br. Yb^{3+}-doped $CsPb(Cl_{1-x}Br_x)_3$ NCs were prepared by anion exchange using Yb^{3+}:$CsPbCl_3$ NCs according to protocols described previously.[5, 22, 23] Briefly, the Yb^{3+}:$CsPbCl_3$ NC solution stored in a nitrogen-filled glovebox was titrated with 1 M TMS-Br until the desired band gap was achieved, as determined by photoluminescence (PL) spectroscopy at

room temperature. The residual TMS-Br and solvent were removed by vacuum evaporation, and the resulting NCs were then resuspended in anhydrous hexane and stored in a nitrogen glovebox.

Anion exchange using OAm-HCl. Yb^{3+}-doped $CsPbCl_3$ NCs were prepared by anion exchange using Yb^{3+}-doped $CsPbBr_3$ NCs according to protocols as detailed previously.[5] In detail, oleylammonium chloride (OAm-HCl) was synthesized by reacting oleylamine with HCl in a 1:1 (v/v) solution of hexane and toluene. Yb^{3+}-doped $CsPbBr_3$ NCs were titrated with the OAm-HCl solution.

4.5.2 *General materials characterization and spectroscopic measurements*

Physical characterization. Elemental composition of NC samples was determined using inductively coupled plasma-atomic emission spectroscopy (ICP-AES, PerkinElmer 8300). The doped NC samples were prepared by digesting NC powders in concentrated nitric acid overnight with ultrasonication. Then, the nitric acid mixture was diluted in ultrapure H_2O. All dopant concentrations in perovskites were determined as the *B*-site cation mole fraction (in %). Transmission electron microscopy (TEM) images were obtained using an FEI TECNAI F20 microscope operating at 200 kV. TEM samples were prepared by dropcasting NCs onto ultrathin carbon-coated copper grids (TED Pella, Inc). Powder x-ray diffraction (XRD) data were collected using a Bruker D8 Discover with a high-efficiency IμS microfocus x-ray source for CuKα radiation (50 kV, 1mA). Samples for XRD measurements were prepared by dropcasting NC suspensions onto silicon substrates.

Spectroscopic measurements. Absorption spectra were collected using an Agilent Cary 5000 spectrometer operating in transmission mode. Samples for PL and time-resolved PL (TRPL) measurements were prepared by dropcasting NCs onto quartz disks and cooling to 5 K in a closed-cycle helium cryostat (Janis, SHI-4H-5). All PL spectra were measured at each temperature using a 375-nm light-emitting diode (LED) for excitation, operating at ~0.6 mW/cm^2 and using a LN_2-cooled silicon charge-coupled device (CCD) camera mounted on a 0.5 m single monochromator. Spectral bandwidths were kept at 0.38 nm (~3.87 cm^{-1}) and 0.03 nm (~0.3 cm^{-1}) for room-temperature and high-resolution PL data, respectively. The samples were excited directly with a 375 nm LED and attenuated with neutral density filters as needed, and the signal was detected using the CCD camera.

4.5.3 *Modeling*

All first-principles calculations were performed with the Vienna Ab-Initio Simulation Package (VASP).[37, 38] Plane-wave, Kohn-Sham density functional theory calculations employed the all-electron projector-augmented wave (PAW) method in the generalized gradient approximation (GGA) with the semilocal PBEsol functional.[39-41] In the pseudopotentials, 9 electrons of Cs ($5s^2$ $5p^6$ $6s^1$), 4 electrons of Pb ($6s^2$ $6p^2$), and 7 electrons of Cl ($3s^2$ $3p^5$) were treated as valence electrons, while 13 *f*-state electrons in the [Xe]$4f^{14}$ $6s^2$ valence configuration of Yb were treated as frozen core states. Blocked Davidson iteration was used to optimize the electronic degrees of freedom. A plane-wave basis cutoff was set to 400 eV, and a Gamma-centered k-point mesh was used for Brillouin zone integration.[42]

A combination of a surrogate energy model based on cluster expansions[43] and Markov chain Monte Carlo (MCMC) were employed to predict the expected Yb_{Pb}-X coordination environment as a function of halide composition. To simplify the combinatorics in generating a dataset for fitting the energy model, we assumed an ideal cubic perovskite structure for enumerating configurations of Cl-Br and Yb_{Pb}-V_{Pb} on their respective sublattices. We assumed, furthermore, that both Yb_{Pb} and V_{Pb} exist in their nominal charge states and constrained our simulation cells to be charge neutral by only allowing for multiples of the fully compensated complex $2Yb_{Pb}+V_{Pb}$, whether dissociated or not. We employed the SHRY software library[44] to enumerate symmetrically distinct Yb_{Pb}-V_{Pb} configurations under this charge-balance constraint. Given the minimum supercell sizes required to fit the longest conformation of these Pb sublattice defect configurations, we subsequently used random uniform enumeration of the Cl-Br site decorations. Initial configurations for subsequent DFT relaxation were generated up to 2x2x3 supercells, and to improve convergence times, lattice constants for a given halide composition were initialized according to Vegard's law.

After obtaining a sufficiently large dataset of DFT calculations, we fit a cluster expansion model to an intrinsic mixing energy, where the absolute DFT energy for a given configuration was refenced to a linear combination of compositional endpoints ($CdPbX_3$, PbX_2, and YbX_3) weighted by the halide fraction and the fractional Pb-sublattice concentrations of Yb_{Pb} and V_{Pb}. To reduce the number of cluster expansion terms and improve convergence of model fitting, we further subtracted a longer-range electrostatic contribution approximated by Ewald summation

(accounting for periodic interactions between Yb_{Pb}^{1+} and V_{Pb}^{2-}) from the total energy. Cluster expansion calculations were facilitated by the ICET software library[45] and model fitting utilized Automatic Relevance Determination (ARD) regression and 10-fold cross validation as implemented in the Scikit-Learn library.[46]

Thermodynamic averages of local Yb_{Pb}-X coordination environments were obtained by sampling equilibrium lattice-site occupancy configurations in the canonical ensemble using Metropolis MCMC. To obtain sufficient statistics, each MCMC simulation for a fixed composition was run for at least 1000 sweeps through the lattice, and finite size effects were mitigated by sampling sufficiently large simulation cells. Statistics we gathered for fixed compositions by doing multi-start runs initialized at room-temperature.

4.6 References

1. Pan, G.; Bai, X.; Yang, D.; Chen, X.; Jing, P.; Qu, S.; Zhang, L.; Zhou, D.; Zhu, J.; Xu, W.; Dong, B.; Song, H. Doping Lanthanide into Perovskite Nanocrystals: Highly Improved and Expanded Optical Properties. *Nano Lett.* **2017,** *17*, 8005-8011.
2. Zhou, D.; Liu, D.; Pan, G.; Chen, X.; Li, D.; Xu, W.; Bai, X.; Song, H. Cerium and Ytterbium Codoped Halide Perovskite Quantum Dots: A Novel and Efficient Downconverter for Improving the Performance of Silicon Solar Cells. *Adv. Mater.* **2017,** *29*, 1704149.
3. Kroupa, D. M.; Roh, J. Y.; Milstein, T. J.; Creutz, S. E.; Gamelin, D. R. Quantum-Cutting Ytterbium-Doped $CsPb(Cl_{1-x}Br_x)_3$ Perovskite Thin Films with Photoluminescence Quantum Yields over 190%. *ACS Energy Lett.* **2018,** *3*, 2390-2395.
4. Milstein, T. J.; Kroupa, D. M.; Gamelin, D. R. Picosecond Quantum Cutting Generates Photoluminescence Quantum Yields Over 100% in Ytterbium-Doped $CsPbCl_3$ Nanocrystals. *Nano Lett.* **2018,** *18*, 3792-3799.
5. Milstein, T. J.; Kluherz, K. T.; Kroupa, D. M.; Erickson, C. S.; De Yoreo, J. J.; Gamelin, D. R. Anion Exchange and the Quantum-Cutting Energy Threshold in Ytterbium-Doped $CsPb(Cl_{1-x}Br_x)_3$ Perovskite Nanocrystals. *Nano Lett.* **2019,** *19*, 1931-1937.
6. Mir, W. J.; Sheikh, T.; Arfin, H.; Xia, Z.; Nag, A. Lanthanide Doping in Metal Halide Perovskite Nanocrystals: Spectral Shifting, Quantum Cutting and Optoelectronic Applications. *NPG Asia Mater.* **2020,** *12*, 9.
7. Dey, A.*, et al.* State of the Art and Prospects for Halide Perovskite Nanocrystals. *ACS Nano* **2021,** *15*, 10775-10981.
8. Roh, J. Y. D.; Milstein, T. J.; Gamelin, D. R. Negative Thermal Quenching in Quantum-Cutting Yb^{3+}-Doped $CsPb(Cl_{1-x}Br_x)_3$ Perovskite Nanocrystals. *Submitted*.
9. Zhou, D.; Sun, R.; Xu, W.; Ding, N.; Li, D.; Chen, X.; Pan, G.; Bai, X.; Song, H. Impact of Host Composition, Codoping, or Tridoping on Quantum-Cutting Emission of Ytterbium in Halide Perovskite Quantum Dots and Solar Cell Applications. *Nano Lett.* **2019,** *19*, 6904-6913.
10. Shockley, W.; Queisser, H. J. Detailed Balance Limit of Efficiency of *p-n* Junction Solar Cells. *J. Appl. Phys.* **1961,** *32*, 510-519.

11. Dexter, D. L. Two Ideas on Energy Transfer Phenomena: Ion-Pair Effects Involving the OH Stretching Mode, and Sensitization of Photovoltaic Cells. *J. Lumin.* **1979,** *18-19*, 779-784.
12. Trupke, T.; Green, M. A.; Würfel, P. Improving Solar Cell Efficiencies by Down-Conversion of High-Energy Photons. *J. Appl. Phys.* **2002,** *92*, 1668-1674.
13. Crane, M. J.; Kroupa, D. M.; Gamelin, D. R. Detailed-Balance Analysis of Yb^{3+}:$CsPb(Cl_{1-x}Br_x)_3$ Quantum-Cutting Layers for High-Efficiency Photovoltaics Under Real-World Conditions. *Energy Environ. Sci.* **2019,** *12*, 2486-2495.
14. Cohen, T. A.; Milstein, T. J.; Kroupa, D. M.; MacKenzie, J. D.; Luscombe, C. K.; Gamelin, D. R. Quantum-Cutting Yb^{3+}-Doped Perovskite Nanocrystals for Monolithic Bilayer Luminescent Solar Concentrators. *J. Mater. Chem. A* **2019,** *7*, 9279-9288.
15. Luo, X.; Ding, T.; Liu, X.; Liu, Y.; Wu, K. Quantum-Cutting Luminescent Solar Concentrators Using Ytterbium-Doped Perovskite Nanocrystals. *Nano Lett.* **2019,** *19*, 338-341.
16. Cai, T.; Wang, J.; Li, W.; Hills-Kimball, K.; Yang, H.; Nagaoka, Y.; Yuan, Y.; Zia, R.; Chen, O. Mn^{2+}/Yb^{3+} Codoped $CsPbCl_3$ Perovskite Nanocrystals with Triple-Wavelength Emission for Luminescent Solar Concentrators. *Adv. Sci.* **2020,** *7*, 2001317.
17. Ding, N.; Xu, W.; Zhou, D.; Ji, Y.; Wang, Y.; Sun, R.; Bai, X.; Zhou, J.; Song, H. Extremely Efficient Quantum-Cutting Cr^{3+}, Ce^{3+}, Yb^{3+} Tridoped Perovskite Quantum Dots for Highly Enhancing the Ultraviolet Response of Silicon Photodetectors with External Quantum Efficiency Exceeding 70%. *Nano Energy* **2020,** *78*, 105278.
18. Roh, J. Y. D.; Smith, M. D.; Crane, M. J.; Biner, D.; Milstein, T. J.; Krämer, K. W.; Gamelin, D. R. Yb^{3+} Speciation and Energy-Transfer Dynamics in Quantum-Cutting Yb^{3+}-Doped $CsPbCl_3$ Perovskite Nanocrystals and Single Crystals. *Phys. Rev. Mater.* **2020,** *4*, 105405.
19. Crane, M. J.; Kroupa, D. M.; Roh, J. Y.; Anderson, R. T.; Smith, M. D.; Gamelin, D. R. Single-Source Vapor Deposition of Quantum-Cutting Yb^{3+}:$CsPb(Cl_{1-x}Br_x)_3$ and Other Complex Metal-Halide Perovskites. *ACS Appl. Energy Mater.* **2019,** *2*, 4560-4565.
20. Sommer, D. E.; Gamelin, D. R.; Dunham, S. T. Defect Formation in Yb-Doped $CsPbCl_3$ from First Principles with Implications for Quantum Cutting. *Phys. Rev. Mater.* **2022,** *6*, 025404.
21. De Siena, M. C.; Sommer, D. E.; Creutz, S. E.; Dunham, S. T.; Gamelin, D. R. Spinodal Decomposition During Anion Exchange in Colloidal Mn^{2+}-Doped $CsPbX_3$ (X = Cl, Br) Perovskite Nanocrystals. *Chem. Mater.* **2019,** *31*, 7711-7722.
22. Creutz, S. E.; Crites, E. N.; De Siena, M. C.; Gamelin, D. R. Anion Exchange in Cesium Lead Halide Perovskite Nanocrystals and Thin Films Using Trimethylsilyl Halide Reagents. *Chem. Mater.* **2018,** *30*, 4887-4891.
23. Creutz, S. E.; Crites, E. N.; De Siena, M. C.; Gamelin, D. R. Colloidal Nanocrystals of Lead-Free Double-Perovskite (Elpasolite) Semiconductors: Synthesis and Anion Exchange To Access New Materials. *Nano Lett.* **2018,** *18*, 1118-1123.
24. Erickson, C. S.; Crane, M. J.; Milstein, T. J.; Gamelin, D. R. Photoluminescence Saturation in Quantum-Cutting Yb^{3+}-Doped $CsPb(Cl_{1-x}Br_x)_3$ Perovskite Nanocrystals: Implications for Solar Downconversion. *J. Phys. Chem. C* **2019,** *123*, 12474-12484.
25. Linaburg, M. R.; McClure, E. T.; Majher, J. D.; Woodward, P. M. $Cs_{1-x}Rb_xPbCl_3$ and $Cs_{1-x}Rb_xPbBr_3$ Solid Solutions: Understanding Octahedral Tilting in Lead Halide Perovskites. *Chem. Mater.* **2017,** *29*, 3507-3514.
26. Tanner, P. A. Electronic Spectra of Yb^{3+} in Elpasolite Lattices. *Molec. Phys.* **1986,** *58*, 317-328.

27. Han, Q.; Wu, W.; Liu, W.; Yang, Q.; Yang, Y. Temperature-Dependent Photoluminescence of $CsPbX_3$ Nanocrystal Films. *J. Lumin.* **2018,** *198*, 350-356.
28. Milstein, T. J.; Roh, J. Y. D.; Jacoby, L. M.; Crane, M. J.; Sommer, D. E.; Dunham, S. T.; Gamelin, D. R. Ubiquitous Near-Band-Edge Defect State in Rare-Earth-Doped Lead-Halide Perovskites. *Chem. Mater.* **2022,** *34*, 3759-3769.
29. Mir, W. J.; Mahor, Y.; Lohar, A.; Jagadeeswararao, M.; Das, S.; Mahamuni, S.; Nag, A. Postsynthesis Doping of Mn and Yb into $CsPbX_3$ (X = Cl, Br, or I) Perovskite Nanocrystals for Downconversion Emission. *Chem. Mater.* **2018,** *30*, 8170-8178.
30. Li, M.; Zhang, X.; Matras-Postolek, K.; Chen, H.-S.; Yang, P. An Anion-Driven Sn^{2+} Exchange Reaction in $CsPbBr_3$ Nanocrystals Towards Tunable and High Photoluminescence. *J. Mater. Chem. C* **2018,** *6*, 5506-5513.
31. Van der Stam, W.; Geuchies, J. J.; Altantzis, T.; van den Bos, K. H. W.; Meeldijk, J. D.; Van Aert, S.; Bals, S.; Vanmaekelbergh, D.; de Mello Donega, C. Highly Emissive Divalent-Ion-Doped Colloidal $CsPb_{1-x}M_xBr_3$ Perovskite Nanocrystals through Cation Exchange. *J. Am. Chem. Soc.* **2017,** *139*, 4087-4097.
32. Xu, K.; Lin, C. C.; Xie, X.; Meijerink, A. Efficient and Stable Luminescence from Mn^{2+} in Core and Core–Isocrystalline Shell $CsPbCl_3$ Perovskite Nanocrystals. *Chem. Mater.* **2017,** *29*, 4265-4272.
33. Bond Energies. In *Encyclopedia of Inorganic Chemistry*, King, R. B.; Crabtree, R. H.; Lukehart, C. M.; Atwood, D. A.; Scott, R. A., Eds. Wiley: 2006.
34. Yang, G.; Zheng, C.; Zhu, Y.; Li, X.; Huang, J.; Xu, X.; Liu, W.; Cui, S.; Pan, G. Efficient Quantum Cutting of Lanthanum and Ytterbium Ions Co-Doped Perovskite Quantum Dots Towards Improving the Ultraviolet Response of Silicon-Based Photodetectors. *J. Alloys Compd.* **2022,** *921*, 166097.
35. Li, D.; Chen, G. Near-Infrared Photoluminescence from Ytterbium- and Erbium-Codoped $CsPbCl_3$ Perovskite Quantum Dots with Negative Thermal Quenching. *J. Phys. Chem. Lett.* **2023,** *14*, 2837-2844.
36. Zeng, M.; Artizzu, F.; Liu, J.; Singh, S.; Locardi, F.; Mara, D.; Hens, Z.; Van Deun, R. Boosting the Er^{3+} 1.5 μm Luminescence in $CsPbCl_3$ Perovskite Nanocrystals for Photonic Devices Operating at Telecommunication Wavelengths. *ACS Appl. Nano Mater.* **2020,** *3*, 4699-4707.
37. Kresse, G.; Furthmüller, J. Efficient Iterative Schemes for Ab Initio Total-Energy Calculations Using a Plane-Wave Basis Set. *Phys. Rev. B* **1996,** *54*, 11169-11186.
38. Kresse, G.; Furthmüller, J. Efficiency of Ab-Initio Total Energy Calculations for Metals and Semiconductors Using a Plane-Wave Basis Set. *Comput. Mater. Sci.* **1996,** *6*, 15-50.
39. Blöchl, P. E. Projector Augmented-Wave Method. *Phys. Rev. B* **1994,** *50*, 17953-17979.
40. Kohn, W.; Sham, L. J. Self-Consistent Equations Including Exchange and Correlation Effects. *Phys. Rev.* **1965,** *140*, A1133-A1138.
41. Perdew, J. P.; Ruzsinszky, A.; Csonka, G. I.; Vydrov, O. A.; Scuseria, G. E.; Constantin, L. A.; Zhou, X.; Burke, K. Restoring the Density-Gradient Expansion for Exchange in Solids and Surfaces. *Phys. Rev. Lett.* **2008,** *100*, 136406.
42. Monkhorst, H. J.; Pack, J. D. Special Points for Brillouin-Zone Integrations. *Phys. Rev. B* **1976,** *13*, 5188-5192.
43. Sanchez, J. M.; Ducastelle, F.; Gratias, D. Generalized Cluster Description of Multicomponent Systems. *Physica A: Statistical Mechanics and its Applications* **1984,** *128*, 334-350.

44. Prayogo, G. I.; Tirelli, A.; Utimula, K.; Hongo, K.; Maezono, R.; Nakano, K. Shry: Application of Canonical Augmentation to the Atomic Substitution Problem. *J. Chem. Inf. Model.* **2022,** *62*, 2909-2915.
45. Ångqvist, M.; Muñoz, W. A.; Rahm, J. M.; Fransson, E.; Durniak, C.; Rozyczko, P.; Rod, T. H.; Erhart, P. ICET – A Python Library for Constructing and Sampling Alloy Cluster Expansions. *Adv. Theory and Simul.* **2019,** *2*, 1900015.
46. Pedregosa, F.; Varoquaux, G.; Gramfort, A.; Michel, V.; Thirion, B.; Grisel, O.; Blondel, M.; Prettenhofer, P.; Weiss, R.; Dubourg, V.; Vanderplas, J.; Passos, A.; Cournapeau, D.; Brucher, M.; Perrot, M.; Duchesnay, É. Scikit-learn: Machine Learning in Python. *J. Mach. Learn. Res.* **2011,** *12*, 2825-2830.

4.7 Appendix

4.7.1 *Additional structural characterization data*

Additional TEM images for Yb^{3+}:$CsPbX_3$ nanocrystals

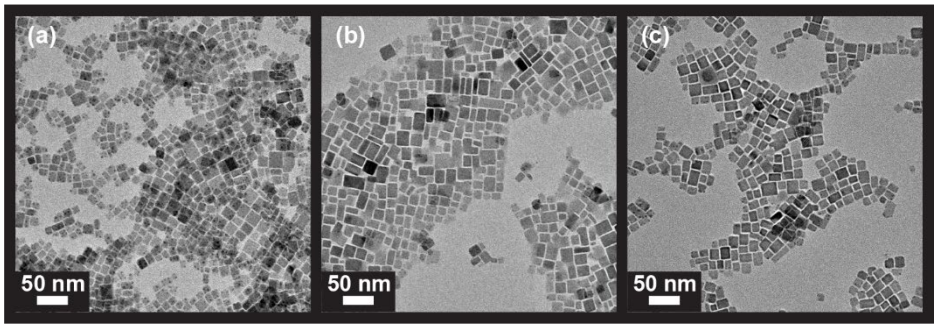

Figure 4.8. Transmission electron microscopy (TEM) images of **(a)** Yb^{3+}:$CsPb(Cl_{0.63}Br_{0.37})_3$ NCs (l = 14.4 ± 2.0 nm), **(b)** Yb^{3+}:$CsPb(Cl_{0.35}Br_{0.65})_3$ NCs (l = 14.9 ± 2.7 nm), and **(c)** Yb^{3+}:$CsPb(Cl_{0.00}Br_{1.00})_3$ NCs (l = 15.4 ± 2.0 nm), all obtained *via* anion exchange from the 7.8% Yb^{3+}:$CsPbCl_3$ NCs of Figure 4.1a.

Additional XRD data for Yb^{3+}:$CsPb(Cl_{1-x}Br_x)_3$ nanocrystals

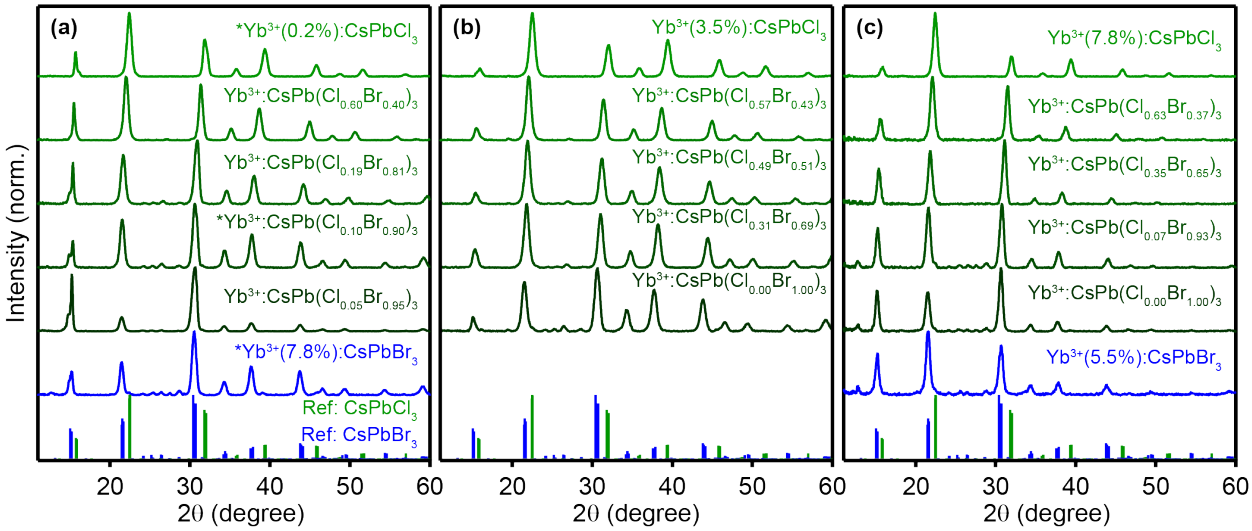

Figure 4.9. Powder X-ray diffraction (pXRD) data collected for (light green) 0.2% Yb^{3+}:$CsPbCl_3$ NCs, (dark green) Yb^{3+}:$CsPb(Cl_{1-x}Br_x)_3$ NCs obtained *via* anion exchange from the 0.2% Yb^{3+}:$CsPbCl_3$ NCs at the top of the panel, and (blue) 7.8% Yb^{3+}:$CsPbBr_3$ NCs prepared by direct synthesis. * denotes the same pXRD patterns as shown in Figure 4.1d. **(b)** pXRD data collected for (light green) 3.5% Yb^{3+}:$CsPbCl_3$ NCs and (dark green) Yb^{3+}:$CsPb(Cl_{1-x}Br_x)_3$ NCs obtained *via* anion exchange. **(c)** pXRD data collected for (light green) 7.8% Yb^{3+}:$CsPbCl_3$ NCs and (dark green) Yb^{3+}:$CsPb(Cl_{1-x}Br_x)_3$ NCs (dark green)

obtained *via* anion exchange, and (blue) 5.5% Yb^{3+}:$CsPbBr_3$ NCs. Reference: $CsPbCl_3$ (red) and $CsPbBr_3$ (blue).[1]

4.7.2 *Additional optical characterization data*

Room-temperature optical characterization for Yb^{3+}:$CsPb(Cl_{1-x}Br_x)_3$ NCs

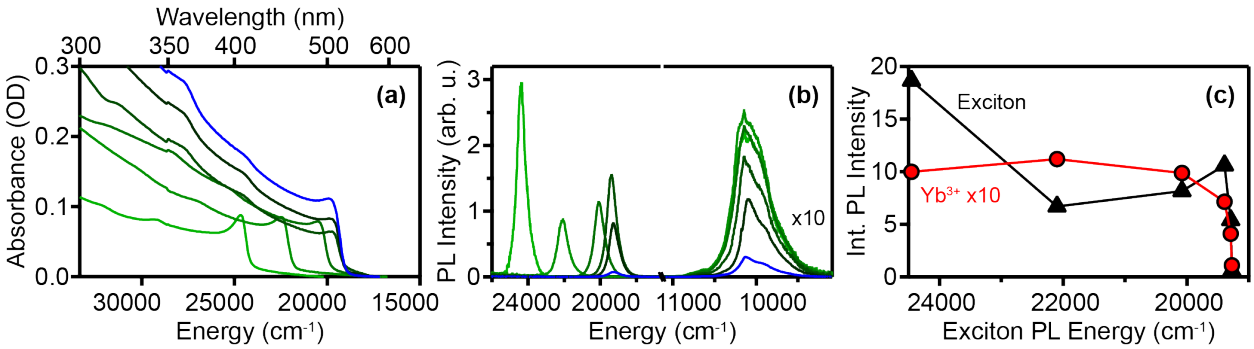

Figure 4.10. (a) Room-temperature absorption spectra of (light green) 0.2% Yb^{3+}:$CsPbCl_3$ NCs and (dark green) 0.2% Yb^{3+}:$CsPb(Cl_{1-x}Br_x)_3$ NCs obtained *via* anion exchange, and of (blue) 5.5% Yb^{3+}:$CsPbBr_3$ NCs. **(b)** Photoluminescence (PL) spectra of the same Yb^{3+}:$CsPb(Cl_{1-x}Br_x)_3$ NCs from panel (a). **(c)** Total integrated excitonic (black) and Yb^{3+} $^2F_{5/2} \rightarrow {}^2F_{7/2}$ (red) PL intensities from the data in panel (b).

Additional 5-K photoluminescence data for Yb^{3+}:$CsPb(Cl_{1-x}Br_x)_3$ nanocrystals

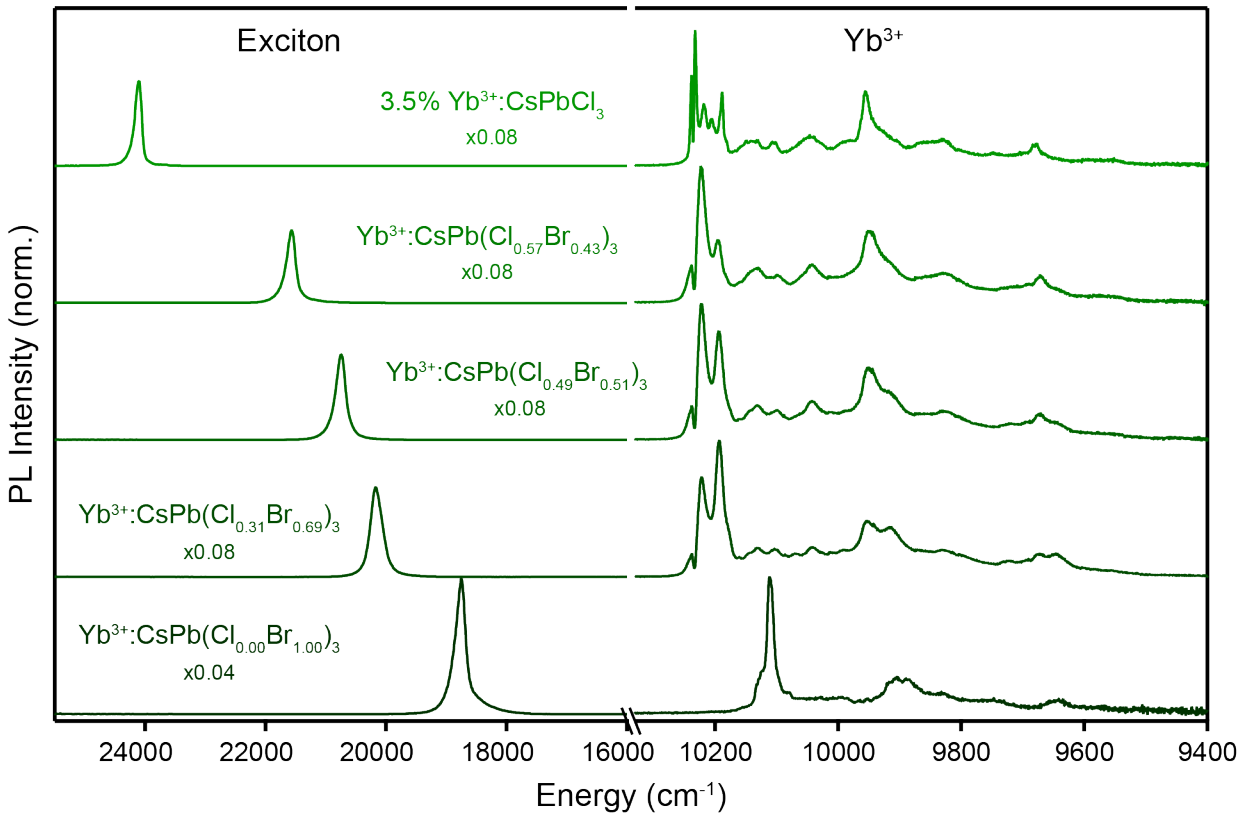

Figure 4.11. 5 K PL spectra of a series of 3.5% Yb^{3+}:$CsPb(Cl_{1-x}Br_x)_3$ NCs with increasing Br^- molar fractions (top to bottom). From top to bottom, the exciton region has been multiplied by 0.08, 0.08, 0.08, 0.08, and 0.04 to display it on the same scale as the Yb^{3+} PL. All measurements used continuous-wave (CW) excitation at λ_{ex} = 375 nm (26700 cm^{-1}).

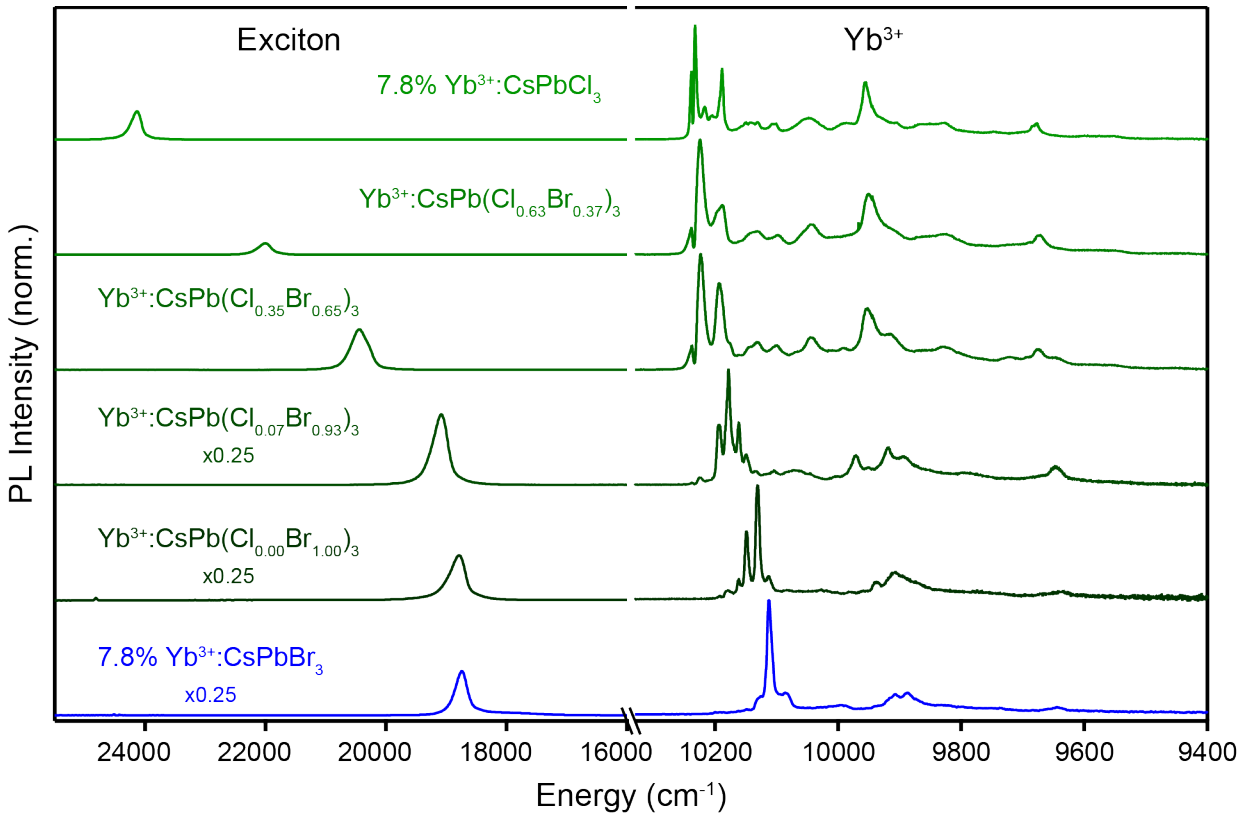

Figure 4.12. 5 K PL spectra of a series of 7.8% Yb^{3+}:$CsPb(Cl_{1-x}Br_x)_3$ NCs prepared by anion exchange (dark green), and of 7.8% Yb^{3+}:$CsPbBr_3$ NCs (blue) independently synthesized by hot-injection. From top to bottom, the exciton region has been multiplied by 1.00, 1.00, 1.00, 0.25, 0.25, and 0.25 to display it on the same scale as the Yb^{3+} PL. All measurements used CW excitation at λ_{ex} = 375 nm (26700 cm^{-1}).

Additional 5 K photoluminescence data for Yb^{3+}, Gd^{3+}:$CsPbCl_3$ nanocrystals

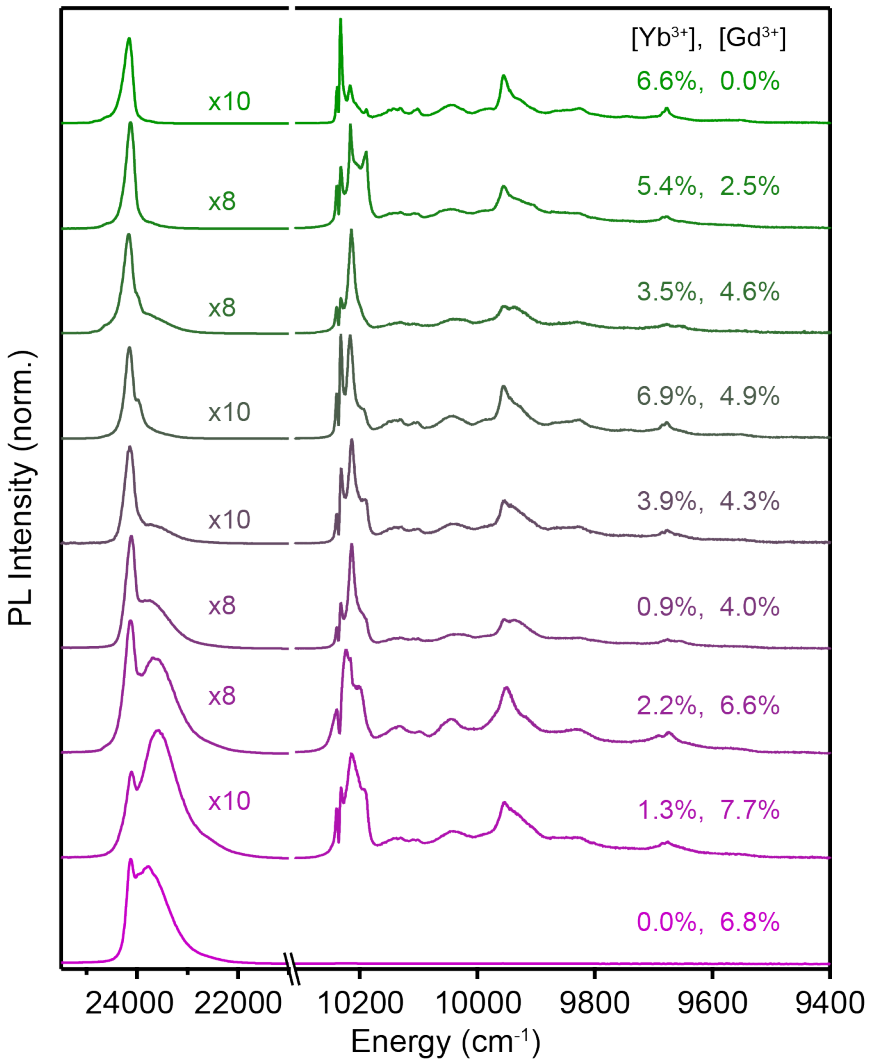

Figure 4.13. 5 K PL spectra of the 6.6% Yb^{3+}:$CsPbCl_3$ (top, green), Yb^{3+}, Gd^{3+}:$CsPbCl_3$ (middle, green-purple) at various dopant concentrations, and 6.8% Gd^{3+}:$CsPbCl_3$ (magenta) NCs. λ_{ex} = 375 nm (26700 cm^{-1}). From top to bottom, the exciton region has been multiplied to place it on the same scale as the Yb^{3+} PL.

Variable-temperature photoluminescence data for Yb^{3+}/Gd^{3+}:$CsPbCl_3$ nanocrystals

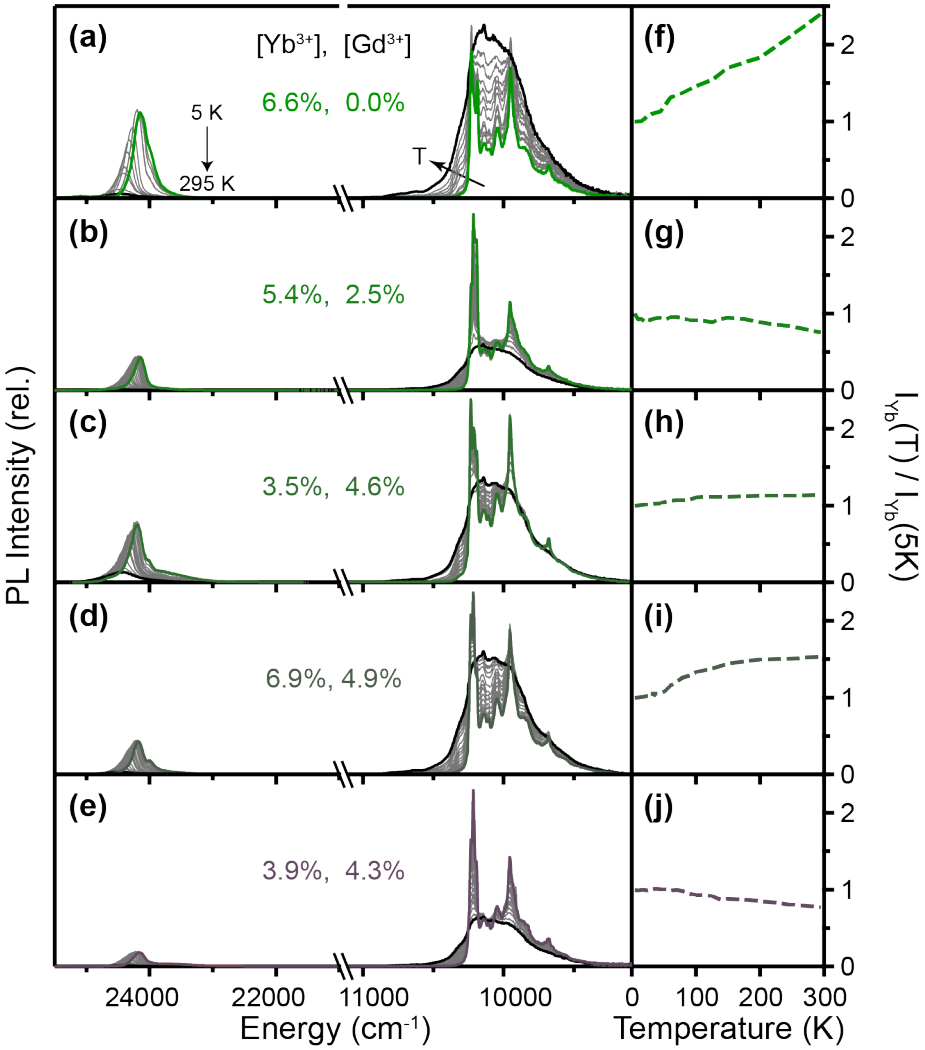

Figure 4.14. Variable-temperature PL (VTPL) spectra of **(a)** 6.6% Yb^{3+}:$CsPbCl_3$ and **(b-e)** a series of Yb^{3+}/Gd^{3+}:$CsPbCl_3$ NCs from 5 (colored) to 295 K. **(f-j)** Integrated Yb^{3+} PL intensity at each temperature relative to the intensity at 5 K ($I_{Yb}(T)/I_{Yb}(5K)$), plotted as a function of temperature for each sample from (a-e). All measurements used continuous-wave (CW) excitation at λ_{ex} = 375 nm (26700 cm^{-1}).

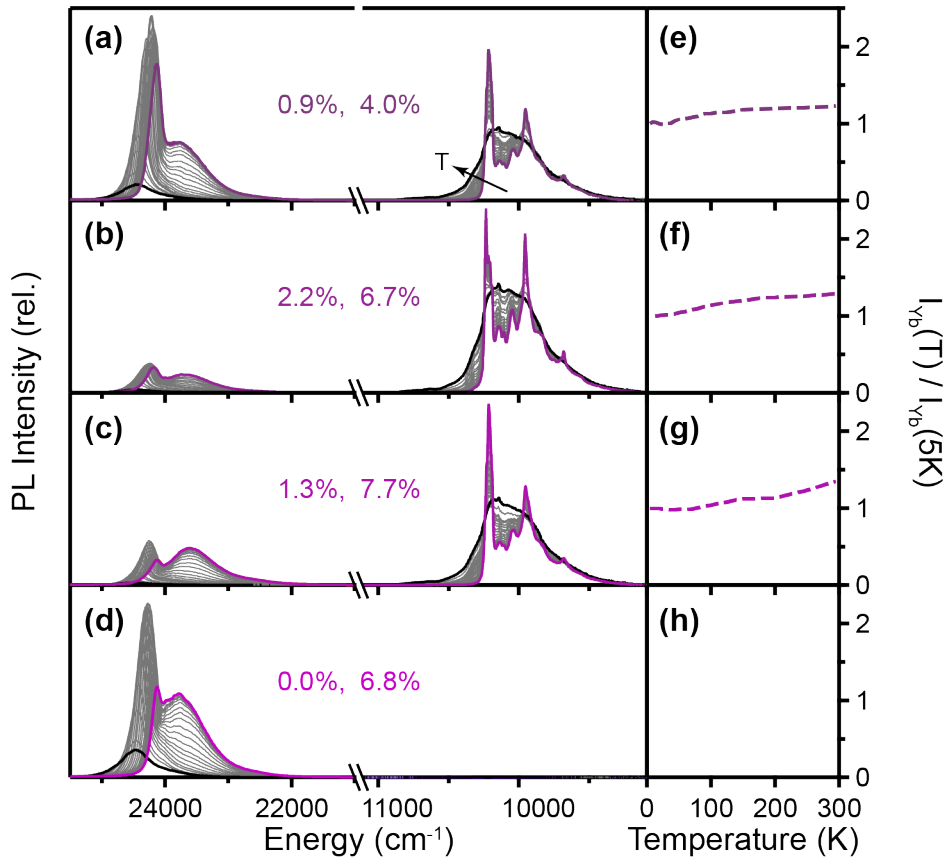

Figure 4.15. VTPL spectra of **(a-c)** series of Yb^{3+}/Gd^{3+}:$CsPbCl_3$ and **(d)** 6.8% Gd^{3+}:$CsPbCl_3$ NCs measured from 5 (colored) to 295 K. **(e-h)** Integrated Yb^{3+} PL intensity at each temperature relative to the intensity at 5 K ($I_{Yb}(T)/I_{Yb}(5K)$), plotted as a function of temperature for each sample from (a-e). All measurements used CW excitation at λ_{ex} = 375 nm (26700 cm^{-1}).

Additional analysis of Yb^{3+} speciation and variable-temperature photoluminescence data for Yb^{3+}/ Gd^{3+}:$CsPb(Cl_{1-x}Br_x)_3$ nanocrystals

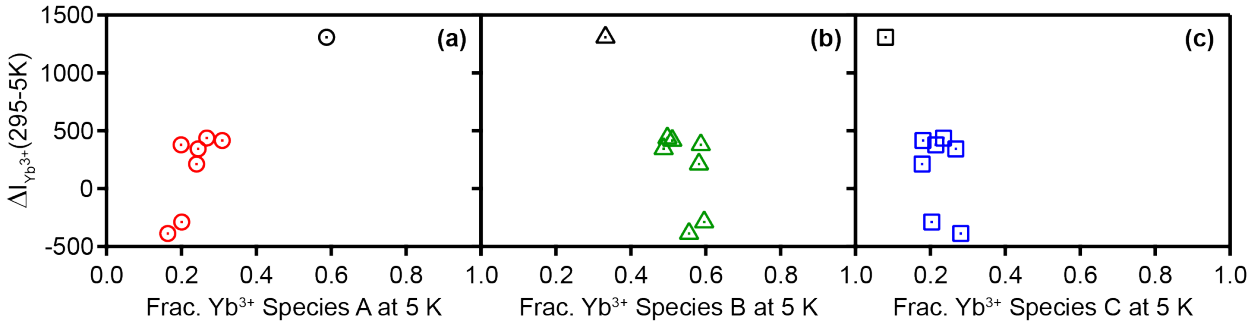

Figure 4.16. (a, b, c) The change in integrated Yb^{3+} PL intensity upon warming from 5 to 295 K (ΔI_{Yb}(295-5K)) plotted against the fractional intensities of Yb^{3+} PL peaks associated with species *A* (circles), *B* (triangles), and *C* (squares) measured at 5 K for 6.6% Yb^{3+}:$CsPbCl_3$ (black) and the entire series of Yb^{3+}/Gd^{3+}:$CsPbCl_3$ (colored) NCs taken from Figures 4.14 and 4.15.

4.7.3 *Additional modeling data*

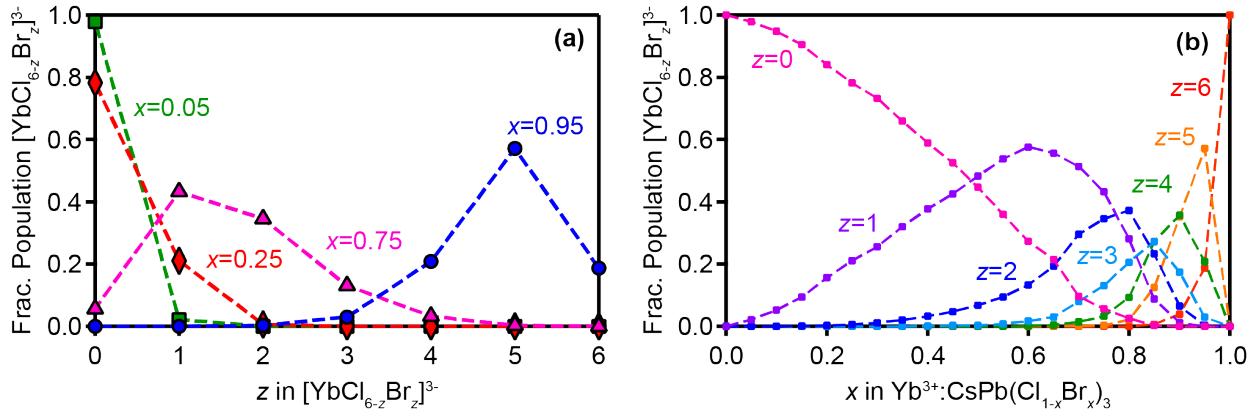

Figure 4.17. (a) Room-temperature Monte Carlo simulation of the fractional population of $[YbCl_{6-z}Br_z]^{3-}$ ($0 \leq z \leq 6$) species in 5.0% Yb^{3+}:$CsPb(Cl_{1-x}Br_x)_3$ at x = 0.05 (green), 0.25 (red), 0.75 (pink), and 0.95 (blue), plotted as a function of z. **(b)** The fractional populations of $[YbCl_{6-z}Br_z]^{3-}$ species with $0 \leq z \leq 6$ plotted as a function of x in Yb^{3+}:$CsPb(Cl_{1-x}Br_x)_3$.

4.7.4 *References*

1. Linaburg, M. R.; McClure, E. T.; Majher, J. D.; Woodward, P. M. $Cs_{1-x}Rb_xPbCl_3$ and $Cs_{1-x}Rb_xPbBr_3$ Solid Solutions: Understanding Octahedral Tilting in Lead Halide Perovskites. *Chem. Mater.* **2017,** *29*, 3507-3514.